# MODELLING THE FLUID-STRUCTURE INTERACTION IN FLOW SENSING AND CELL ADHESION

**CUI JINGYU**

**PhD**

**The Hong Kong Polytechnic University**

**2021**

The Hong Kong Polytechnic University

Department of Mechanical Engineering

# Modelling the Fluid-Structure Interaction in Flow Sensing and Cell Adhesion

**Cui Jingyu**

A thesis submitted in partial fulfilment of the requirements for the degree of Doctor of Philosophy

April 2021

# CERTIFICATE OF ORIGINALITY

I hereby declare that this thesis is my own work and that, to the best of my knowledge and belief, it reproduces no material previously published or written, nor material that has been accepted for the award of any other degree or diploma, except where due acknowledgement has been made in the text.

__________________(Signed)

CUI Jingyu (Name of student)

# Abstract

The first part of this study concerns the modelling of the flow sensing of primary cilia via their passive deflection in an oscillating viscous flow. A two-way fluid-cilia interaction is considered in the modelling using an immersed boundary-lattice Boltzmann method (IB-LBM). Typically, the primary cilium is modelled as a slender filament with its basal end connecting to a nonlinear rotational spring to reproduce the experimentally observed basal rotation.

The developed algorithm and code are first validated against some benchmark problems, and then applied to study the dynamics of a three-dimensional cilia array in an oscillating Newtonian flow. The simulation result indicates that the primary cilia do an in-plane flapping motion which is symmetrical in term of the cilium profiles. During the deflection, the flow-induced curvature at the lower part of the primary cilium synchronizes well with the applied pressure gradient signal, while an obvious phase lag in the curvature can be found for the rest parts of the cilium. Therefore, the lower part of primary cilia may be most responsible for detecting the variations of the flow information as it can provide real-time response. The simulation result also suggests that the location of the maximal tensile stress (MTS) may not always stay at the cilium's base region, instead is able to propagate from the cilium's base point to its tip for a certain distance. The presence of primary cilia is found to reduce the average wall shear stress (WSS) level and affect the oscillation characteristic of the WSS field by making the WSS in some regions less oscillatory.

A follow-up parametric study which covers the peak Reynolds number ($Re_{peak}$), the Womersley number ($Wo$), the cilium length, and the spacing interval, is also performed to investigate how these parameters affect the flow-cilia interaction. By examining the variations of curvature direction in the cilium profile, our simulations capture three typical stretch states. For primary cilia with short and medium length, an increase in the maximal tip deflection is accompanied with a greater propagation distance of the MTS location. While this may not be true for long primary cilia that extend into 1/3 of the lumen, as the possible emergence of the third stretch state could greatly suppress such propagation. Under the same flow condition, the decrease in the average WSS is found to be more significant when a cilium undergoes a larger span of deflection and/or when the spacing interval is reduced. Compared with the spacing interval, the span of deflection plays a marginal role in decreasing WSS. For the parameter ranges considered, an increase in the $Re_{peak}$ or cilium length is found to bring a larger cilium deflection and maximal curvature. An increase in the $Wo$, however, is found to decrease these two quantities. For a constant spacing interval, a larger span of deflection is found to correspond to a more uneven OSI distribution. The interacting between neighboring cilia becomes weaker as the spacing interval increases. A sparser cilia array therefore tends to have a larger deflection, maximal curvature, and propagation distance of the MTS location. For a medium $Re_{peak}$ and $Wo$, a spacing interval greater than twice the cilium length is found to effectively reduce the interference from the neighboring cilia thus improves the cilium's sensing accuracy. This could be the reason why there is only one primary cilium at most for each endothelial or epithelial cell whose diameter happens to be about 2-3 times the length of primary cilium.

The power-law model is also integrated into our IB-LBM framework to study cilium dynamics in oscillating no-Newtonian fluids. The simulation result suggests that a sensory failure may occur when $n$=1.5, as the primary cilia could no longer capture the symmetry of the input pressure signal via their passive deflection. No significant difference in the flow structure is observable for different $n$ values. However, as $n$ increases, a larger affected area with smaller OSI value can be observed in the OSI distribution. Compared with the Newtonian fluid case, the decrease in the average WSS is more dramatic for a shear-thinning fluid while less obvious for shear-thickening fluid. Therefore, modelling a shear-thinning fluid as Newtonian underestimates the cilium's impact on the WSS while modelling a shear-thickening fluid as Newtonian tends to overestimate such impact.

The second part of the thesis focus on the simulation of circulating tumor cell (CTC) adhesion in a three-dimensional curved microvessel. A comparative study is first performed to characterize the differences between the adhesion of CTC in straight and curved vessels. After that, a parametric study is performed to investigate the effect of the flow driven force density $f$ (or $Re$) and membrane bending modulus $K_b$ on CTC adhesion. Our simulation results suggest that the CTC is more likely to adhere to the curved vessel as more bonds will form around the curvature transition regions due to centrifugal effect which increases cell-wall contact. The parametric study indicates that an increase in the $f$ or a decrease in the $K_b$ (e.g., the cell becomes softer), increases the bond formation probability and cell-wall contact sites in the curved vessel. Increasing

the $f$ brings a larger centrifugal force while decreasing the $K_b$ enables a more complete cell-wall contact by increasing the contact area, both of which promotes bond formation. In the curved-vessel case, the site where bonds are formed the most (hotspot) is found to vary with the applied $f$ and the $K_b$. For the vessel geometry considered, the hotspot tends to be within the first bend of the vessel when the applied $f$ is relatively low; however, the hotspot is found to shift to the second bend of the vessel as $f$ increases or $K_b$ decreases.

**Keywords:** cilium dynamics, cell adhesion, IB-LBM, DPD, oscillating flow, curved vessel

# Publications arising from the thesis

Journal paper:

1. **Jingyu Cui**, Yang Liu*, and Bingmei Fu, "A three-dimensional simulation of the dynamics of primary cilia in an oscillating flow". (in preparation)
2. **Jingyu Cui**, Yang Liu*, Yuzhen Jin, "Impact of initial fiber states on different fiber dynamic patterns in the laminar channel flow", *International Journal of Mechanical Science,* 2021.198: 106359.
3. **Jingyu Cui**, Yang Liu*, Lanlan Xiao, Shuo Chen, and Bingmei M. Fu, Numerical study on the adhesion of a circulating tumor cell in a curved microvessel. *Biomechanics and Modeling in Mechanobiology*, 2021. 20:243–254.
4. **Jingyu Cui**, Yang Liu*, and Bingmei M. Fu, Numerical study on the dynamics of primary cilium in pulsatile flows by the immersed boundary-lattice Boltzmann method. *Biomechanics and Modeling in Mechanobiology*, 2020. 19(1): 21-35.

Conference paper:

1. **Jingyu Cui**, Yang Liu, Lanlan Xiao, and Shuo Chen, Simulating the dynamics of primary cilium in pulsatile flow by the immersed boundary-lattice Boltzmann method, *5th Symposium on Fluid-Structure-Sound Interactions and Control*, August 2019, Greece.

# Acknowledgements

First of all, I would like to thank my supervisor, Dr. Yang Liu, for his guidance and support during my PhD studies at the Hong Kong Polytechnic University. His mentoring in research, his patience and motivation helped me a lot during all my research projects and in writing this thesis. He held me to a high standard while allowed for lots of freedom on the project selection to capitalize on my strength. Without his guidance and support, this thesis would have not been possible, or at least not to this extent.

I would like to thank my Co-supervisors, professor Shuo Chen and Dr. Lanlan Xiao for their advices and help on this project. In particular, I would like to thank professor Bingmei M. Fu for reviewing and giving suggestions on my thesis as well as the arising articles.

I would like to express my gratitude to all faculty members for their scientific advice and the wonderful courses provided in the Mechanical Engineering department. I am also grateful to Tianxi Chi, Shuhong Liu, Mingran Liu and Liangjing Zhao for a friendly and collaborative environment in the group. My gratitude is extended to my officemates including but not limited to Zhaokun Wang, Feng Ren, Weiping Yang, and Tong Zhou for numerous interesting discussions on scientific matters. It is my pleasure to work and study with you all.

I would also like to express my deepest gratitude to my fiancée Yuqian Zhang for her love, sacrifice and tremendous encouragement and support during my PhD study.

Last but certainly not least, I would like to thank my families, especially my dear father, for their unconditional support, encouragement, and love throughout all these years.

# Table of contents

# List of figures

# List of tables

# Chapter 1 Introduction

## 1.1 Primary cilia as a flow sensor

### 1.1.1 Background and significance

Primary cilia are filament-like, immotile organelles solitarily protruding into extracellular space from the apical surface of nearly every mammalian cell [1, 2]. Though primary cilia were originally discovered over a century ago, their exact functions remain incompletely understood. Indeed, they were once believed to be vestigial organelles [3]. However, in the past few decades, increasing studies have revealed the primary cilium to be a multifunctional antenna, sensing both mechanical (e.g., fluid drag, pressure, vibration) and chemical (e.g., light, odor) changes in the extracellular environment [4].

The primary cilia have an anatomical structure similar to that of the motile cilia but in a relatively simper manner. They both have a membrane enclosed axoneme, which contains nine circumferentially arranged doublet microtubules. However, unlike the motile cilia, the primary cilia do not have any central pairs at their axonemes, thus have a 9+0 microtubule doublet structure (see Fig. 1.1). The primary cilia also lack some other axonemal components that are found in motile cilia, including radial spokes, dynein arms and nexin links. Consequently, the primary cilia are less stiff and unable to spontaneously generate internal forces like motile cilia [5].

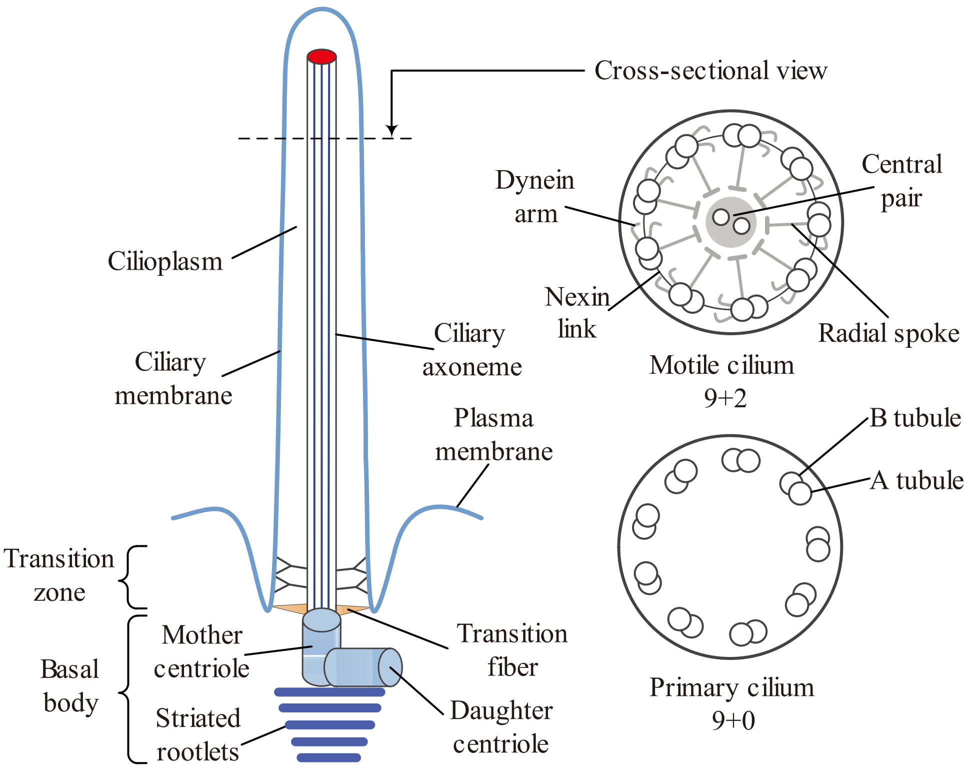

Fig. 1.1 Sketch of structures of primary cilium and motile cilium

Proper function and homeostasis of a wide range of cells and tissues require mechanical stimuli from extracellular environment. Variation of these stimuli, such as the oscillation of the blood flow and changes of osmolality and hydrostatic pressure in renal tubule flow, needs to be sensed and transduced among different cell components. Recent studies have revealed that the primary cilium, an immotile extension from cell surface, acts as a sensor for the perceiving and mechanotransduction of these mechanical stimuli, as it has been experimentally demonstrated that the passive bending of the primary cilium is correlated with initiation of a variety of signaling cascades [6-9]. For example, in ciliated kidney cells, the passive deflection of epithelium primary cilia induced by the flow drag or directly via a micropipette (mechanical load), could lead to an increased intracellular calcium level, an important second messenger communicating the extracellular activities with the cell nucleus. In contrast to the ciliated cells, kidney cells without a cilium are unable to translate such mechanical stimulation into the cell nucleus by increasing intracellular calcium levels. This deflection-triggered calcium increase, is reported to rely on the opening of PC2 cation channel which localizes to the membrane of primary cilia and more importantly, these channels are believed to be stretch-activated [8, 9]. The resulting change in intracellular calcium concentration then helps to regulate numerous molecular activities inside the cell that contributes to tissue and organ development [6]. Similar mechanism has also been found in the blood-pressure maintenance mechanism in vasculatures, where endothelial primary cilia sense the flow information and regulate the vessel diameter via adjusting nitric oxide production [10].

These observations and measurements indicate that the primary cilia sense flow information via their passive deflection which contributes to the activation of various signaling pathways. But how do primary cilia encode/response to the spatial and temporal patterns of natural stimuli? and what is the relationship between the activation of signaling pathways and the cilium deflection? These are still open questions. This study aims to address the first question and explore how the fluid-cilium interaction affects cilium deflection and the near-wall flow pattern. The deflection of primary cilium not only results in the change of force and stress distributions in the cilium membrane but could also alter the regime of the near-wall flow. Understanding this fluid-cilia/cilium interaction will greatly help to interpret the role of primary cilium as a flow sensor and may have rich practical implications. For instance, it may shed light on the design of artificial flow sensors, especially for biological applications that usually involve low-Reynolds-number and pulsatile flow conditions.

On the other hand, defects of primary cilium in ciliary protein or its physical structure are linked with numerous diseases which known as ciliopathies, for instance, polycystic kidney disease [11, 12], cystic and fibrotic liver disease [13], osteoarthritis [14], obesity [15] and even cancer [16, 17]. So, one tentative idea for treating those ciliopathies is by rescuing or regulating corresponding cilium form and its mechanosensing function. It has already been suggested that through adjusting the parameters of primary cilium, for instance, its length and bending module, one can alter the deflection response of cilium to mechanical stimuli, and further manage to manipulate the mechanosensitivity of primary cilium [18]. Recently, an experiment aimed to alter the bending modulus of primary cilia via pharmacological treatment was successfully performed [19], adding credit to the idea of treating ciliopathies through cilium manipulation. Other ideas such as using magnetic force to manipulate the dynamics of artificial cilia to generate a directional local flow were also reported [20]. Successful treatment of ciliopathies through cilium manipulation depends on the understanding of cilium deflection. Performing numerical studies on the fluid-cilium interaction system will contribute to the development of possible therapeutic treatment of ciliopathies in the long run.

### 1.1.2 Models for studying cilium deflection

The length of endothelial primary cilia usually ranges from 1.8 to11.1μm, while the diameter is about 0.2μm [21]. At such scale, experimental measurements of the force and stress that involved during the deflection process are still highly challenging to obtain at present. Simulations can complement experiments by providing information that is not easily obtained through direct measurement, thus could be helpful in elucidating and quantifying this process and mechanism. In fact, primary cilium, as a kind of filiform hair structure, has already been numerically studied with various mathematical models in the past few decades. In this section, we will give a brief review on the previous models for such structures.

#### 1.1.2.1 Inverted pendulum model

The first mathematical model developed for modelling the deflection of a filiform hair structure may be the inverted pendulum model proposed by Shimozawa and Kanou [22, 23]. In this model, the filiform hair is approximated as an inverted, rigid pendulum with its basal end connecting to a spring and a damper (viscous resistance) to resist angular displacement as shown in Fig. 1.2. The fluid drag in this model is approximated using Stokes's solution.

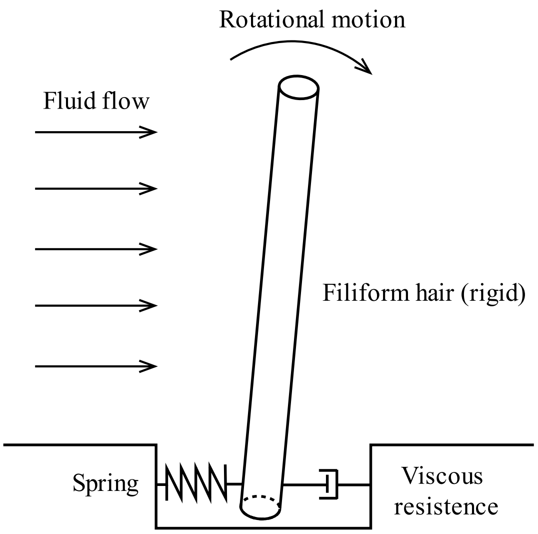

Fig. 1.2 A schematics of the inverted pendulum model

Humphrey et al. [24, 25] improved the original inverted pendulum model by adding a virtual mass forces into the hair angular momentum equation to account for the effect of fluid inertia on the hair motion. However, their model does not consider the impact of hair on the flow field thus does not involves any interactions between the hairs. To make the flow feels the existence of the hairs, Cummins et al.[26] modified the velocity by adding a perturbation velocity caused by the presence of hairs. The perturbation velocity is calculated based on the steady Stokes flow approximated. They applied this model to study the fluid-mediated interaction between multiple hairs.

The inverted pendulum model is simple and naturally accounts for the basal rotations of the hair. However, it assumes that the hair is rigid thus is likely to have a low prediction accuracy for those complaint filiform hair structures (e.g., the primary cilium).

### 1.1.2.2 Cantilevered Euler-Bernoulli beam model

The cantilevered Euler-Bernoulli beam model may be the simplest model for studying the deflection of an elastic primary cilium. In this model, the primary cilium is considered as a one-dimensional (i.e., represented by its the neutral line) homogeneous slender cantilevered beam whose bending behavior is governed by a Euler-Bernoulli beam formulation. For the equilibrium case, the formulation yields

$$\frac{\partial^2\theta}{\partial s^2}+\beta^2 cos\varphi=0 \tag{1}$$

where s is the distance of a considering point $X$ to the free end of the beam, $\theta$ is the angle of slope of beam at that point, and $\beta$ is a constant which dependent on beam size, shape material and the applied load. The temporal form of Euler-Bernoulli beam formulation can be expressed as

$$EI\frac{\partial^4 X}{\partial s^4}+\rho_l\frac{\partial^2 X}{\partial t^2}=p \tag{2}$$

where $EI$ is the flexural rigidity of the beam, $\rho_l$ is the beam linear density, and $p$ is the load applied to the point $X$. However, just like the inverted pendulum model, the fluid drag in the cantilevered Euler-Bernoulli beam model is usually obtained based on the Stokes flow approximation, rather than solving the Navier–Stokes equations. Because of the Stokes flow approximation, this model is usually unable to consider the full interaction between the fluid and the structure (the impact of the structure on the flow is usually not considered). Thus, this model is not very accurate in non-Stokes flow cases or in the cases when the interplay between the fluid and the cilium is strong (e.g., to model the fluid propulsion due to the beating of motile cilia).

Nevertheless, the cantilevered Euler-Bernoulli beam model is used extensively to determine the mechanical properties of primary cilia under static load. Schwart et al. firstly used this model to evaluate the flexural rigidity of primary cilium based on an imaged-informed approach [27]. By assuming a constant flow velocity distribution along the cilium length, the Euler-Bernoulli equation was solved using both quadruple integration model and heavy elastic model, and the final bending profile of the cilium was obtained. The flexural rigidity was then iteratively updated during each calculation until the predicted bending shape matched the experimentally observed deflection. As a result, their approach yielded a flexural rigidity of $3.1 \pm 0.8 \times 10^{-23} Nm^2$ for the primary cilium, which is about one order less in magnitude than that of the motile cilium. Following their steps, this model is further developed to account for the initial cilium shape and base orientation [28, 29]. While Schwart et al. [27] estimated the flow drag based on two-dimensional (2D) laminar flow around a cylinder, Liu et al. [30] estimated it by numerically solving the Stokes equations, which improved the prediction accuracy greatly. They used the developed model to study the hydrodynamic interactions between multiple cilia. Their calculations suggested that shear stress experienced by the apical cell membrane alone may not be enough to elicit a calcium response, thus the primary cilium must assist to mediate such response via its deflection.

Despite that the cantilevered Euler-Bernoulli beam model is simple and popular in study cilium deflection, experimental observations deviate from this model have been reported in [5, 28, 31], where the base of the primary cilium can experience a certain degree of rotation rather than remain clamped or cantilevered. To incorporate basal rotation into the Euler-Bernoulli beam model, Resnick [5] modelled the basal end of the primary cilium as a nonlinear rotational spring. The reverse bending moment generated by the spring is then incorporated into the Euler-Bernoulli beam formulation as a boundary condition. With properly chosen linear and nonlinear spring constants, their model predicts a resultant oscillation amplitude and frequency well match their experimental measurements which are obtained with optical trap technique.

#### 1.1.2.3 Slender body theory

The slender body theory is widely used to simulate the dynamics of large-aspect ratio fibers immersed in Stokes flow, for instance in [32-34]. Its basic idea is to approximate the effect of the obstacle on its surrounding flow field by a distribution of singularities, whose strength is dependent on the imposed boundary conditions. In 2012, Young et al. used this theory to study the dynamics of primary cilium in shear flow [35]. In their simulations, the anchoring effect of the basal body is incorporated as a damped rotational spring, i.e., by coupling the elastic cilium with a cylindrical elastic shell. A good agreement is obtained between experimental measurements and numerical calculations, and the distribution of tension force along cilium and the membrane is investigated. Later, combined with an image-informed approach [36], the slender body theory is adopted to study mechanical and structural properties primary cilia of Madin-Darby Canine Kidney (MDCK) cells. The advantage of the slender body theory lies in its capability to handle large deformation of the slender object, because no fluid grid is required in the simulation due to the Stoke flow assumption. However, this conversely limits its application in many engineering problems where non-Stokes and even turbulent flow conditions are involved.

#### 1.1.2.4 Three-dimensional finite element model

The deflection of primary cilia can be also modelled by finite element method, especially in three-dimensional (3D) applications. Roydholm et al. [37] developed a 3D finite element (FE) model which includes three sub-ciliary components, i.e. the cilium microtubule core, the ciliary membrane, and the apical plasma membrane. In combined with an image-informed method, this model was used to study cilium bending and the resulting calcium signal. Based on their results, they speculated that the dynamic mechanical properties of the cilium and cell membrane serve to decode slow fluctuations in fluid flow. A more sophisticated FE model that aims to simulate the whole cell-cilium system was proposed by Khayyeri et al. [18] , in which the cell components includes nucleus, cortex, cytoplasm, microtubules and actin bundles, are carefully modelled in order to investigate the transmitting of mechanical stimuli among different organelles when the primary cilium is deflected. Their results suggest that the maximal strains induced by cilium deflection are located at the cilium base and in the cytoplasm. Despite of the robustness of FE model in 3D sub-ciliary modelling, the boundary condition used for each component still need further experimental verification as those additional degrees of freedom (masses, spring constants, etc.) have not yet been constrained. Besides, this method brought an increased computational load which would be when multiple cilia are needs to be simulated. Moreover, in the above-mentioned simulations which adopted these FE models, only a one-way decoupled fluid-structure interaction (FSI) were considered. This may reduce the overall accuracy of the simulations, as the recent two-way FSI studies on cilium dynamics suggests that the cilia array could have a considerable impact on the near-wall flow pattern [38].

### 1.1.2.5 Filament model

The filament model is different to the Euler-Bernoulli beam formulation which is derived based on small deflection assumption. The filament model drops this assumption thus can well describe the motion of the primary cilium which could undergo very large deformations. The model also includes a stretching force term to enforce the inextensibility condition. In this model, the motion equation for the filament is described as [39, 40]

$$\rho_d \frac{\partial^2 \boldsymbol{X}}{\partial t^2} = \frac{\partial}{\partial s}\left[T(s)\frac{\partial \boldsymbol{X}}{\partial s}\right] - K_b \frac{\partial^4 \boldsymbol{X}}{\partial s^4} + \boldsymbol{F_e} \tag{3}$$

where $\boldsymbol{X}$ is the position vector of the filament, $s$ the Lagrangian coordinate along the length of filament. $T(s)$ is the tension. $\boldsymbol{F_e}$ is the external load exerted on the filament, which can be a hydrodynamics force or simply a gravitational force. $K_b$ is bending rigidity of the filament, and $\rho_d$ denotes the difference in the linear density between the filament and the fluid. $\rho_d = 0$ therefore represents the neutrally buoyant, in that case the inertial term in the left-hand side can be dropped.

The filament model usually works under the framework of the immersed boundary method [41-43] and has been extensively used to study the flapping of a one-end tethered filament in a viscous flow [44-48]. The model was also used by Heys et al. [49] to study filiform hair (a structure locates on a pair of abdominal cerci of cricket which functions to sense the surrounding environment) motion in oscillating fluid flow, and more recently by Zhu et al. [50] to study the dynamics of motile cilia in respiratory tract. O'Connor et al. [38] exploited this model to study the dynamics of primary cilium in Poiseuille and Womersley flows, and Cui et al. [51] used this model to investigate the dynamics of primary cilia in a pulsatile blood flow. These simulations on cilium dynamics all considered a two-way FSI, however, most of them are limited only to 2D scenarios.

### 1.1.3 Research gap on the modelling of cilium dynamics

Based on the literature review given above, we have noticed some drawbacks of previous studies on cilium dynamics. The first one is the improperly modelling of the cilium basal body. A clamped boundary condition imposed at the cilium basal end fails to reproduce the basal rotation behaviors and can also not correctly predict the resonant oscillation amplitude and frequency in [52]. The second one is that, in many earlier studies, the flow is simplified (by using a steady Stokes flow approximation rather than solving the Navier–Stokes equations) and the influence of the primary cilia on the flow is assumed to be negligible. This assumption works only for the case of a single cilium or for a very sparse cilia array, however, would introduce a significant error when the cilia array is relatively dense. There are also some other studies such as [51, 52] that manage to simulate cilium deflection in a viscous fluid with a full-way FSI considered. However, these simulations are only 2D. One apparent drawback of the 2D simulations is that it may predict inaccurate drag force, as flow can only past above the primary cilia and has no variations in the third direction. Thus, in those 2D simulations, the authors are simulating the deflection of an infinitely wide elastic plate rather than a filament-like primary cilia. A 2D simulation is also unable to reproduce out of plane cilium motions which have been observed in [53].

## 1.2 Adhesion of a circulating tumor cell

### 1.2.1 Background and significance

The ability to metastasize is one of the most dangerous aspect of cancer. After detaching from the primary tumor, the tumor cells become circulating via invading either the blood circulatory or lymphatic system. After a successful invasion, the tumor cells become circulating and may be transported to a new site where they proliferate to form a new tumor [54]. During the metastasis, the majority of circulating tumor cells (CTCs) are trapped or lethally damaged on their way being delivered to various target organs, leading to cell death and ‘metastatic inefficiency’ [55]. To colonize a distant organ, one important and necessary step the CTCs must accomplish is to successfully adhere to the endothelial cells that form the wall of the microvessels, specifically, the post-capillary venules [56, 57]. Blocking tumor cell adherence to vessels therefore could be a promising stagey to prevent the metastasis of cancer. However, the mechanism behind the CTC adhesion is yet not fully revealed. The dynamics and adhesion of CTCs greatly depend on the circulation of the blood. CTCs usually are trapped in the first set of capillaries they encounter downstream from the point of entry. As a principal step in cancer metastasis, the adhesion of CTCs to the walls of a blood microvessel has attracted tremendous attention in the past few decades. A detailed review on the adhesion of tumor cells under hydrodynamic conditions can be found in [58] and a more recent review in [59]. Lots of progress has been made already, among them the recognition of receptor-ligand bonds for their role in mediating the adhesive dynamics of cells [60]. A successful cell adhesion not only relies on the competition between the adhesive and anti-adhesive forces, but also on the rates that bonds get formed and ruptured [61]. Apart from that, the adhesion process could also affected by the local microenvironment, such as the geometric features and local hemodynamic factors of the vasculature [62], and the tumor-derived and tumor associated-endothelial cell-derived exosomes uptaken by the organ-specific cells, which prepare the pre-metastatic niche [63].

Dong et al. [64] performed experiments on the adhesion and migration of human melanoma cells in shear flow using a modified Boyden chamber. Guo et al. [57] experimentally explored the arrest and adhesion of MDA-MB-231 cells (breast cancer) in rat mesenteric microvasculature. Marshall et al. [65] measured the force history in a receptor-ligand dissociation process using atomic force microscopy (AFM). In situ analysis on the adhesion of single CTC has also performed by Mao et al. [66] using microfluidic approaches. However, due to the complexity of tumor cell adhesion, rigorous measurement of the cellular interactions and the forces involved are still highly challenging to conduct *in vivo* at present. Simulations which can provide much detailed information would be a valuable tool in exploring the mechanism of cell adhesion under complex flow conditions. Rejniak [67] investigated the impact of cell deformability on their adhesion using a 2D numerical simulation. In their simulations, they examined the several parameters that related to the structure of the actin network, the adhesion links and the cell nucleus. Xiao et al. [68] numerically studied the adhesion of a CTC in a microvessel using the dissipative particle dynamics (DPD) method. Their study mainly focused on the impact of RBC aggregation on the CTC adhesion. Therefore, a straight vessel geometry was used in their simulations and no curvature effect was considered in their simulations

### 1.2.2 Research gap on CTC adhesion

Quite a few studies, both experiments and simulations, have investigated cell adhesions in a straight vessel. However, the recent experimental studies by Liu et al. [69], Guo et al. [57] and Zhang et al. [70, 71] reveal that CTCs are more likely to adhere to curved vessels and bifurcations of the microvasculature. To explore the mechanism underlying such adhesion phenomena, Yan et al. [72, 73] studied the effect of vessel curvature and wall shear stress on the adhesion of a circulating cell using a lattice Boltzmann simulation. Their simulation suggests that the simultaneous bond number will be increased when the vessel becomes curved, therefore the vessel curvature could enhance the adhesion probability of the CTC. However, the simulations performed by Yan et al. [72, 73] are two-dimensional, which cannot describe the cell's motion in the third direction. Apart from that, the cell in their simulations is assumed to be rigid, which may not reflect the real case. More importantly, the study by Rejniak [8] indicates that the cell deformability is closely related to its adhesion activity.

## 1.3 Objectives of this thesis

The first part of the thesis focuses on the modelling of cilium dynamics in pulsatile/oscillating flows. Its objectives include:

(1) To develop a proper 3D model for studying the dynamics of primary cilia in pulsatile/oscillating flow conditions.

(2) To numerically investigate the fluid-cilia interaction system, and evaluate the influence of some governing parameters, such as the peak Reynolds number, Womersley number, the cilium length, and the spacing interval on the system.

(3) To study cilium dynamics in generalized Newtonian fluid, and evaluate the impact of no-Newtonian effect on cilium dynamics.

The second part of the thesis aims to study the adhesion of a CTC in a curved microvessel using a 3D numerical modelling. Its objectives include:

(1) To characterize the differences in the dynamics and adhesion of a CTC in the straight and curved vessels.

(2) To investigate the effect of the applied driven force density (or the flow Reynolds number) and membrane bending modulus on CTC adhesion.

## 1.4 Organization of this thesis

The present thesis is organized in the following manner. Chapter 2 gives a brief introduction on our numerical method. In Chapter 3, our algorithm and codes are validated by simulating some benchmark problems. A grid independence study is also performed to find the effective grid resolutions for the present fluid-cilium interaction problem. In Chapter 4, we numerically study the dynamics of an cilia array in an oscillating Newtonian flow. The effect of the $Re_{peak}$, the $Wo$, the cilium length, and the spacing interval on fluid-cilia interaction are evaluated and discussed. The dynamics of primary cilia in oscillating no-Newtonian fluids is studied in Chapter 5. In Chapter 6, the adhesion of a CTC in a 3D curved microvessel is simulated, and the effect of the Reynolds number and bending stiffness of the membrane on the CTC adhesion is investigated. Chapter 7 presents the concluding remarks of this study with some recommendations for the future work.

# Chapter 2 Methodology

In this chapter, the methodologies involved in our modelling will be briefly introduced. For the cilium dynamics, the lattice Boltzmann method will be used to solve the flow dynamics. The primary cilium will be modelled as a filament with its basal end connected to a nonlinear rotational spring. The fluid-structure interaction will be handled by the immersed boundary method (IBM). For the CTC adhesion in a 3D curved vessel, the DPD is used to model the blood plasma and cytoplasm. The deformation of the cell is modeled by a spring-based network membrane model and the adhesion modeled by a probabilistic adhesive dynamics model.

## 2.1 Lattice Boltzmann method

The governing equations (or the Navier-Stokes (N-S) equations) for the incompressible viscous flow with external force is given by

$$\nabla \cdot \boldsymbol{u} = 0 \tag{4}$$

$$\rho\left(\frac{\partial \boldsymbol{u}}{\partial \mathrm{t}} + \boldsymbol{u} \cdot \nabla \boldsymbol{u}\right) = -\nabla \mathrm{p} + \mu \Delta \boldsymbol{u} + \boldsymbol{f_e} \tag{5}$$

where $\boldsymbol{u} = (u, v, w)$ is the fluid velocity, $\rho$ and $\mu$ are the density and dynamic viscosity of the fluid, respectively. p is the pressure and $\boldsymbol{f_e}$ is the external force from the immersed structural boundary.

Solving the N-S equations analytically is usually extremely difficult. We therefore turn to seek their approximate solutions using numerical approaches such as finite difference, finite volume, finite element, and boundary element methods.

In the past few decades, the LBM has evolved into a promising and versatile numerical tool for computational fluid dynamics (CFD). It has drawn tremendous attention in the past few decades due to its simple implementation and intrinsic parallel nature. Since its conception in 1980s, the LBM has been successfully applied to the simulations of a diversity of complex problems including multiphase flow [74, 75], turbulence flow [76, 77], particulate flow [78, 79], non-Newtonian fluid flow [80, 81] and even chemical reaction flow [82]. A more detailed review on the LBM and its applications can be found in [83, 84].

Historically, the LBM originated from the lattice gas automata (LGA), which is a simple particle-based approach to simulate fluid flows with a discrete lattice. In LGA, the fluid is considered as a cluster of particles residing on a regular lattice node, where they collide and stream following some prescribed rules. The first LGA model is introduced by Hardy, Pomeau, and de Pazzis (i.e., the HPP model) [85], which uses a 2D square lattice. In this model, the particles at a lattice node can stream to any of the four nearest neighboring nodes along those lattice links. The evolution of particles can be described by the following discrete kinetic equation

$$N_i(\boldsymbol{x} + \boldsymbol{e}_i \Delta t, t + \Delta t) = N_i(\boldsymbol{x}, t) + \Omega_i\big(N_i(\boldsymbol{x}, t)\big) \tag{6}$$

where $N_i(\boldsymbol{x}, t) = 0$ or $1$ denotes the particle number that moving with velocity $\boldsymbol{e}_i$ at position $\boldsymbol{x}$ and time $t$, and $\Omega_i$ is called the collision operator which alters the value of $N_i(\boldsymbol{x}, t)$ via collisions.

In the HPP model, a collision happens when two particles arrive at the same node but with opposite velocities, and as a result, their velocities will turn around 90° after the collision. However, due to the insufficient symmetry of the used lattice, the hydrodynamics variables in the HPP model do not satisfy the continuum equations. This drawback is removed in the later HFP model [86], which increases the lattice symmetry by using a triangular lattice (i.e. with six nearest neighbors). Despite the improvement, the LGA still suffers from statistical noise arising from the Boolean variables, the violation of the Galilean invariance, and the velocity- dependent pressure.

To eliminate the statistical noise in the LGA, McNamara and Zametti [87] proposed the first lattice Boltzmann equation (LBE) in 1988, where the Boolean variable $N_i$ is replaced by a distribution function $f_i$, which is a real variable that $\in [0, 1]$. In the LBE, the evolution of $f_i$ is similar to that of $N_i$ in LGA,

$$f_i(\boldsymbol{x} + \boldsymbol{e}_i \Delta t, t + \Delta t) - f_i(\boldsymbol{x}, t) = \Omega_i\big(f_i(\boldsymbol{x}, t)\big) \tag{7}$$

where $f_i(\boldsymbol{x}, t)$ is the distribution function which denotes the possibility to find a particle with velocity $\boldsymbol{e}_i$ at node $\boldsymbol{x}$, and time $t$.

The LBE retains the advantage of LGA in treating the collision operation locally. However, efficiently calculating this collision operator $\Omega_i$ is still a problem due to its complexity (it involves double integral over the velocity space). Apart from that, other problems in the LGA still exists because the equilibrium distribution is still Fermi-Dirac. To solve these problems, Chen et al. [88] and Qian et al. [89] proposed LBE models in which Fermi-Dirac statistics were abandoned, and therefore provided the freedom required for the equilibrium distribution to satisfy isotropy, Galilean invariance and to make the pressure independent of the velocity. In their models, a much simpler BGK collision operator was proposed, which locally relaxes the distribution function towards its equilibrium at a constant rate. The LBE with the BGK collision operator is known as the LBGK model, which is later been widely used in the LBM community due to its simplicity. The BGK collision operator is expressed as,

$$\Omega_i\big(f_i(\boldsymbol{x},t)\big) = -\frac{1}{\tau}\left[f_i(\boldsymbol{x},t) - f_i^{eq}(\boldsymbol{x},t)\right] \tag{8}$$

where $\tau$ is the relaxation time which defines the speed of this equilibration. $f_i^{eq}(\boldsymbol{x},t)$ is the equilibrium distribution function, which is chosen so that the LBE can recover the macroscopic N-S equations. It is calculated by,

$$f_i^{eq}(\boldsymbol{x},t) = \omega_i\rho\left[1 + \frac{\boldsymbol{e}_i\cdot\boldsymbol{u}}{c_s^2} + \frac{(\boldsymbol{e}_i\cdot\boldsymbol{u})^2}{2c_s^4} - \frac{\boldsymbol{u}^2}{2c_s^2}\right] \tag{9}$$

where $\omega_i$ is the weighting coefficient specific to the chosen velocity set $\boldsymbol{e}_i$, and $c_s$ is the model's speed of sound. In the D3Q19 (three-dimensional nineteen-velocity) lattice model (see Fig. 2.1) that used in our simulations, $c_s = c/\sqrt{3}$, and $c = \Delta x/\Delta t$ is the lattice speed, where $\Delta x$ and $\Delta t$ are the grid spacing and timestep size, respectively. In the D3Q19 lattice model, the weighting coefficients are given as,

$$\omega_i = \begin{cases} \frac{1}{3}, & i = 0 \\ \frac{1}{18}, & i = 1\sim 6 \\ \frac{1}{36}, & i = 7\sim 18 \end{cases} \tag{10}$$

The relaxation time $\tau$ is related to the kinetic viscosity $\upsilon$ by,

$$\upsilon = (\tau - 0.5)c_s^2\Delta t \tag{11}$$

In the practical implementation of an LBM code, the evolution is usually separated into a collision step and a streaming step as follows,

$$\text{Collison: } f_i^*(\boldsymbol{x},t) = f_i(\boldsymbol{x},t) - \tfrac{1}{\tau}\left[f_i(\boldsymbol{x},t) - f_i^{eq}(\boldsymbol{x},t)\right] \tag{12}$$

Streaming: $f_i(\boldsymbol{x} + \boldsymbol{e}_i \Delta t, t + \Delta t) = f_i^*(\boldsymbol{x}, t)$ (13)

Hereafter, the distribution function with an asterisk denotes the post-collision distribution function.

With all the updated distribution functions at hand, the macroscopic density, velocity, and pressure can be conveniently obtained by

$$\rho = \sum_i f_i \tag{14}$$

$$\boldsymbol{u} = \frac{1}{\rho} \sum_i \boldsymbol{e}_i f_i \tag{15}$$

$$p = c_s^2 \rho \tag{16}$$

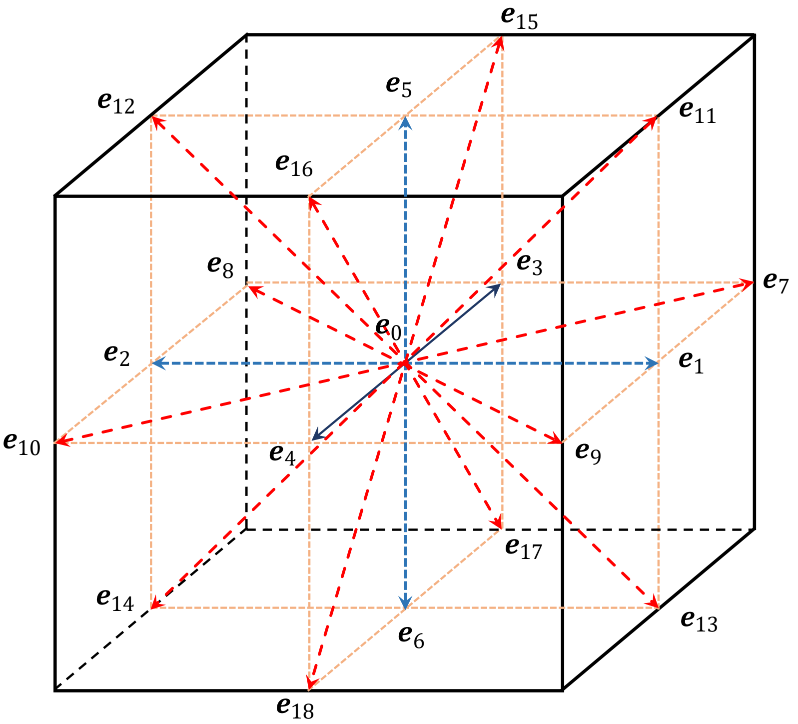

$\boldsymbol{e}_0 = (0,\ 0,\ 0)c$
$\boldsymbol{e}_1 = (1,\ 0,\ 0)c$
$\boldsymbol{e}_2 = (-1,\ 0,\ 0)c$
$\boldsymbol{e}_3 = (0,\ 1,\ 0)c$
$\boldsymbol{e}_4 = (0,\ -1,\ 0)c$
$\boldsymbol{e}_5 = (0,\ 0,\ 1)c$
$\boldsymbol{e}_6 = (0,\ 0,\ -1)c$
$\boldsymbol{e}_7 = (1,\ 1,\ 0)c$
$\boldsymbol{e}_8 = (-1,\ 1,\ 0)c$
$\boldsymbol{e}_9 = (1,\ -1,\ 0)c$
$\boldsymbol{e}_{10} = (-1,\ -1,\ 0)c$
$\boldsymbol{e}_{11} = (1,\ 0,\ 1)c$
$\boldsymbol{e}_{12} = (-1,\ 0,\ 1)c$
$\boldsymbol{e}_{13} = (1,\ 0,\ -1)c$
$\boldsymbol{e}_{14} = (-1,\ 0,\ -1)c$
$\boldsymbol{e}_{15} = (0,\ 1,\ 1)c$
$\boldsymbol{e}_{16} = (0,\ -1,\ 1)c$
$\boldsymbol{e}_{17} = (0,\ 1,\ -1)c$
$\boldsymbol{e}_{18} = (0,\ -1,\ -1)c$

Fig. 2.1 The D3Q19 lattice model

To couple the LBM with the immersed boundary method, we need the LBE with a forcing term. In this study, we adopt the split-forcing scheme proposed by Guo et al. [90] to handle external forces, which recovers the N-S equations with second-order accuracy. In this scheme, the forcing term is directly inserted to the evolution equation of the LBE (known as the second-forcing step).

$$f_i(\boldsymbol{x}+\boldsymbol{e}_i\Delta t, t+\Delta t) = f_i(\boldsymbol{x},t) - \frac{1}{\tau}\left[f_i(\boldsymbol{x},t) - f_i^{eq}(\boldsymbol{x},t)\right] + \boldsymbol{F}_i\Delta t \tag{17}$$

And the forcing term $\boldsymbol{F}_i$ is given as,

$$\boldsymbol{F}_i = \left(1-\frac{1}{2\tau}\right)\omega_i\left(\frac{\boldsymbol{e}_i-\boldsymbol{u}}{c_s^2}+\frac{\boldsymbol{e}_i\cdot\boldsymbol{u}}{c_s^4}\boldsymbol{e}_i\right)\boldsymbol{f}_{\boldsymbol{e}} \tag{18}$$

where $\boldsymbol{f}_{\boldsymbol{e}}$ is the external force density. The velocity (momentum) in the split-forcing LBE is also redefined to include the external force effect as following (known as the first-forcing step).

$$\boldsymbol{u} = \frac{1}{\rho}\left(\sum_i \boldsymbol{e}_i f_i + \frac{\Delta t}{2}\boldsymbol{f}_e\right) \tag{19}$$

### 2.1.1 LBM with MRT collision operator

The LBGK model greatly alleviates the complexity in calculating the collision term in the LBE. However, it may face stability issues due to that all moments relax to their equilibria with the same rate [91, 92]. Moreover, the result in the LBGK model may exhibit unphysical viscosity-dependent feature, which contradicts to the fundamental physical requirement that the solutions should be uniquely determined by their non-dimensional physical parameters [93]. These defects can be removed by using the multiple-relaxation-time (MRT) collision operator, in which the moments relax to their equilibria at their own rates that are not necessarily equal. The MRT-LBM has been proved to have a better stability and accuracy over the LBGK model [94], thus is more preferable to incorporate with IBM to solve fluid-structure-interaction problems.

As the MRT-LBM enables the local prescription of the relaxation parameters without any change in viscosity, the solutions obtained can be viscosity-independent.

In the MRT frame, the evolution equation of the LBE is rewritten in the moment form, and the one with forcing term is given below [95].

$$\begin{aligned} &|f(\boldsymbol{x}+\boldsymbol{e}_{\alpha}\Delta t, t+\Delta t)\rangle - |f(\boldsymbol{x},t)\rangle \\ &\qquad = -\mathbf{M}^{-1}\left\{\hat{\mathbf{S}}[|m(\boldsymbol{x},t)\rangle - |m^{eq}(\boldsymbol{x},t)\rangle] + \left(\mathbf{I}-\frac{\hat{\mathbf{S}}}{2}\right)|\mathrm{F}(\boldsymbol{x},t)\rangle\right\} \end{aligned} \tag{20}$$

where the notation $|\cdot\rangle$ denotes column vector, i.e. $|f\rangle \equiv (f_0, f_1, \cdots, f_{18})^T$. $\mathbf{I}$ is the identity matrix. $|m\rangle$ is the moment form of $|f\rangle$ and $|m^{eq}\rangle$ is its corresponding equilibrium value, and in our D3Q19 lattice model, they are defined respectively as [96],

$$|m\rangle = (\rho, e, \varepsilon, j_x, j_y, q_x, j_y, q_y, j_z, q_z, 3p_{xx}, 3\pi_{xx}, p_{ww}, \pi_{ww}, p_{xy}, p_{yz}, t_x, t_y, t_z)^{\mathrm{T}} \tag{21}$$

and

$$\begin{aligned} |m^{eq}\rangle = \Big(&\rho, -\rho(11-19|\boldsymbol{u}|^2), \rho(\alpha-\beta|\boldsymbol{u}|^2), j_x, -\frac{2}{3}j_x, j_y, -\frac{2}{3}j_y, j_z, -\frac{2}{3}j_z, \\ &\frac{1}{\rho_0}\left(j_x^2-j_y^2-j_z^2\right),\ \frac{\gamma}{\rho_0}\left(j_x^2-j_y^2-j_z^2\right),\ \frac{1}{\rho_0}\left(j_y^2-j_z^2\right),\ \frac{\gamma}{\rho_0}\left(j_y^2-j_z^2\right),\ \frac{1}{\rho_0}j_xj_y \\ &\frac{1}{\rho_0}j_yj_z,\ \frac{1}{\rho_0}j_zj_x,\ 0,\ 0,\ 0\Big)^{\mathrm{T}} \end{aligned} \tag{22}$$

where $e$ is the energy. $j_x$, $j_y$ and $j_z$ are the components of the moment density $\rho\boldsymbol{u}$. $q_x$, $q_y$, and $q_z$ are the energy flux components, $p_{xx}$, $p_{ww}$ and $p_{xy}$, $p_{yz}$, and $p_{yz}$ relate to the symmetric and traceless strain-rate tensors. $\pi_{xx}$ and $\pi_{ww}$ are the fourth-order moments while $t_x$, $t_y$, and $t_z$ are the third-order moments. $\alpha$, $\beta$, and $\gamma$ are free parameters, and they are chosen as 3, -5.5, and -0.5 in our simulations, respectively.

**M** is a 19×19 transformation matrix which defines the mapping between $f$ and $m$, i.e., $|m\rangle = \mathbf{M}|f\rangle$, and in the D3Q19 lattice model,

$$\mathbf{M} =$$

$$\begin{vmatrix}
1 & 1 & 1 & 1 & 1 & 1 & 1 & 1 & 1 & 1 & 1 & 1 & 1 & 1 & 1 & 1 & 1 & 1 & 1 \\
-30 & -11 & -11 & -11 & -11 & -11 & -11 & 8 & 8 & 8 & 8 & 8 & 8 & 8 & 8 & 8 & 8 & 8 & 8 \\
12 & -4 & -4 & -4 & -4 & -4 & -4 & 1 & 1 & 1 & 1 & 1 & 1 & 1 & 1 & 1 & 1 & 1 & 1 \\
0 & 1 & -1 & 0 & 0 & 0 & 0 & 1 & -1 & 1 & -1 & 1 & -1 & 1 & -1 & 0 & 0 & 0 & 0 \\
0 & -4 & 4 & 0 & 0 & 0 & 0 & 1 & -1 & 1 & -1 & 1 & -1 & 1 & -1 & 0 & 0 & 0 & 0 \\
0 & 0 & 0 & 1 & -1 & 0 & 0 & 1 & 1 & -1 & -1 & 0 & 0 & 0 & 0 & 1 & -1 & 1 & -1 \\
0 & 0 & 0 & -4 & 4 & 0 & 0 & 1 & 1 & -1 & -1 & 0 & 0 & 0 & 0 & 1 & -1 & 1 & -1 \\
0 & 0 & 0 & 0 & 0 & 1 & -1 & 0 & 0 & 0 & 0 & 1 & 1 & -1 & -1 & 1 & 1 & -1 & -1 \\
0 & 0 & 0 & 0 & 0 & -4 & 4 & 0 & 0 & 0 & 0 & 1 & 1 & -1 & -1 & 1 & 1 & -1 & -1 \\
0 & 2 & 2 & -1 & -1 & -1 & -1 & 1 & 1 & 1 & 1 & 1 & 1 & 1 & 1 & -2 & -2 & -2 & -2 \\
0 & -4 & -4 & 2 & 2 & 2 & 2 & 1 & 1 & 1 & 1 & 1 & 1 & 1 & 1 & -2 & -2 & -2 & -2 \\
0 & 0 & 0 & 1 & 1 & -1 & -1 & 1 & 1 & 1 & 1 & -1 & -1 & -1 & -1 & 0 & 0 & 0 & 0 \\
0 & 0 & 0 & -2 & -2 & 2 & 2 & 1 & 1 & 1 & 1 & -1 & -1 & -1 & -1 & 0 & 0 & 0 & 0 \\
0 & 0 & 0 & 0 & 0 & 0 & 0 & 1 & -1 & -1 & 1 & 0 & 0 & 0 & 0 & 0 & 0 & 0 & 0 \\
0 & 0 & 0 & 0 & 0 & 0 & 0 & 0 & 0 & 0 & 0 & 0 & 0 & 0 & 0 & 1 & -1 & -1 & 1 \\
0 & 0 & 0 & 0 & 0 & 0 & 0 & 0 & 0 & 0 & 0 & 1 & 1 & -1 & -1 & 0 & 0 & 0 & 0 \\
0 & 0 & 0 & 0 & 0 & 0 & 0 & 1 & -1 & 1 & -1 & -1 & 1 & -1 & 1 & 0 & 0 & 0 & 0 \\
0 & 0 & 0 & 0 & 0 & 0 & 0 & -1 & -1 & 1 & 1 & 0 & 0 & 0 & 0 & 1 & -1 & 1 & -1 \\
0 & 0 & 0 & 0 & 0 & 0 & 0 & 0 & 0 & 0 & 0 & 1 & 1 & -1 & -1 & -1 & -1 & 1 & 1
\end{vmatrix}$$

$\hat{\mathbf{S}}$ is the non-negative 19×19 diagonal collision matrix, whose element defines the relaxation rate for its specific moment. Based on linear stability analysis [97], the relaxation parameters are chosen as,

$$\hat{\mathbf{S}} \equiv diag\{s_0, s_1, s_2, s_3, s_4, s_5, s_6, s_7, s_8, s_9, s_{10}, s_{11}, s_{12}, s_{13}, s_{14}, s_{15}, s_{16}, s_{17}, s_{18}\} \qquad (23)$$

where $s_1$=1.19, $s_2$=$s_{10}$=$s_{12}$=1.4, $s_4$=$s_6$=$s_8$=1.2, $s_{16}$=$s_{17}$=$s_{18}$=1.98, and $s_9$=$s_{11}$=$s_{13}$= $s_{14}$=$s_{15}$= $1/(3\nu/\Delta t + 0.5)$. In the MRT-LBM without the forcing term, the value of the relaxation times for the conserved moments ($s_0$, $s_3$, $s_5$, and $s_7$) are usually set to zero as they will not affect the result at all. However, in the case when forcing term is included, their values are no longer insignificant and they need to be nonzero [98, 99]. In our study we follow Premnath et al.[100] to set them to unity.

In the MRT frame, $|\mathrm{F}(\boldsymbol{x},t)\rangle = \mathbf{M}|f_e(\boldsymbol{x},t)\rangle$, and $|f_e(\boldsymbol{x},t)\rangle$can be calculated as [101, 102],

$$|f_e(\boldsymbol{x},t)\rangle = \frac{[\boldsymbol{e}_\alpha - \boldsymbol{u}(\boldsymbol{x},t)]\boldsymbol{f}_e(\boldsymbol{x},t)}{\rho c_s^2}|f^{eq}(\boldsymbol{x},t)\rangle \tag{24}$$

where $\boldsymbol{f}_e(\boldsymbol{x},t)$ is the external force density on the fluid, and $|f^{eq}(\boldsymbol{x},t)\rangle$ are the equilibrium distribution functions.

In this study, the BGK collision operator was used for the simulation of Non-Newtonian fluid flow only due to its efficiency (as will be introduced in Chapter 5 that the Non-Newtonian fluid flow simulation will greatly increase the computational cost). For the other simulations, the MRT collision operator was adopted due to its improved stability and accuracy.

### 2.1.2 Frequently used boundary conditions in the LB simulations

Boundary conditions (BCs) play a significant role in the LB simulations and should be treated with great care. The LBM is theoretically second-order accurate for the weakly compressible Navier-Stokes (N-S) equation [103, 104]. However, the accuracy order can be degraded if BCs are not properly constructed or specified (to accommodate the second-order accuracy of LBM in a grid-independent manner, the boundary scheme need to have a higher-order accuracy). The BCs also affect the stability of the LB simulations [105], though they are applied to only a small portion of the simulation domain. The way to specify a BC in the LB simulation is very different with that in conventional N-S solvers where the macroscopic variables of interest (e.g. velocity or pressure) are usually specified. In LB simulations, one must specify all the unknown distribution functions of the boundary nodes that are pointing to the fluid domain to attain a desired macro quantity indirectly. This is usually a more difficult task as the distribution functions have more degrees of freedom. There are many LB boundary schemes proposed in the literature and we will give a brief introduction on a few of them which are frequently used. For simplicity and without lose generality, we will use the D2Q9 lattice model and a 2D computational domain shown in Fig. 2.2 as an example to illustrate how to implement them. Note that most of them can be straightforwardly extended to 3D scenarios.

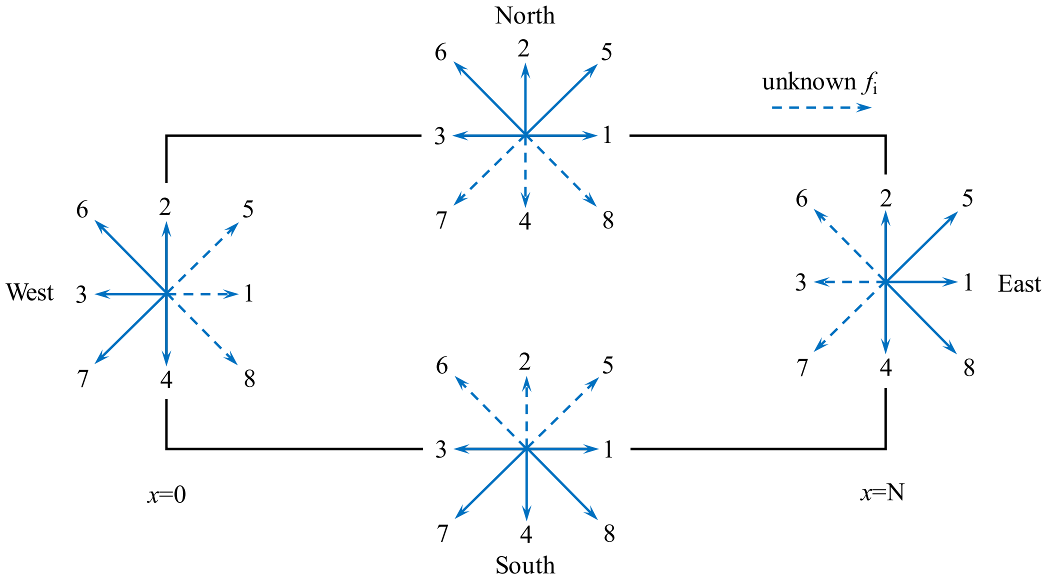

Fig. 2.2 Schematics of the distribution functions at the four boundaries with D2Q9 lattice model

### 2.1.2.1 Periodic boundary condition

The periodic BC may be the simplest BC to implement in the LB simulations. In a periodic flow pattern, the fluid leaving the domain on one side will, instantaneously, re-enter at the opposite side. This can be easily achieved in the LBM by making the two opposite boundary nodes neighbors during the streaming of distribution functions. This BC must work in pairs. Taking the west and east boundaries in Fig. 2.2 as an example, the periodicity in $x$-direction can be achieved by

$$f_i(x = 0, t + 1) = f_i^*(x = N, t) \tag{25}$$

$$f_j(x = N, t + 1) = f_j^*(x = 0, t) \tag{26}$$

where $i$=1, 5, 8 and $j$=3, 6, 7, are the indexes of the unknown distribution functions at the west and east boundaries, respectively.

### 2.1.2.2 No-slip boundary conditions

For stationary solid walls, the no-slip BC can be easily implemented with the bounce-back (BB) scheme. The BB scheme assumes that when a particle distribution function hits a solid wall, it will be reflected back to where it comes from in the streaming step. In our simulations, we used the halfway bounce-back scheme due to its second-order accuracy for walls aligned with the grids and it is more accurate in unsteady flow simulations [106]. Taking the south boundary in Fig. 2.2 as an example, the no-slip BC can be achieved by

$$\begin{aligned} f_2(\boldsymbol{x}_b, t + 1) &= f_4^*(\boldsymbol{x}_b, t) \\ f_5(\boldsymbol{x}_b, t + 1) &= f_7^*(\boldsymbol{x}_b, t) \\ f_6(\boldsymbol{x}_b, t + 1) &= f_8^*(\boldsymbol{x}_b, t) \end{aligned} \tag{27}$$

where $\boldsymbol{x}_b$ stands for the boundary nodes. However, it should be noted that in the halfway BB scheme, the wall is actually placed approximately a half lattice away from the boundary nodes. This can be easily understood by looking at the bounce-back process depicted in Fig. 2.3.

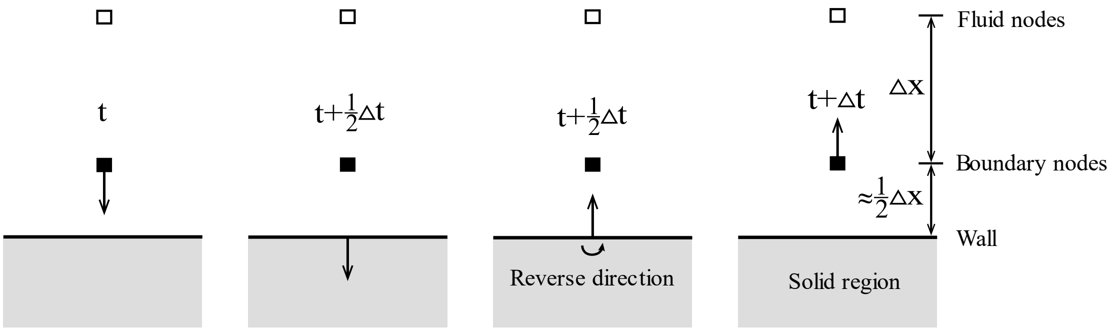

Fig. 2.3 Schematics of the halfway bounce-back process

The BB scheme is a big strength of the LBM. When combined with a “staircase” approximation on the boundary, the BB scheme can efficiently handle complex solid geometries, such as porous media. Besides its easy implementation, the BB scheme can also exactly conserve the mass at rest walls and has a sound stability even when the relaxation time $\tau$ is close to 0.5. However, the solution will be viscosity-dependent when the BB scheme is used in the BGK-LBM. The exact location of the wall will vary with the $\tau$. In the cases when the wall is not aligned with the grids, the BB scheme will have to approximate the wall with “staircase” shapes, which decreases its accuracy to first-order [107, 108].

In the case when the wall is not stationary, one can use the corrected BB scheme [78]. In this scheme, when a distribution function hits the wall, it will bounce back with an appropriate adjustment of its momentum.

$$f_{-i}(\boldsymbol{x}_b, t+1) = f_i^*(\boldsymbol{x}_b, t) - 2\omega_i \rho_w \frac{\boldsymbol{e}_i \cdot \boldsymbol{U}_w}{c_s^2} \tag{28}$$

where -$i$ denotes the opposite direction of $i$, i.e., $\boldsymbol{e}_{-i} = -\boldsymbol{e}_i$. $\rho_w$ and $\boldsymbol{U}_w$ are the density and velocity of the wall, respectively.

One can also enforce the no-slip BC with the non-equilibrium extrapolation method

(NEEM) proposed by Guo et al. [109]. Unlike the BB scheme which focusing on finding the unknown distribution functions, the NEEM will replace the boundary distribution functions at all directions (nine for D2Q9 lattice model). The distribution function consists of an equilibrium and a non-equilibrium part. In the NEEM, the equilibrium part of the distribution function is computed locally, while the non-equilibrium part (the part that related to the velocity gradient) comes from the nearest fluid node at the boundary normal direction. The NEEM can be expressed by

$$f_i(\boldsymbol{x}_b, t) = f_i^{eq}(\rho_w, \boldsymbol{u}_w) + \left(f_i(\boldsymbol{x}_n, t) - f_i^{eq}(\rho_n, \boldsymbol{u}_n)\right) \tag{29}$$

where $\boldsymbol{x}_n$ is the neighboring fluid node of $\boldsymbol{x}_b$ along the boundary normal direction and $\rho_n$ and $\boldsymbol{u}_n$ are the density and velocity of $\boldsymbol{x}_n$, respectively.

The NEEM is second-order accurate [109] and is naturally appliable to both 2D and 3D applications. However, this method may not strictly conserve the mass and could be a source of instability in the LB simulations.

The halfway BB scheme and the NEEM are second-order accurate for flat boundaries that are aligned with lattice links. For curved or inclined wall boundaries, their accuracy both degenerate to first order. In those cases, one can use the curved BCs proposed in [107, 110, 111] to achieve a higher-order accuracy.

#### 2.1.2.3 Symmetry boundary condition

When there is a symmetry plane exists, one can half the simulation domain and use a symmetry boundary condition to reduce computation cost. The symmetry boundary condition can be implemented easily by obtaining those unknown distribution functions through mirroring. Considering a symmetry boundary aligned with the lattice links, the symmetry boundary condition can be implemented with

$$f_j(\boldsymbol{x}_b, t) = f_i(\boldsymbol{x}_b, t) \tag{30}$$

where $i$ and $j$ denote those known and unknown distribution functions respectively at a boundary node $\boldsymbol{x}_b$. The tangential and normal velocities of the $j$th distribution function are related to that of the $i$th distribution function by $\boldsymbol{e}_{j,t} = \boldsymbol{e}_{i,t}$, and $\boldsymbol{e}_{j,n} = -\boldsymbol{e}_{i,n}$.

#### 2.1.2.4 Open boundary conditions

It is always convenient to specify a velocity or pressure boundary at the inlet/outlet with the NEEM. However, the Chapman-Enskog analysis suggests that a boundary scheme with second-order accuracy is not enough to support the level of exactness of the LB solution in the bulk [93].

The non-equilibrium bounce-back method (NEBBM, also called the Zou-He boundary scheme) [112] has a superior accuracy over the NEEM. It has a formally third-order accuracy for straight boundaries that aligned with the grids. To use the NEBBM, one needs to specify two macro quantities out of three (i.e. $\rho_{in}$, $u_x$, and $u_y$) at the boundary. Consider a pressure (density) inlet at the west boundary in Fig. 2.2, and a given tangential velocity component $u_y$ at the boundary, we immediately have the following three equations.

$$\rho_{in} = f_0 + f_2 + f_3 + f_4 + f_6 + f_7 + (f_1 + f_5 + f_8) \tag{31}$$

$$\rho_{in} u_x = (f_1 + f_5 + f_8) - f_3 - f_6 - f_7 \tag{32}$$

$$\rho_{in} u_y = (f_5 - f_8) + f_2 - f_4 + f_6 - f_7 \tag{33}$$

Consistency of Equations (31) and (32) gives,

$$u_x = 1 - \frac{[f_0 + f_2 + f_4 + 2(f_3 + f_6 + f_7)]}{\rho_{in}} \tag{34}$$

There are 4 unknown variables (i.e. $f_1$, $f_5$, $f_8$, and $u_x$) to be determined, yet we have only three equations at hand. To close the system, Zou and He [112] proposed the fourth equation by evaluating the non-equilibrium part of the wall-normal distribution function using the bounce-back rule. In our example, the equation is

$$f_1 - f_1^{eq} = f_3 - f_3^{eq} \tag{35}$$

which yields

$$f_1 = f_3 + \frac{2}{3}\rho_{in}u_x \tag{36}$$

The other two unknown $f$ then can be determined as follows

$$f_5 = f_7 - \frac{1}{2}(f_2 - f_4) + \frac{1}{6}\rho_{in}u_x + \frac{1}{2}\rho_{in}u_y \tag{37}$$

$$f_8 = f_6 + \frac{1}{2}(f_2 - f_4) + \frac{1}{6}\rho_{in}u_x - \frac{1}{2}\rho_{in}u_y \tag{38}$$

The velocity BC in the NEBBM can be determined in a similar manner. Compared with the NEEM, the NEBBM has one-order higher accuracy for straight boundaries. However, in NEBBM, the corner nodes need to be specially treated and the NEBBM is also difficult to apply in 3D scenarios. In 3D cases where velocity or pressure BCs are desired, we recommend to use the boundary scheme proposed in [113].

If the flow domain to be simulated is ideally very large or infinite in one or more dimensions, one can truncate the domain to a finite size and use an outflow BC to save computational cost. In LB simulations, there are three frequently used outflow BCs. The first one is the Neumann boundary condition (NBC), which is usually applied when the flow at the outlet is fully developed. The NBC can be expressed as,

$$\frac{\partial \varphi}{\partial x} = 0 \tag{39}$$

where $\varphi$ is the interested variable such as $\rho$ and $\boldsymbol{u}$. $x$ is the boundary normal direction. The NBC can be implemented in the LBM easily as,

$$f_i(x = N, t) = f_i(x = N - 1, t) \tag{40}$$

The second one is the convective boundary condition (CBC),

$$\frac{\partial \varphi}{\partial t} + U \frac{\partial \varphi}{\partial x} = 0 \tag{41}$$

where $U$ is a typical velocity normal to the outlet boundary [114], which is usually taken as the average $u$-velocity in the upstream. The CBC can be discretized by a first-order finite difference scheme as following.

$$\frac{\varphi(N, t + 1) - \varphi(N, t)}{\Delta t} + U \frac{\varphi(N, t + 1) - \varphi(N - 1, t + 1)}{\Delta x} = 0 \tag{42}$$

which yields

$$\varphi(N, t + 1) = \frac{\varphi(N, t) + \alpha \cdot \varphi(N - 1, t + 1)}{1 + \alpha} \tag{43}$$

where $\alpha = U\Delta t/\Delta x$. The CBC is implemented in the LBM by calculating the boundary distribution functions with,

$$f_i(N, t + 1) = \frac{f_i(N, t) + \alpha \cdot f_i(N - 1, t + 1)}{1 + \alpha} \tag{44}$$

The third outflow BC is the extrapolation boundary condition which is specially designed for LB simulations. It can be expressed as,

$$f_i(N, t + 1) = 2f_i(N - 1, t + 1) - f_i(N - 2, t + 1) \tag{45}$$

### 2.1.3 Shear stress and wall shear stress evaluation in the LBM

In conventional N-S solvers, one needs to calculate the velocity gradient $\nabla \boldsymbol{u}$ through finite-difference method to obtain the shear stress field, which require a lot of computation. In the LBM, the shear stress tensor can be calculated efficiently with no need to calculate $\nabla \boldsymbol{u}$. Moreover, the calculation is totally local, which could be a big advantage if the code is being implemented in parallel. These features make LBM a popular tool in blood flow simulations, where the shear stress field and the wall-shear stress (WSS) distribution are usually paid special attention to [80, 115]. In the LBM, the deviatoric stress tensor in *D* spatial dimensions can be locally evaluated by [116],

$$\tau_{\alpha\beta} = -\left(1 - \frac{1}{2\tau}\right) \sum_i \left(e_{i\alpha} e_{i\beta} - \frac{\delta_{\alpha\beta}}{D} \boldsymbol{e}_i \cdot \boldsymbol{e}_i\right) f_i^{neq} \tag{46}$$

where $\delta_{\alpha\beta}$ is the Kronecker delta, and $f_i^{neq} = f_i - f_i^{eq}$. The hydrostatic stress (pressure) in the LBM is given by $p = c_s^2 \rho$. The stress tensor then can be obtained by,

$$\sigma_{\alpha\beta} = -p\, \delta_{\alpha\beta} + \tau_{\alpha\beta} \tag{47}$$

The WSS is a vector that is defined as the tangential force per unit area exerted by a solid boundary on a fluid in motion. With the stress tensor $\boldsymbol{\sigma}$, the WSS vector $\boldsymbol{\tau}^{wss}$ can be computed by [117],

$$\boldsymbol{\tau}^{wss} = \boldsymbol{T} - (\boldsymbol{T} \cdot \boldsymbol{n})\boldsymbol{n} \tag{48}$$

or in tensor notation,

$$\tau_\alpha^{wss} = \delta_{\alpha\beta}\, n_\beta - \left(\sigma_{\beta\gamma} n_\beta n_\gamma\right) n_\alpha \tag{49}$$

where $\boldsymbol{T} = \boldsymbol{\sigma} \cdot \boldsymbol{n}$ is the traction vector. $\boldsymbol{n} = (n_1, n_2, n_3)$ is the unit normal vector at the wall, which needs to be determined before calculating the WSS vector. It is common to report only the magnitude of the WSS vector, simply called the WSS ($\tau^{wss}$=|$\boldsymbol{\tau}^{wss}$|). In the case when halfway bounce-back scheme is used at the boundary, the wall location is shifted a half lattice away from the boundary. To evaluate the WSS on site, it is recommended to first evaluate the WSS at the boundary and near-boundary nodes, then interpolate the WSS at the wall nodes. This will bring a higher order accuracy in WSS evaluation according to [118].

## 2.2 Cilium dynamics

As the primary cilium has a large aspect ratio (its length usually ranges from 1.8 to11.1μm, while its diameter is about 0.2μm [21]), its dynamics can be reduced to a one-dimensional description (i.e. treated as a filament) by averaging the underlying balance laws over its cross-sections. Based on this, it's motion equation can be described as [39, 40]

$$\rho_d \frac{\partial^2 \boldsymbol{X}}{\partial t^2} = \frac{\partial}{\partial s}\left[T(s)\frac{\partial \boldsymbol{X}}{\partial s}\right] - K_b \frac{\partial^4 \boldsymbol{X}}{\partial s^4} + \boldsymbol{F_{fluid}} \tag{50}$$

where $\boldsymbol{X}$ is the position of the cilium, $s$ the Lagrangian coordinate along the length of cilium. $\boldsymbol{F_{fluid}}$ is the hydrodynamic force exerted on the cilium, and $K_b$ the bending rigidity of the cilium. $\rho_d$ is the difference in the linear density between the cilium and the fluid it immersed in (i.e., $\rho_d = (\rho_c - \rho) * A$, where $\rho_c$ is the density of the cilium and $A$ the cross-sectional area of the cilium), so $\rho_d = 0$ represents the neutrally buoyant case. The first and second terms in the right-hand side of Equation (50) represent the tensile and bending forces, respectively. $T(s)$ is the tension which enforces the inextensibility condition and can be calculated by

$$T(s) = K_s\left[\left(\frac{\partial \boldsymbol{X}}{\partial s}\cdot\frac{\partial \boldsymbol{X}}{\partial s}\right)^{\frac{1}{2}} - 1\right] \tag{51}$$

where $K_s$ is a stretching coefficient that defines the extensibility of the cilium. In our problems of interest, stretching of the primary cilium is not significant compared to its bending. Thus, we assume that the primary cilium is inextensible, and use a large value of $K_s$ in our simulations to enforce this constraint, as did by Zhu and Peskin [48] and Tian et al. [46]. The value of $K_s$ is chosen that the maximal stretch ratio is less than 0.5% throughout the simulations. Here, a small stretch ratio is allowed because an exceeding large value of $K_s$ could make the simulation unstable, however, a too small $K_s$ should be avoid as it will introduce unacceptable error to the solution [45].

While the fluid is defined on these fixed Eulerian points, the cilium is represented by a set of isometric Lagrangian points $\boldsymbol{X}(s_i, \mathrm{t})$, *i=0,1,…,Nb*. In our modelling, $s_0=0$ represents the cilium's basal end, and $s_{Nb}=L$ the cilium's distal end (i.e. cilium tip), where $L$ is the cilium length. We discretize the right-hand side of Eq. (50) in space with a central finite difference (FD) scheme.

$$\rho_d \frac{\partial^2 \boldsymbol{X}}{\partial t^2} = \frac{T_{i+\frac{1}{2}} \left[\frac{\partial \boldsymbol{X}}{\partial s}\right]_{i+\frac{1}{2}} - T_{i-\frac{1}{2}} \left[\frac{\partial \boldsymbol{X}}{\partial s}\right]_{i-\frac{1}{2}}}{\Delta s} - K_b \frac{\boldsymbol{X}_{i+2} - 4\boldsymbol{X}_{i+1} + 6\boldsymbol{X}_i - 4\boldsymbol{X}_{i-1} + \boldsymbol{X}_{i-2}}{\Delta s^4} + \boldsymbol{F}_{\boldsymbol{fluid}} \tag{52}$$

where $\partial \boldsymbol{X}/\partial \mathrm{s}$ is the local unit tangent vector which is evaluated at the segment center via a first-order central FD stencil as following.

$$\left[\frac{\partial \boldsymbol{X}}{\partial s}\right]_{i+\frac{1}{2}} = \frac{\boldsymbol{X}_{i+1} - \boldsymbol{X}_i}{\Delta s}, \text{ and } \left[\frac{\partial \boldsymbol{X}}{\partial s}\right]_{i-\frac{1}{2}} = \frac{\boldsymbol{X}_i - \boldsymbol{X}_{i-1}}{\Delta s} \tag{53}$$

Similarly, the tension at the segment center is calculated by

$$T_{i+\frac{1}{2}} = K_s \left( \left| \frac{\boldsymbol{X}_{i+1} - \boldsymbol{X}_i}{\Delta s} \right| - 1 \right), \text{ and } T_{i-\frac{1}{2}} = K_s \left( \left| \frac{\boldsymbol{X}_i - \boldsymbol{X}_{i-1}}{\Delta s} \right| - 1 \right) \tag{54}$$

The treatment of the left-hand side of Eq. (50) (the temporal discretization) requires more care, as it is closely related to the stability of the explicit structure solver whose time-marching scheme should not violate the Courant–Friedrichs–Lewy (CFL) condition. Here the three-step Runge–Kutta method is adopted to advance the position and velocity of the Lagrangian points from time step $n$ to $n+1$.

Step 1

$$\boldsymbol{U}^{(1)} = \boldsymbol{U}^{n} + \Delta t \frac{\partial^2 \boldsymbol{X}^{n}}{\partial t^2} \tag{55}$$

$$\boldsymbol{X}^{(1)} = \boldsymbol{X}^{n} + \Delta t \boldsymbol{U}^{n} \tag{56}$$

Step 2

$$\boldsymbol{U}^{(2)} = \frac{3}{4}\boldsymbol{U}^{n} + \frac{1}{4}\left(\boldsymbol{U}^{(1)} + \Delta t \frac{\partial^2 \boldsymbol{X}^{(1)}}{\partial t^2}\right) \tag{57}$$

$$\boldsymbol{X}^{(2)} = \frac{3}{4}\boldsymbol{X}^{n} + \frac{1}{4}\left(\boldsymbol{X}^{(1)} + \Delta t \boldsymbol{U}^{(1)}\right) \tag{58}$$

Step 3

$$\boldsymbol{U}^{n+1} = \frac{1}{3}\boldsymbol{U}^{\boldsymbol{n}} + \frac{2}{3}\left(\boldsymbol{U}^{(2)} + \Delta t \frac{\partial^2 \boldsymbol{X}^{(2)}}{\partial t^2}\right) \tag{59}$$

$$\boldsymbol{X}^{n+1} = \frac{1}{3}\boldsymbol{X}^{n} + \frac{2}{3}\left(\boldsymbol{X}^{(2)} + \Delta t \boldsymbol{U}^{(2)}\right) \tag{60}$$

where superscript $n$ and $n+1$ are the time-step index. $\boldsymbol{U}^{(1)}$ and $\boldsymbol{U}^{(2)}$ are the intermediate velocities, $\boldsymbol{X}^{(1)}$ and $\boldsymbol{X}^{(2)}$ the intermediate positions.

## 2.3 Fluid-structure interaction

The interaction between the fluid and the cilium is handled by the immersed boundary method (IBM). The IBM is a mathematical framework originally developed by Peskin in 1972 to simulate blood flow through a heart valve [41-43]. Since its conception, the IBM has found a wide variety of applications in computational biofluid mechanics (e.g. the deformation of red blood cells [119], the swimming of sperm [120] and eel [121], and the insect flight [122]) and has evolved into a generalized framework for studying fluid-structure interaction (FSI) problems. In the IBM, fluid and structures are discretized by sperate, independent grids (Eulerian grid for fluid and Lagrangian grid for structures) which do not need to conform at the interfaces (see Fig. 2.4). This is a big advantage of IBM in solving moving and/or deformable boundary problems, as it saves the tedious remeshing process and is independent of the complexity of the boundary geometry. As the solution evolves on two separate grids, information needs to be exchanged at those interfaces through interpolation. The fluid feels the existence of the immersed object through a boundary force which is inserted into the momentum equations, and the immersed object is forced to deform and/or move so that the no-slip condition at the boundary is satisfied.

The IBM can be easily incorporated with the LBM to solve moving boundary problems. Based on the way to represent the fluid–structure interfaces, the IBM can be classified as diffused interface and sharp interface methods. In the upcoming subsections, we will give a brief introduction on them and for convenience, hereafter, we will represent Eulerian variables in lowercase, while the Lagrangian variables in uppercase.

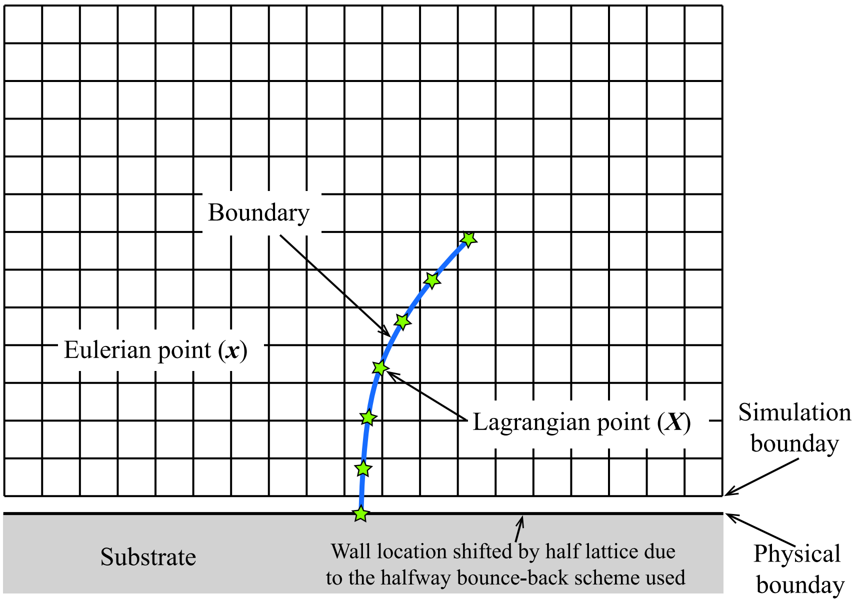

Fig. 2.4 Schematics of the grids used in our IB-LBM simulations

### 2.3.1 Diffused-interface IBM

The diffused-interface IBM is widely adopted in the study of FSI problems. In this method, the immersed boundaries are smeared due to the distribution of singular forces to the surrounding fluid using the Dirac delta function. In the original IBM developed by Peskin [41-43], the boundary forces from the solid to the fluid are calculated based on the constitutive laws (e.g. Hook's law) of the elastic boundary,

$$\boldsymbol{F}(\boldsymbol{X},t) = G(\boldsymbol{X},t) \tag{61}$$

where $G$ is the boundary force generating operator, which is related to the properties of the boundary. To incorporate the boundary effect in fluid dynamics, the boundary forces are distributed to the neighboring fluid nodes to obtain the Eulerian force density,

$$\boldsymbol{f}(\boldsymbol{x},t) = \sum_{\boldsymbol{X}} \boldsymbol{F}(\boldsymbol{X},t)\delta_h(\boldsymbol{x}-\boldsymbol{X})\Delta s \tag{62}$$

where $\delta_h$ is the Dirac delta function, $\sum_{\boldsymbol{X}}$ denotes the summations over all Lagrangian grid points, and $\Delta s$ denotes the surface area (in 2D cases, the arc length) that a Lagrangian point occupies. The no-slip boundary condition is enforced explicitly by letting the boundary points move with the local fluid velocity,

$$\frac{\partial \boldsymbol{X}(s,t)}{\partial t} = \boldsymbol{U}(s,t) = \sum_{\boldsymbol{x}} \boldsymbol{u}(\boldsymbol{x},t)\delta_h(\boldsymbol{x}-\boldsymbol{X})(\Delta x)^D \tag{63}$$

where $\Delta x$ is the Eulerian grid spacing, and $D$ is the spatial dimension of the problem, and $\sum_{\boldsymbol{x}}$ denotes the summations over all Eulerian grid points.

This version of IBM is fully explicit and can be implemented with relative ease. However, it could face stability issues when the timestep is chosen too large or the boundary is too stiff [123, 124]. To improve the numerical stability, implicit [125, 126] and semi-implicit [127-129] IBM were proposed. The original IBM by Peskin is designed to handle elastic boundaries only. For rigid boundaries with no deformation allowed, alternative way to compute the boundary forces must be constructed. There are several ways exist to do this, interested readers can refer to [130]. In the following subsections, we will give a brief introduction on three frequently used boundary-force evaluation approaches.

#### 2.3.1.1 The direct-forcing method

The explicit direct-forcing method may be the most popular boundary force evaluation scheme in IBM. In this method, the boundary force density can be easily evaluated by

$$\boldsymbol{F}(\boldsymbol{X},t) = 2\rho\frac{\boldsymbol{U}(\boldsymbol{X},t)-\boldsymbol{U}^*(\boldsymbol{X},t)}{\Delta t} \tag{64}$$

where $\boldsymbol{U}(\boldsymbol{X},t)$ is the desired velocity of the boundary which can be determined by solving the structure dynamics. $\boldsymbol{U}^*(\boldsymbol{X},t)$ is the could-be boundary velocity without considering the boundary influence on the flow, which can be interpolated from the unforced flow velocity $\boldsymbol{u}^*(\boldsymbol{x},t)$ in the LBM (i.e. $\boldsymbol{u}^*(\boldsymbol{x},t) = (\sum_i f_i \boldsymbol{e_i})/\rho$).

$$\boldsymbol{U}^*(\boldsymbol{X},t) = \sum_{\boldsymbol{x}} \boldsymbol{u}^*(\boldsymbol{x},t)\delta(\boldsymbol{x}-\boldsymbol{X})(\Delta x)^D \tag{65}$$

The explicit direct-forcing method is easy to implement and well adapted in the LBM. However, it may face unphysical streamline penetration problem [131], as the no-slip boundary condition is approximately enforced at the interface. To solve the problem, implicit direct-forcing methods have been proposed, for example in [132, 133]. The implicit schemes require to solve complicated banded matrix equations, which make the direct-forcing method less efficient and cumbersome to implement. A multi-direct forcing approach [134] is then introduced, which only requires to iterate the forcing procedures several times until the no-slip condition is well enforced. More recently, a non-iterative force correction approach for the direct-forcing method is proposed by Tao et al. [135], which is efficient and easy to implement. In this method, the boundary force computed from the explicit direct-forcing method is corrected by multiplying a local adjustment parameter $\lambda$, i.e.,

$$\boldsymbol{F}(\boldsymbol{X},t) = 2\lambda(\boldsymbol{X},t)\rho\frac{\boldsymbol{U}(\boldsymbol{X},t)-\boldsymbol{U}^*(\boldsymbol{X},t)}{\Delta t} \tag{66}$$

For an immersed boundary that represented by *Nb*+1 Lagrangian points, the corresponding $\lambda$ for the point $\boldsymbol{X}_n$, $n = 0, 1, \cdots, Nb$, can be explicitly calculated by the following equation in 3D, respectively,

$$\lambda_n = \frac{1}{\Delta s \Delta x^5 \sum_{i,j,k} \sum_m \delta\left(\boldsymbol{x}_{i,j,k} - \boldsymbol{X}_m\right) \delta\left(\boldsymbol{x}_{i,j,k} - \boldsymbol{X}_n\right)} \tag{67}$$

where $\boldsymbol{x}_{i,j,k}$ is the position of the Eulerian point. $\sum_{i,j,k}$ and $\sum_m$ represent summations over all Eulerian and Lagrangian points, respectively.

### 2.3.1.2 The momentum-exchange method

The momentum-exchange method is originally devised by Ladd [78, 79] for the LB simulation of particulate suspension. Inherited from the kinetic theory, the momentum-exchange method can evaluate the hydrodynamic force in LBM conveniently by summation over the momenta passing through the solid boundary. Although the momentum-exchange method can be directly used in LB simulations to handle FSI problems, it is a little difficult to implement and is not efficient for moving boundaries problem (it requires to identify fluid-solid links in every timestep). Niu et al. [136] combined the momentum-exchange method with the IBM, making it robust and efficient to handle both rigid and elastic boundaries. In their method, the first step is to interpolate the boundary distribution functions, as the Lagrangian points may not coincident with the background Eulerian points. It is always convenient to use the Dirac delta function for this interpolation [137],

$$f_i(\boldsymbol{X},t) = \sum_{\boldsymbol{x}} f_i(\boldsymbol{x},t)\delta\,(\boldsymbol{x}-\boldsymbol{X})\,(\Delta x)^3 \tag{68}$$

By applying the bounce-back rules, a new set of boundary distribution functions can be obtained at all lattice directions.

$$f_{-i}(\boldsymbol{X},t+\Delta t) = f_i(\boldsymbol{X},t) - 2\omega_i\rho\frac{\boldsymbol{e}_i\boldsymbol{U}(\boldsymbol{X},t)}{c_s^2} \tag{69}$$

where $-i$ denotes the opposite direction of $i$, i.e., $\boldsymbol{e}_{-i} = \boldsymbol{e}_i$. The boundary force (from the structure to the fluid) then can be computed via momentum exchange method,

$$\boldsymbol{F}(\boldsymbol{X},t) = -\sum_i \boldsymbol{e}_i \left[ f_i(\boldsymbol{X},t+\Delta t) - f_{-i}(\boldsymbol{X},t) \right] \tag{70}$$

The momentum-exchange based IB-LBM is efficient and easy to implement. However, it faces the streamline penetration problem as the direct-forcing method does. To remove this drawback, an iterative technique for the momentum-exchange based IB-LBM is introduced in [138].

#### 2.3.1.3 The feedback forcing method

The feedback forcing method that originally used by Peskin [41-43] to compute the restoring force of an elastic boundary is further developed by Goldstein et al. [139] to handle rigid boundaries. In their method, the neighboring fluid points are assumed to connect with the immersed boundary through a set of stiff springs with damping. By applying the feedback law, the boundary force is evaluated by,

$$\boldsymbol{F}(\boldsymbol{X},t) = \alpha \int_0^t \big(\boldsymbol{u}(\boldsymbol{X},t) - \boldsymbol{U}^*(\boldsymbol{X},t)\big) dt' + \beta\big(\boldsymbol{u}(\boldsymbol{X},t) - \boldsymbol{U}^*(\boldsymbol{X},t)\big) \tag{71}$$

where $\boldsymbol{u}(\boldsymbol{X},t)$ and $\boldsymbol{U}^*(\boldsymbol{X},t)$ are the interpolated and the desired velocity (obtained by solving the motion equations of the immersed boundary) at the boundary. $\alpha$ and $\beta$ are two large negative free constants to be tuned depending on the flow conditions. In the feedback forcing method, the requirement of specifying two proper parameters introduces some complexity in its practical implementations especially in unsteady flow conditions. These two parameters, if not properly chosen, may impose a restraint on the simulation timestep, and thus reduces the computational efficiency.

### 2.3.2 Sharp-interface IBM

In the diffused-interface IBMs, the fluid-structure interface is not precisely simulated at its actual location but within a localized region around the interface. The sharp-interface IBMs allows for a sharp representation of the immersed boundary, thus can obtain a higher accuracy at the interface. There are various sharp-interface IBM exist in the literature, such as [140, 141]. In the next, we will briefly introduce the direct-forcing sharp-interface IBM which can be easily incorporated with the LBM.

The very first step of a sharp-interface IBM is to do a solid-fluid demarcation. A Eulerian node outside the solid boundary is termed “fluid node”, otherwise termed “solid node”. Such node-type identification needs to be done only once for stationary boundaries. However, for moving and/or deformable boundaries, this identification is required at every timestep, thus a sharp-interface IBM is usually less efficient than a diffused-interface IBM. Once the solid-fluid demarcation has been completed, the followed step is to determine the forcing nodes (note that in a sharp-interface IBM, the immersed boundary no longer acts as a force-generator as in the diffused-interface IBM), which are inside the immersed object and have at least one neighboring fluid node (see Fig. 2.5).

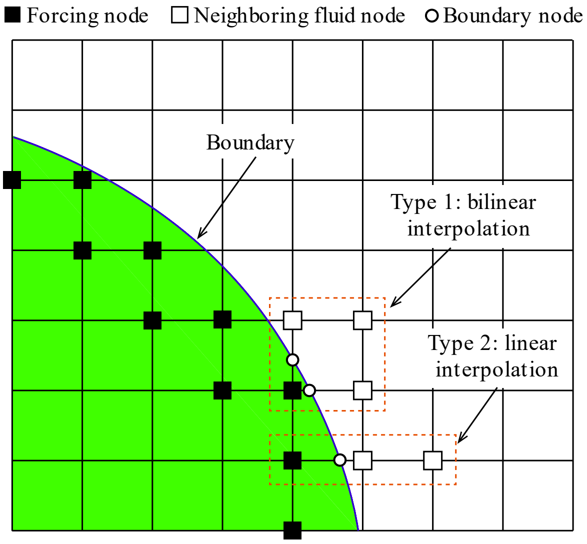

Fig. 2.5 Schematics of the forcing nodes and the interpolation schemes

In the direct-forcing sharp-interface IBM, to evaluate the boundary force density on the forcing nodes, the desired velocity at these forcing nodes needs to be interpolated so that the corresponding boundary points can satisfy the no-slip boundary condition. In 2D applications, we can use the second-order linear and bilinear interpolations from the velocities of the nearby fluid nodes and the boundary points based on the arrangement of the nearby fluid nodes [142], as shown in Fig. 2.5. For 3D applications, we can use the tri-linear interpolation if there are seven neighboring fluid nodes available for the interpolation. Otherwise, the interpolation degenerates into bilinear or linear interpolations, as explained in the 2D case. With the interpolated velocity in the forcing points, we can easily calculate the force at these points by,

$$\boldsymbol{F}(\boldsymbol{x}_f, t) = 2\rho \frac{\boldsymbol{u}'(\boldsymbol{x}_f, t) - \boldsymbol{u}^*(\boldsymbol{x}_f, t)}{\Delta t} \tag{72}$$

where $\boldsymbol{u}'(\boldsymbol{x}_f, t)$ and $\boldsymbol{u}^*(\boldsymbol{x}_f, t)$ are the interpolated and unforced velocities at the forcing node $\boldsymbol{x}_f$, respectively. $\boldsymbol{u}^*(\boldsymbol{x}_f, t)$ is calculated in the macro quantities update in the LBM without considering the forcing effect. The calculated force is then used to update the velocity at the forcing point and no force distribution step is required.

$$\boldsymbol{u}(\boldsymbol{x}_f,t)=\boldsymbol{u}^*(\boldsymbol{x}_f,t)+\frac{\Delta t}{2\rho}\boldsymbol{F}(\boldsymbol{x}_f,t) \tag{73}$$

Via this interpolated velocity, the boundary effect is considered in the LBM through the following collision and stream steps.

The sharp-interface IBMs may model the boundary with a higher accuracy. However, they could also cause spurious pressure oscillation in moving and/or deformable boundary problems [140, 143]. This undesirable feature is usually diminished in the diffused-interface IBM via the force-spreading process [144]. Spreading the force with the smoothed delta function, works as smoothing mechanism at the immersed boundaries. The sharp-interface IBMs also greatly increase the computational load and are not easy to implement. Therefore, in our study we will use the diffused-interface IBM to solve the fluid-cilium interaction.

### 2.3.3 The Dirac delta function

The Dirac delta function $\delta$ is defined as

$$\delta(\boldsymbol{x}-\boldsymbol{X})=\frac{1}{h^3}\phi\left(\frac{x-X}{h}\right)\phi\left(\frac{y-Y}{h}\right)\phi\left(\frac{z-Z}{h}\right) \tag{74}$$

where $x$, $y$, and $z$ are the components of the Eulerian point $\boldsymbol{x}$, and $X$, $Y$, and $Z$ are the components of the Lagrangian point $\boldsymbol{X}$, respectively. $h$ is a parameter defining the effective thickness of the boundary (in our case, the radius of the primary cilium) [145], and it is usually set to some multiple of the grid spacing $\Delta x$, i.e. $h=m\Delta x$, where $m$ is the grid number that the boundary thickness covers. There are a variety of stencils for function $\phi$ exist in literature. In this study, we adopted the four-point stencil which is given by

$$\emptyset(r) = \begin{cases} \left(3 - 2|r| + \sqrt{1 + 4|r| - 4r^2}\right)/8, & |r| \le 1 \\ \left(5 - 2|r| - \sqrt{-7 + 12|r| - 4r^2}\right)/8, & 1 \le |r| \le 2 \\ 0, & |r| \ge 2 \end{cases} \tag{75}$$

This stencil has a profile shown in Fig. 2.6, and it gives a second-order approximation. The way to construct $\delta$ and $\emptyset(r)$ is discussed in [43], and a comparison between different delta functions can be found in [144]. The support of $\delta$ is a $4h \times 4h \times 4h$ cube around each Lagrangian point.

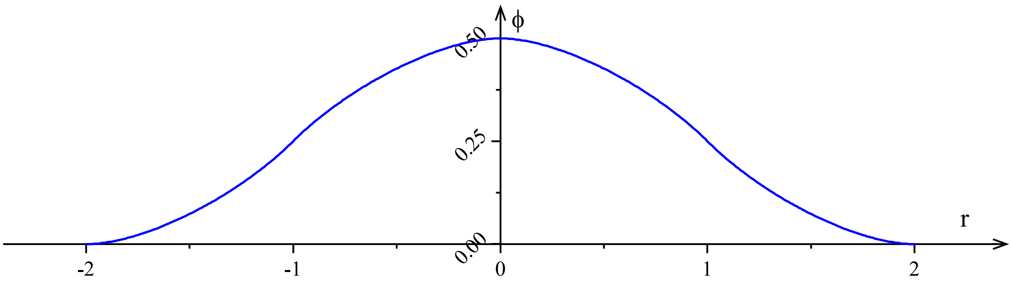

Fig. 2.6 The $\emptyset(r)$ with four-point stencil

## 2.4 Coupling strategy

There are basically two kinds of coupling strategy in the IBM for handling elastic boundaries with mass. The first one is initially used in Zhu and Peskin [48], where the boundary velocity is directly interpolated from the fluid velocity rather than determined by solving its motion equation. By doing this, the no-slip boundary condition is naturally enforced by definition. The updated boundary velocity is then taken as an input to the motion equation (Eq. (50)), to obtain the hydrodynamic force $\boldsymbol{F}_{fluid}$. In the next step, the reaction force of $\boldsymbol{F}_{fluid}$ (i.e. the boundary force) is distribute to the neighboring fluid nodes with Eq. (62).

The IBM by Huang et al. [45] and Yuan et al. [47] provided a different coupling strategy. In their approaches, the boundary force (or its reaction force, the hydrodynamic force) is evaluated first, which is then used as an input to obtain the boundary velocity by solving the motion equation (Equation (50). Finally, the boundary force is spread/distributed to the nearby fluid to make it move at the same velocity as the boundary (i.e., to enforce the no-slip condition).

In our study, we used the second coupling strategy as it can handle both rigid and elastic boundaries, thus is more robust and versatile (the original coupling strategy by Zhu and Peskin only works for elastic boundary) for solving FSI problems. The direct-forcing method is used to evaluate boundary forces due to that it’s efficient and easy to implement. To eliminate the streamline penetration problem, the no-iterative force correction technique proposed by Tao et al. [135] is adopted to well enforce the no-slip boundary condition. The coupling procedure used in our simulations is illustrated in Fig. 2.7.

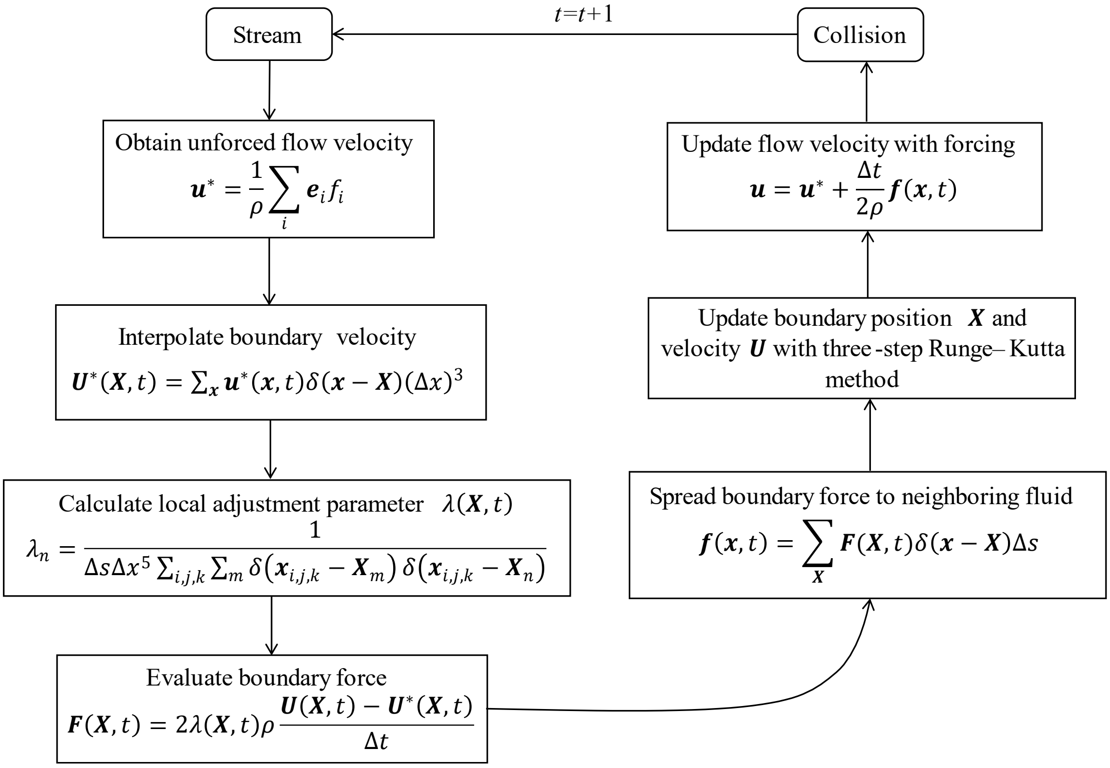

Fig. 2.7 The coupling procedure used in our simulations

## 2.5 Modelling the cilium basal end

The primary cilium is connected to the cytoskeletal microtubules of the cells through its basal body, which has a rather complex structure. Inappropriate modelling of the basal body may predict wrong or less accurate cilium dynamics. The effect of the basal body was frequently modelled with a cantilevered or clamped boundary condition at the cilium basal end. Such simplification tends to give inconsistence result with experimental measurements as the basal end can experience a certain rotation during the deflection process of cilium [28, 31]. In this study, we adopt the approach proposed by Resnick [5], to model the cilium basal body as a nonlinear rotational spring connected to the cilium basal end (see Fig. 2.8). Similar treatment has also been used by Young et al. [35] to study cilium dynamics in a shear flow and their results compared favorably with experimental observations. In this approach, a basal rotation induced by the flow drag will generate a reverse bending moment at the attached spring. This can be described in mathematics as

$$\begin{aligned} &\boldsymbol{X} = \boldsymbol{X}_0 \\ &\frac{d^2\boldsymbol{X}}{ds^2} = \frac{L}{K_b}\left(k\frac{d\boldsymbol{X}}{ds} + \alpha\left(\frac{d\boldsymbol{X}}{ds}\right)^2\right), \quad at\ s = 0 \end{aligned} \tag{76}$$

where $L$ is the length of the cilium, $k$ and $\alpha$ are the linear and nonlinear spring constants, respectively.

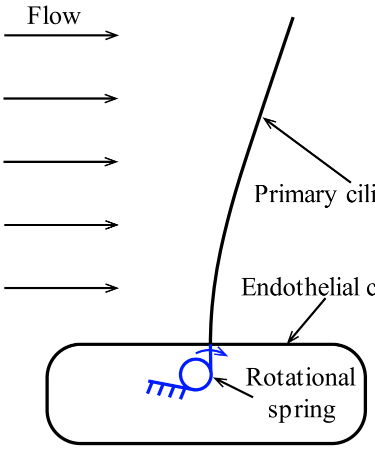

Fig. 2.8 The nonlinear rotational spring model for cilium basal end

## 2.6 Dissipative particle dynamics

To study CTC adhesion in a curved microvessel, the DPD is adopted to model the blood flow. As a kind of mesoscopic simulation methods, the DPD is frequently used in the modelling of dynamic and rheological properties of complex fluids [146, 147]. The fluid is represented by a sufficient large number of particles in the DPD. Each particle can be viewed as a molecular cluster of mass $m_i$, position $\boldsymbol{r}_i$, and velocity $\boldsymbol{v}_i$. The properties of the fluid are reflected via the interaction between particles. The interaction is achieved through the introduction of three forces, i.e. a conservative (repulsive) force $\boldsymbol{F}_{ij}^{C}$, a dissipative (friction) force $\boldsymbol{F}_{ij}^{D}$, and a random force $\boldsymbol{F}_{ij}^{R}$. The resultant force $\boldsymbol{F}_i$ for each individual particle then can be written as,

$$\boldsymbol{F}_i = \boldsymbol{F}_e + \sum_{j \neq i} \boldsymbol{F}_{ij}^{C} + \boldsymbol{F}_{ij}^{D} + \boldsymbol{F}_{ij}^{R} \tag{77}$$

where $\boldsymbol{F}_e$ denotes the external force and the sum runs over the neighbors of particle $i$ within a cutoff radius $r_c$. Each interaction force is calculated respectively as follows,

$$\boldsymbol{F}_{ij}^{C} = \begin{cases} a_{ij}(1 - r_{ij})\hat{\boldsymbol{r}}_{ij}, & for\ r_{ij} \leq r_c \\ 0, & for\ r_{ij} > r_c \end{cases}, \tag{78}$$

$$\boldsymbol{F}_{ij}^{D} = -\gamma\omega^{D}(r_{ij})(\hat{\boldsymbol{r}}_{ij} \cdot \boldsymbol{v}_{ij})\hat{\boldsymbol{r}}_{ij} \tag{79}$$

$$\boldsymbol{F}_{ij}^{R} = -\sigma\omega^{R}(r_{ij}) \cdot \frac{\xi_{ij}}{\sqrt{dt}}\hat{\boldsymbol{r}}_{ij}, \tag{80}$$

where $\hat{\boldsymbol{r}}_{ij} = \boldsymbol{r}_{ij}/r_{ij}, \boldsymbol{r}_{ij} = \boldsymbol{r}_i - \boldsymbol{r}_j, \boldsymbol{v}_{ij} = \boldsymbol{v}_i - \boldsymbol{v}_j$. $a_{ij}$, $\gamma$, and $\sigma$ are the respective coefficients. $\xi_{ij}$ is a random number with zero mean and unit variance. $\omega^{D}(r_{ij})$ and $\omega^{R}(r_{ij})$ are weight functions that rely on the distance. In order to satisfy the fluctuation-dissipation theorem in the DPD system, they have the following relationship,

$$\omega^{D}(r_{ij}) = [\omega^{R}(r_{ij})]^2 = \begin{cases} \left(1 - \frac{r_{ij}}{r_c}\right)^{1/2}, & for\ r_{ij} \leq r_c \\ 0, & for\ r_{ij} > r_c \end{cases}, \qquad \sigma^2 = 2\gamma k_B T \tag{81}$$

where $k_B$ is the Boltzmann constant and $T$ the temperature of the system. For a more detailed introduction of the DPD, interested readers can refer to [148]. The dynamics of the particles follows Newton's second law.

$$\frac{d\boldsymbol{r}_i}{dt} = \boldsymbol{v}_i, \qquad m_i\frac{d\boldsymbol{v}_i}{dt} = \boldsymbol{F}_i \tag{82}$$

where the mass for each particle $m_i$ is assumed to be unity. A modified velocity-Verlet algorithm [149, 150] is implemented to update the position and velocity of the particles at each timestep, which makes the integration more stable.

## 2.7 Cell membrane model

To well describe the deformations of the cell membrane, a spring-based network model is integrated into the DPD. In this model, the membrane is represented by a set of triangular meshes whose nodes are connected through linear springs. The elastic force generated on each membrane node *i* is calculated by

$$\boldsymbol{F}_i^{\text{membrane}} = -\frac{\partial E\{(\boldsymbol{r}_i)\}}{\partial \boldsymbol{r}_i} \tag{83}$$

where $E\{(\boldsymbol{r}_i)\}$ is the total energy of the network which the following components, i.e.,

$$E\{(\boldsymbol{r}_i)\} = E_{in-plane} + E_{bending} + E_{area} + E_{volume} \tag{84}$$

where $E_{in-plane}$ and $E_{bending}$ are the in-plane elastic energy and bending energy, respectively. $E_{area}$, and $E_{volume}$ are the energies that account for the conservation constraints of the surface area and volume.

As we adopted WLC-POW network model, this energy can be calculated by

$$E_{in-plane} = \sum_{\text{all edges}} \left( \frac{k_B T l_{max}}{4p} \frac{3x_l - 2x_l^3}{1 - x_l} + \frac{k_p}{(m-1)l^{m-1}} \right) \tag{85}$$

where $l_{max}$ denotes the maximum spring length allowed during the deformation, which is chosen as 2.2 times the equilibrium spring length based on our chosen WLC model [151]. $x_l = l/l_{max}$, where $l$ is the instantaneous spring length. $p$ is the persistence length, and $k_p$ is the spring constant in the POW model. The system temperature $T$ is chosen as 310K in our simulations. *m* is a specified exponent which takes the value of 2 in our simulations as suggested bt Fedosov et al. [151].

The bending energy $E_{bending}$ is defined as,

$$E_{bending} = \sum_{\substack{\text{all triangle} \\ \text{adjacent}}} K_b\left[1 - \cos\left(\theta_{\alpha\beta} - \theta_0\right)\right] \tag{86}$$

where $K_b$ is the bending stiffness of the cell membrane. $\theta_0$ and $\theta_{\alpha\beta}$ represent the spontaneous and instantaneous angles between two adjacent meshes.

$E_{area}$ and $E_{volume}$ are calculated respectively by,

$$E_{area} = \frac{K_{area}^{tot}(A^{tot} - A_0^{tot})}{2A_0^{tot}} + \sum_{\text{all triangles}} \frac{K_{area}(A - A_0)^2}{2A_0} \tag{87}$$

$$E_{volume} = \frac{K_{volume}(V^{tot} - V_0^{tot})^2}{2V_0^{tot}} \tag{88}$$

where $K_{area}^{tot}$, $K_{area}$, and $K_{volume}$ denotes the constraint constants for the global cell area, local element (mesh) area, and cell volume, respectively. $A^{tot}$, $A$, and $V^{tot}$ represent the instantaneous global cell area, local element area, and global cell volume, respectively, and their corresponding spontaneous values are indexed with “0”.

The cell membrane in our simulations is assumed to be incompressible and its thickness assumed to be very small thus negligible. These means the membrane surface area would remain almost constant when it gets deformed. To impose such constraint, a larger value of $K_{area}^{tot}$ is chosen so that the membrane area can be well conserved.

### 2.8 Cell adhesion model

The adhesion of the CTC to the vessel wall is modeled with the probabilistic model proposed by Hammer and Apte [152]. The adhesive dynamics in this model is mediated by the interactions between ligands and receptors coating respectively on the vessel wall and CTC (see Fig. 2.9). The formation and dissociation of the bond between the receptors and ligands obey the following rule. For a receptor, its distance $l_b$ to all free ligand (i.e., a ligand not bound to any receptors) will be calculated at each timestep. If this distance is within the reactive distance $d_{\mathrm{on}}$, a new bond could form with a probability of $P_{\mathrm{on}}$. A preexisting bond will get ruptured if the distance exceeds a disassociation distance of $d_{\mathrm{off}}$. However, if the distance is below $d_{\mathrm{off}}$, the bond may get ruptured at a probability of $P_{\mathrm{off}}$. $P_{\mathrm{on}}$ and $P_{\mathrm{off}}$ are defined as

$$P_{\mathrm{on}} = \begin{cases} 1 - e^{-k_{\mathrm{on}}\Delta t}, & l_b < d_{\mathrm{on}} \\ 0, & l_b \geq d_{\mathrm{on}} \end{cases} \tag{89}$$

$$P_{\mathrm{off}} = \begin{cases} 1 - e^{-k_{\mathrm{off}}\Delta t}, & l_b < d_{\mathrm{off}} \\ 1, & l_b \geq d_{\mathrm{off}} \end{cases} \tag{90}$$

where $\Delta t$ is the time step interval, $k_{\mathrm{on}}$ and $k_{\mathrm{off}}$ are the association and dissociation rates which are calculated by,

$$k_{\mathrm{on}} = k_{\mathrm{on}}^0 \exp\left(-\frac{\sigma_{\mathrm{on}}(l_b - l_b^0)^2}{2k_B T}\right) \tag{91}$$

$$k_{\mathrm{off}} = k_{\mathrm{off}}^0 exp\left(\frac{\sigma_{\mathrm{off}}(l_b - l_b^0)^2}{2k_B T}\right) \tag{92}$$

where $k_{\mathrm{on}}^0$ and $k_{\mathrm{off}}^0$ are the unstressed reaction rates which are obtained when the distance $l_b$ equals to the equilibrium spring length $l_b^0$. $\sigma_{\mathrm{on}}$ and $\sigma_{\mathrm{off}}$ are effective on and off strengths. For each bond, there exist a spring force $F_s$ along the receptor and ligand link to make the receptor adhere to the vessel wall.

$$F_s(l_b) = K_s(l_b - l_b^0) \tag{93}$$

A stochastic Monte Carlo technique is used in this study to determine the state of the bond. For each ligand-receptor pair that is under the effective distance $d_{\mathrm{on}}$, and existing bond under the effective distance $d_{\mathrm{off}}$, two uniformly distributed random number $\xi_1$ and $\xi_2 \in [0, 1]$ will be generated. A new bond will form if $P_{\mathrm{on}} > \xi_1$, and an existing bond will rupture if $P_{\mathrm{off}} > \xi_2$.

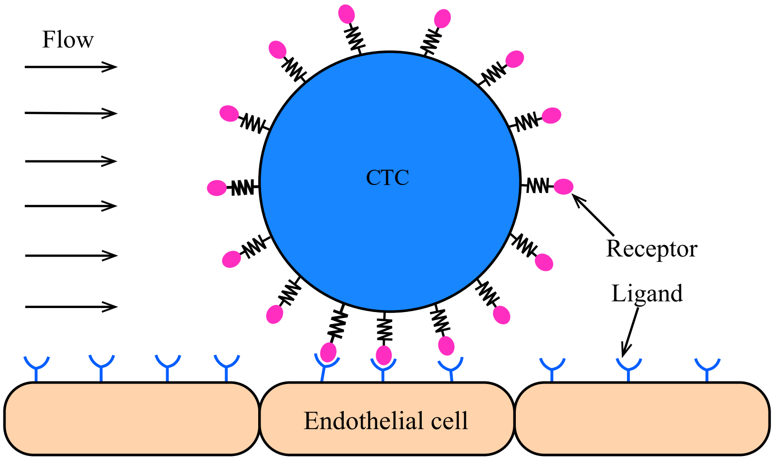

Fig. 2.9 Schematic diagram of the adhesion model

# Chapter 3 Validations and grid independence study

## 3.1 Planar Poiseuille flow

A 3D planar Poiseuille flow is simulated to validate our LBM code. The planar Poiseuille flow has the following analytical solution.

$$U(z) = \frac{\Delta P}{2L\rho\upsilon}(Hz - z^2) \tag{94}$$

where $H$ is the distance between the two infinite plates which are parallel to the z-direction and $L$ is the length of the computational domain in the flow direction. $\rho$ is the density and $\upsilon$ the kinetic viscosity of the fluid. $\Delta P/L$ is the applied pressure gradient.

In our simulation, a periodic boundary conditions are assumed in the x- and y-directions. Instead of imposing pressure boundary conditions at the inlet and outlet, the pressure gradient is generated by applying a body force density $f_d$ at each fluid node. This is a widely used trick in the LBM community to simulate pressure-gradient driven Poiseuille flow, as in [38, 153]. The applied body force density is equivalent to a pressure gradient under the relation of

$$\frac{\Delta P}{L} = f_d \tag{95}$$

The simulation domain is a cuboid, and the grid resolution is $30 \times 30 \times 150$. The simulation parameters are chosen that the result will give a maximal *U*-velocity of 0.009 at *Re*=10. Periodic boundary conditions are imposed in the x- and y- directions and a half-way bounce-back scheme is applied at the plates to enforce the no-slip wall boundary condition. When the simulation converges, the simulated result was compared with the analytical solution and a favorable agreement was obtained, as shown in Fig. 3.1.

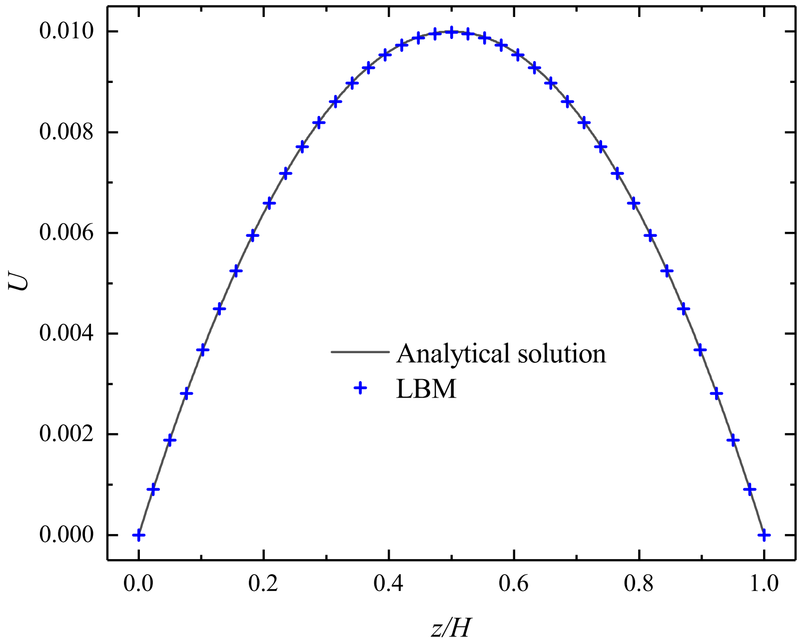

Fig. 3.1 Comparison of the LBM simulation result and the analytical solution

## 3.2 A flexible rope pendulum swings under gravity

The structure solver is validated by simulating the swinging motion of a flexible rope pendulum under gravity with the absence of ambient fluid. The schematic diagram is illustrated in Fig. 3.2a. A flexible pendulum is pivoted and initially hanging sideways (with an initial angle of θ) from the vertical direction where gravity **g** applies. Both the length $L$ and linear density $\rho_f$ of the pendulum are set to unity, and the magnitude of the gravity $|\mathbf{g}|$ is 10. The dynamics of the pendulum is governed by Equation (50) with the hydrodynamic and repulsive forces being replaced by a gravity. The equation is solved with a finite-difference method described in Section 2.2. A typical cycle obtained is demonstrated in Fig. 3.2b, where asymmetry in the swinging motion can be observed which is likely due to the flexibility of the pendulum. When $\theta$ is very small, an analytical solution for the tip displacement can be derived using a perturbation method [45], given that $\theta$ is very small and a hinged and a free-end boundary condition applied at the two ends of the pendulum. The analytical solution is given as following,

$$x(s,t) = \sum_{i=1}^{\infty} \frac{4\theta L}{z_i^2} \frac{J_2(z_i)}{J_1^2(z_i)} J_0\left(z_i \sqrt{\frac{L-s}{L}}\right) \cos\left(\frac{z_i}{2}\sqrt{\frac{|\mathbf{g}|}{L}}\right) \tag{96}$$

where $J_0$, $J_1$and$J_2$ are the Bessel function of the first kind of order zero, one and two, respectively. $z_i$ is the $ith$ positive root of $J_0(z)$.

For a totally flexible pendulum with a zero bending rigidity and a small initial angle ($\theta$=0.01), the comparison of the simulated and analytically calculated tip x-displacement at successive time is shown in Fig. 3.2c. We can see the results match closely.

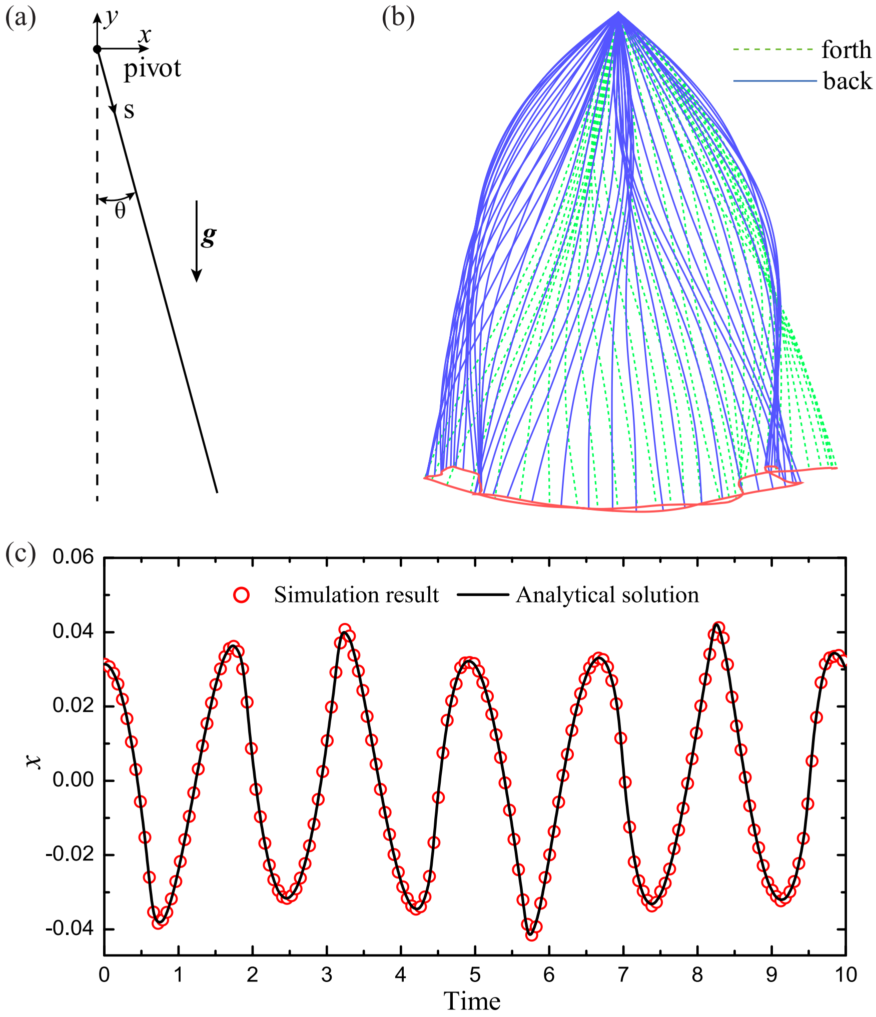

Fig. 3.2 The schematic diagram of the swinging pendulum problem (a) simulated superposition of the pendulum in one cycle ($K_b = 1 \times 10^{-3}, \theta = 0.15\pi$) (b) comparison of the tip $x$-displacement between numerical and analytical solutions ($K_b = 0, \theta = 0.01$) (c)

## 3.3 An oscillating sphere in a quiescent fluid

The flow solver and the immersed boundary method are validated by simulating an oscillating sphere in a quiescent fluid, which is a typical moving boundary problem that has been studied by Mei [154] and Tian et al. [155]. The sphere with a radius $R$ is initially placed at the center of a cuboid domain which has the size of $40R \times 36R \times$

$36R$, as shown in Fig. 3.3a. The sphere is represented by 4000 uniformly distributed Lagrangian points using the method of Saff and Kuijlaars [156]. The oscillation speed of the sphere is $U = U_m \cos(\omega t)$, where $U_m$ is the amplitude of the velocity and $\omega$ is the angular frequency of the oscillation. The problem is governed by two dimensionless number, i.e. the Reynolds number $Re = 2U_m R/\upsilon$, and the Stokes number $\varepsilon = \sqrt{\omega R^2/2\upsilon}$. A uniform grid is used to solve the problem with the resolution that each $R$ covers 20 grid points, and to improve computational efficiency, our algorithm is parallelized. To compare with the literature, the $Re$ and $\varepsilon$ are chosen as 40 and 4, respectively. The unsteady drag force is evaluated using the scheme proposed by Suzuki and Inamuro [157],

$$F_D = \frac{\partial}{\partial t}\int_{V_s} \rho u dV - \int_{V_s \cup V_f} f_x dV \tag{97}$$

where $V_s$ and $V_f$ denote the solid and fluid domains, respectively. $f_x$ is the *x*-component of the boundary force that exerted on the fluid points. After the flow becomes periodic, we compare the dimensionless drag force, defined by $C_D = F_D/6\pi\rho\upsilon U_m R$, with that of Mei [154] and Tian et al. [155]. The comparison is shown in Fig. 3.3b, where a good agreement is obtained, and Fig. 3.3c and Fig. 3.3d shows the instantaneous velocity and vorticity fields respectively at 0.6T.

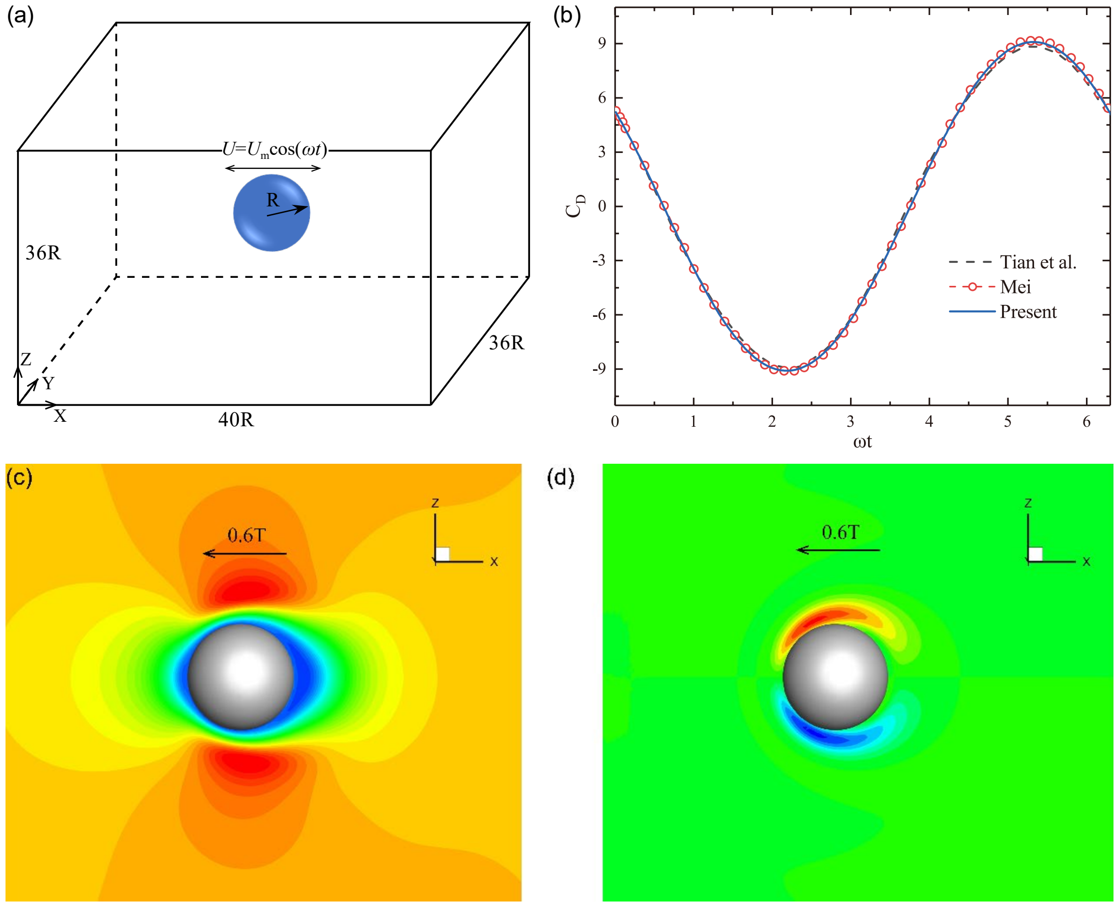

Fig. 3.3 The schematic of the oscillating sphere problem (a) and comparison of the dimensionless drag force (b) the velocity (c) and vorticity (d) contours at t=0.6T

## 3.4 Grid independence study

The solution accuracy gets improved when more grid is used in the simulations. However, this will inevitably bring a heaver computational load as the required run time and memory surge in 3D cases. We therefore need to find a proper balance between the simulation accuracy and the computational cost. To that purpose, we performed a grid independence study to figure out the maximal effective grid spacing for the simulation problem (i.e., prove that the chosen grid spacing is sufficiently small).

In this section, we performed the grid independence study by simulating the deflection of a primary cilium in a steady flow. The flow $Re$ based on the maximal upstream velocity and the channel height is 0.02. The cilium is anchored at the center of the bottom wall which is formed by endothelial cells, and the cilium initially orients perpendicularly to the bottom wall as shown in Fig. 3.4a. The domain is assumed periodic in the x- and y- directions to represent a bed of cilia. While in the z-direction, a no-slip boundary is imposed to the bottom plane and a symmetry boundary condition is applied to the top plane as we also assumed that the primary cilia present symmetrically in both the upper and bottom walls. For the cilium tip, a free-end boundary condition is applied.

$$\frac{\partial^2 \boldsymbol{X}}{\partial s^2} = 0, \ \frac{\partial^3 \boldsymbol{X}}{\partial s^3} = 0 \tag{98}$$

At the basal end of the cilium, it is attached to a nonlinear rotational spring as depicted in Fig. 1, thus boundary condition can be written as,

$$\boldsymbol{X} = \boldsymbol{X}_0, \ \frac{d^2\boldsymbol{X}}{ds^2} - \frac{L}{K_b}\left(k\frac{d\boldsymbol{X}}{ds} + \alpha\left(\frac{d\boldsymbol{X}}{ds}\right)^2\right) = 0, \ \text{for } s=0 \tag{99}$$

where $L$ is the length of the cilium, $k$ and $\alpha$ are the linear and nonlinear spring constants, respectively.

In the IBM, the Lagrangian points should be distributed neither too sparsely nor too densely. In a too sparse distribution, the fluid will leak between those Lagrangian points. When the distribution is too dense, two neighboring points may never get separated [158]. It is thus usually recommended to choose the Lagrangian grid spacing $\Delta s$ somewhere between 0.5-1 times the Eulerian grid spacing $\Delta x$ [93]. In our simulations, to save the computational cost, $\Delta s$ is set equal to the $\Delta x$.

In each simulation, the grid spacing $\Delta x$ is refined by a factor of 1.5, and to inhibit the compressibility error in the LBM, the time step Δt is scaled accordingly to ensure that $\Delta t/\Delta x$ is kept unchanged. Moreover, as mentioned above, the parameter $h$ in the Dirac delta function has a physical meaning. To keep the cilium radius a constant during the grid refinement process, the value of $h$ is also varied accordingly to make the function's supporting distance remain unchanged. The time evolution of the deflection of the cilium tip $\delta$ at different grid spacing is shown in Fig. 3.4b. We can conclude that the solution is found grid independent at $\Delta x$=1/60, as little difference can be observed when the grid spacing further gets refined to $\Delta x$=1/90.

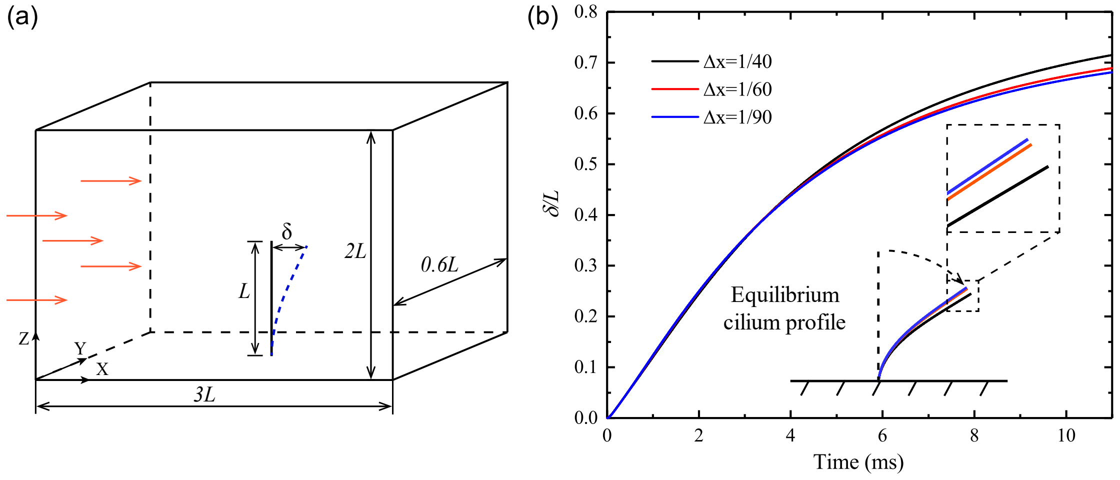

Fig. 3.4 The schematic of a primary cilium deflected in a steady flow (a) and the time evolution of the deflection of the cilium tip $\delta$ at different grid spacing with the inset showing the equilibrium cilium profile (b)

# Chapter 4 The dynamics of an array of primary cilia in an oscillating Newtonian fluid flow

## 4.1 Model formation and simulation setup

In this chapter, we simulated the dynamics of primary cilia in an oscillating Newtonian fluid flow. We first consider the scenario that primary cilia periodically and symmetrically present at the bottom and upper plates, which can be viewed as two infinite cilia arrays, and more importantly, all the primary cilia are assumed to move synchronously. This allows us to solve only one motion equation for the primary cilia with periodic and symmetry boundary conditions, as shown in Fig. 4.1. The primary cilium in our simulations is anchored at the center of the bottom plate (wall) of the simulation box. The two plates in Fig. 4.1 are only a rough approximation of the support substrate (such as the inner wall of blood vessels and the collecting duct in renal tubules) for primary cilia. Here we do not take the geometry curvature into consideration and the plates/walls are assumed to be rigid and impermeable. The flow is assumed to be incompressible, laminar, Newtonian, and oscillatory, and it can be characterized by two dimensionless numbers, i.e., the peak Reynolds number $Re_{peak}$ and the Womersley number $Wo$. As we simulated only half of the domain by using a symmetry boundary condition, these two numbers are defined as,

$$Re_{peak} = \frac{u_0 D}{\upsilon}, \qquad Wo = D\sqrt{\frac{2\pi f}{\upsilon}} \tag{100}$$

where $D$ is the distance between the upper and bottom plates where primary cilia anchor at. $u_0$ is the maximal flow speed when the oscillating frequency $f = 0$, i.e. there is no oscillation. We also introduce the following non-dimensionalization

$$L^* = \frac{L}{D}, \qquad L_d^* = \frac{L_d}{L}, \qquad W_d^* = \frac{W_d}{L} \tag{101}$$

where the quantities with asterisk denote their non-dimensional counterparts.

The pulsatile flow is driven by a temporally oscillating pressure gradient which has a sinusoidal waveform.

$$\frac{dp}{dx} = A\sin(2\pi f t) \tag{102}$$

where $A$ is amplitude of the waveform, which is determined by $A = 8\rho u_0 v/D^2$.

As we are focusing on the dynamics of primary cilia in relatively small vessels, the physiological-relevant $Re_{peak}$ and $Wo$ chosen here are relatively small, which indicate that the viscous effects dominate over the inertial and pulsatile effects in the flow. The basic parameters of this fluid-cilium coupling system are tabulated in Table 4.1.

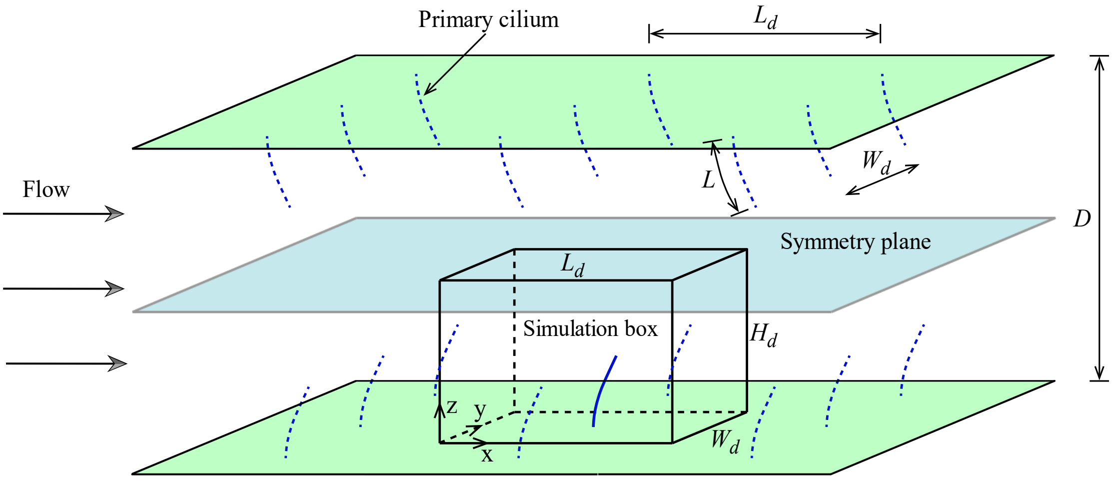

Fig. 4.1 The schematics of the considered problem

Table 4.1 Basic parameters of the fluid-cilium coupling system in physical units

| **Parameter** | **Symbol** | **Physical value** |
|---|---|---|

| | | |
|---|---|---|
| Distance between the two plates | $D$ | 24μm |
| Cilium length | $L$ | 4, 6, 8μm |
| Cilium diameter | $d$ | 0.2μm [21] |
| The height of the computational domain | $H_d = \frac{1}{2}D$ | 12μm |
| Cilium spacing interval in x-direction (i.e. the length of the computational domain) | $L_d$ | 3, 6, 12, 18μm |
| Cilium spacing interval in y-direction (i.e. the width of the computational domain) | $W_d$ | 4.8μm |
| Fluid density | $\rho_f$ | $1000\mathrm{kg/m^3}$ |
| Cilium density | $\rho_c$ | $1110\mathrm{kg/m^3}$ [159] |
| Cilium linear density | $\rho_l = \rho_c \frac{\pi d^2}{4}$ | $8.72 \times 10^{-12}\mathrm{kg/m}$ |
| Fluid kinematic viscosity | $\upsilon$ | $1.2 \times 10^{-6}\mathrm{m^2/s}$ |
| Bending rigidity of cilium | $K_b$ | $1.5 \times 10^{-23}\mathrm{Nm^2}$ |
| Linear spring constant | $k$ | $4.6\times 10^{-12}\mathrm{N/rad}$ [5] |
| Nonlinear spring constant | $\alpha$ | $-1 \times 10^{-10}\mathrm{N/rad^2}$ [5] |
| Peak Reynolds number | $Re_{peak}$ | 0.05-0.3 |
| Womersley number | $Wo$ | 0.4-1.5 |

For the boundary conditions, the periodic boundary condition described in Section 2.1.3.1 is applied to the x- and y- directions. A symmetry boundary condition is imposed to the upper plate while the bottom plate is assumed to be no-slip which is implemented with the half-way bounce-back scheme described in Section 2.1.3.2. For the primary cilium, a free-end boundary condition is imposed at its distal end (i.e., cilium tip), which means that the bending moment and transverse stress vanish at this end. In mathematics, this would require that,

$$\frac{d^2\boldsymbol{X}}{ds^2}=\frac{d^3\boldsymbol{X}}{ds^3}=0,\ \ at\ s=L \tag{103}$$

The basal end of the cilium is applied with a torque due to the deformation of the attached rotational spring, in that case the boundary condition becomes [5]

$$\begin{gathered}\boldsymbol{X}=\boldsymbol{X}_0\\ \frac{d^2\boldsymbol{X}}{ds^2}=\frac{L}{K_b}\left(k\frac{d\boldsymbol{X}}{ds}+\alpha\left(\frac{d\boldsymbol{X}}{ds}\right)^2\right),\ \ at\ s=0\end{gathered} \tag{104}$$

where $L$ is the length of the cilium, $k$ and $\alpha$ are the linear and nonlinear spring constants, respectively.

### 4.2 A baseline case

We first look at how these synchronized primary cilia get deflected and examine their impact on the flow pattern. Without losing generality, a baseline case with $Re_{peak}$ and $Wo$ at 0.2 and 0.6, respectively, is chosen and studied. The length ratio $L^*$ is 1/4 and the cilium spacing intervals in $x$- and $y$-directions are ${L_d}^*=2.0$ and ${W_d}^*=0.8$, respectively. The simulated cilium initially orients perpendicularly to the bottom wall and is unstressed. An oscillating flow comes and deflects the cilium, making it flaps left and right. After several oscillating cycles, the cilium's flapping motion becomes periodic, and then we start to record data for analysis.

The cilium profile in a typical flapping cycle is shown in Fig. 4.2, where the flapping motion is decomposed into a forward stroke and a backward stroke. Here a forward stroke denotes a clockwise deflection process while a backward stroke refers to a counterclockwise deflection process. We can see that the flapping is two-dimensional and totally symmetrical in term of the cilium profile, which means that the forward and backward stokes are proceeded in the same fashion but in opposite directions. No straight cilium profile can be observed during the entire flapping cycle, indicating that the cilium is tressed all the time during this process. It is also noticed that no out-of-plane cilium motion is observable for such cilia arrangement. In each stroke, the middle section of the cilium seems to lead the rest section in the flapping, while there is an obvious lag at the cilium's tip section. The flapping dynamics of primary cilium we observed is similar with the ciliary oscillation captured in renal tubular flow by O'Connor et al. [160]. Therefore, it is very likely that the flow in the renal tubular is oscillatory rather than unidirectional.

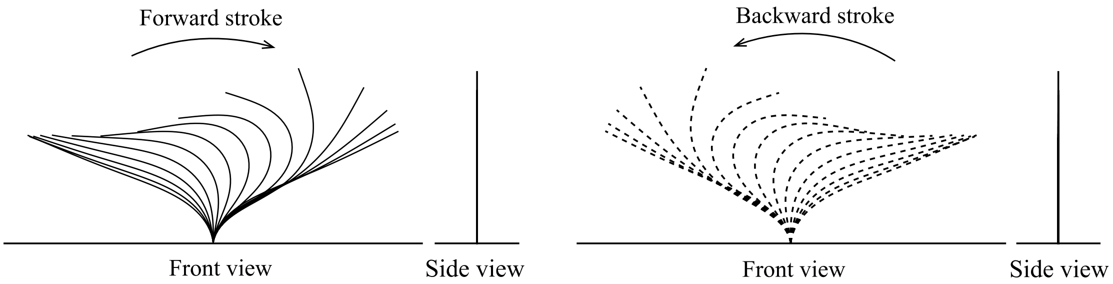

Fig. 4.2 The forward and backward strokes in a flapping cycle

When the cilium gets deflected, one side of its membrane will be stretched while the other side will be compressed at the same location. For the chosen case, two typical stretch states are observed during the deflection process, as shown in Fig. 4.3. In the first stretch state, the cilium is distorted in one direction, and the direction of the profile curvature (i.e., its principal normal) does not vary along the cilium length. This makes one side of the membrane under stretch while the other under compression throughout the cilium length. In the second stretch state, the direction of the profile curvature is found to vary once along the cilium length. As a result, each side of the cilium membrane will be partially under stretch and partially under compression due to the simultaneously exist of two curvature directions in the profile.

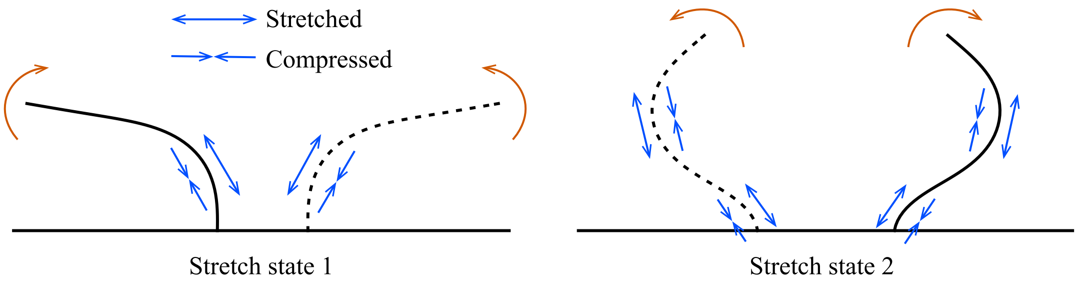

Fig. 4.3 The observed two stretch states during the deflection process

The time evolution of the cilium height (scaled by the cilium length) is shown in Fig. 4.4a. The cilium is observed to lie low and never reach its initial height $L$ (the maximal and average heights are $0.79L$ and $0.55L$, respectively) in a flapping cycle, which is endowed by its low bending rigidity. By adopting a more streamlined profile during the deflection, the primary cilium can decrease the hydrodynamic resistance and at the same time alleviate its disturbance to the fluid flow, making itself less intrusive as a flow sensor. The time evolution of the basal rotation angle is presented in Fig. 4.4b, where the basal rotation angle of the cilium is observed to vary between $-14.2^{\circ}$ and $14.2^{\circ}$. The evolution curve of the angle is also found to be distinct from the applied pressure gradient waveform and there is a rapid decrease after the value reaches its peaks and valleys.

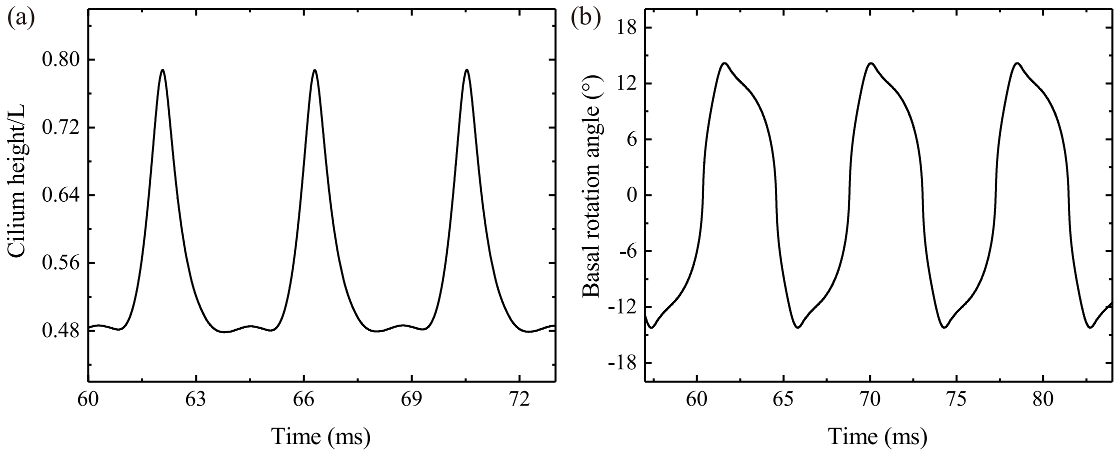

Fig. 4.4 The time evolution of the scaled cilium height (a) and basal rotation angle (b)

The time evolutions of the scaled tip deflection and tip angular speed (TAS) are shown in Fig. 4.5a, and b, respectively, where the normalized pressure gradient waveform is appended for reference. Compared with the applied pressure gradient (input signal), a phase lag (more than 1/4 oscillating cycle) in the tip defection curve can be observed in Fig. 4.5a, which is consistent with the two-dimensional result of O'Connor et al [38]. The phase lag is due to the low but nonnegligible bending rigidity of the primary cilium, which resists the deformation caused by the flow drag. Interestingly, unlike the tip deflection, a very limited phase lag is observable in the TAS (see Fig. 4.5b), suggesting that the TAS and the pressure gradient signal can be better synchronized during the deflection/sensing process. Therefore, the TAS is better in identifying the variations of pressure gradient signal due to its fast response speed which will cause little delay. We also noticed that the peak and valley values of the TAS are obtained when the cilium's deflection is around zero (i.e., when the cilium tip swings over its basal end).

As it has been experimentally verified that the opening of the ion channels in the cilium membrane is correlated with the local tensile stress [8, 9]. The tensile stress of a primary cilium is approximately proportional to its curvature due to its large aspect ratio. Therefore, the term “maximal curvature” and the “maximal tensile stress (MTS)” in this study can be used synonymously. As a result, the stretch-sensitive ion channels localized at membrane area with larger curvature would be prioritized and more likely to get activated during the deflection process. The location of the MTS (scaled by the cilium length) as a function of time is plotted in Fig. 4.5c. The previous numerical studies by Rydholm et al. [37] and Young et al. [35] on cilium deflection in a steady flow predicted an MTS location at the cilium base region. However, when it comes to an oscillating flow, we observe that the MTS location may not always stay at the base region, instead it is found to periodically varies (relocated) during the deflection process (see Fig. 4.5c). To be more specific, starting from the base point (where the MTS location is found at for roughly half of a flapping cycle), the MTS location is found to propagate forward to the cilium tip by a certain distance. With the chosen simulation parameters, the propagation distance can be as far as $0.56L$. Beyond this observation, the relocation of MTS is found to typically happen in the first halves of the forward and backward stokes, where the value of TAS is increasing.

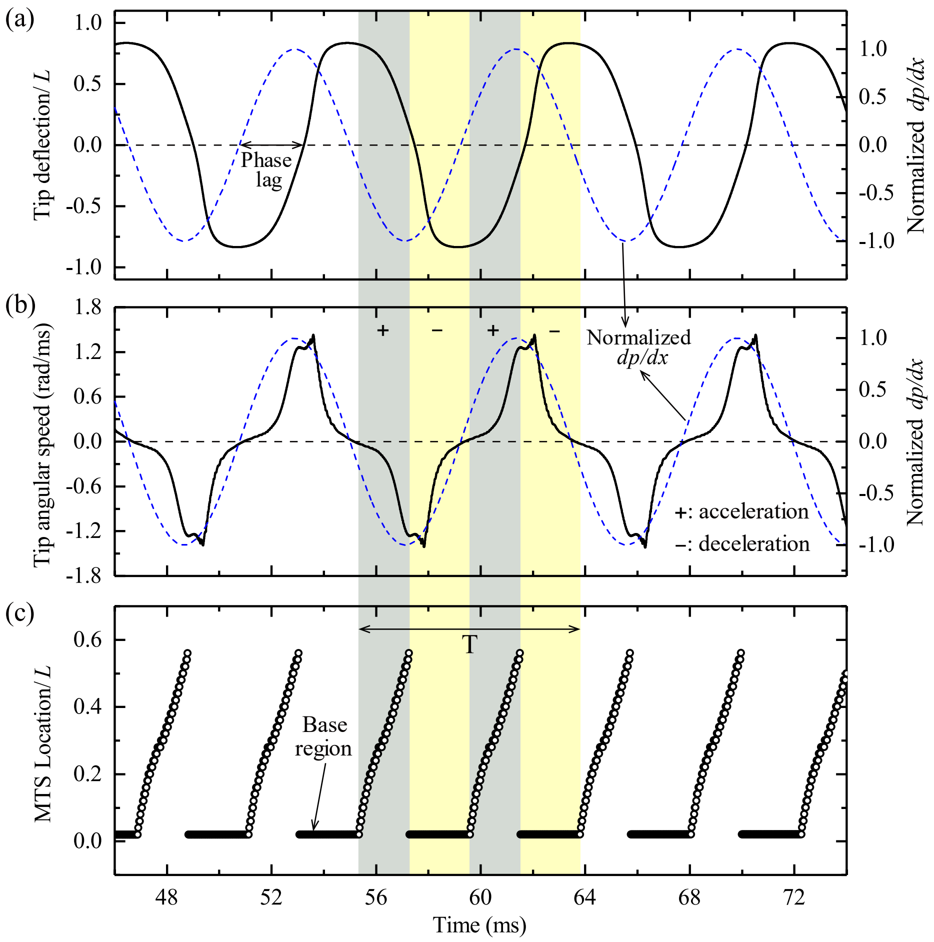

Fig. 4.5 Time evolutions of the scaled tip deflection (a), tip angular speed (b), and scaled MTS location (c)

To investigate the local curvature distribution along the cilium length during the deflection, three equally spaced sites on the cilium are selected (see Fig. 4.6a), which represent the lower, middle, and upper parts of the cilium, respectively. Fig. 4.6b shows the time evolutions of the curvature at these sites. A significantly lower maximal curvature can be found at Site A. Site C has the largest maximal curvature among these three sites, though its average curvature is lower than that of Site B. Despite its low value, the curvature at Site A is found to be almost in synchronization with the applied pressure gradient, while an obvious phase difference exists for the other two sites. A smaller phase difference means a fast respond speed and less delay. Therefore, it would be reasonable to speculate that the lower part of primary cilia may be most responsible for detecting the variations of those flow information.

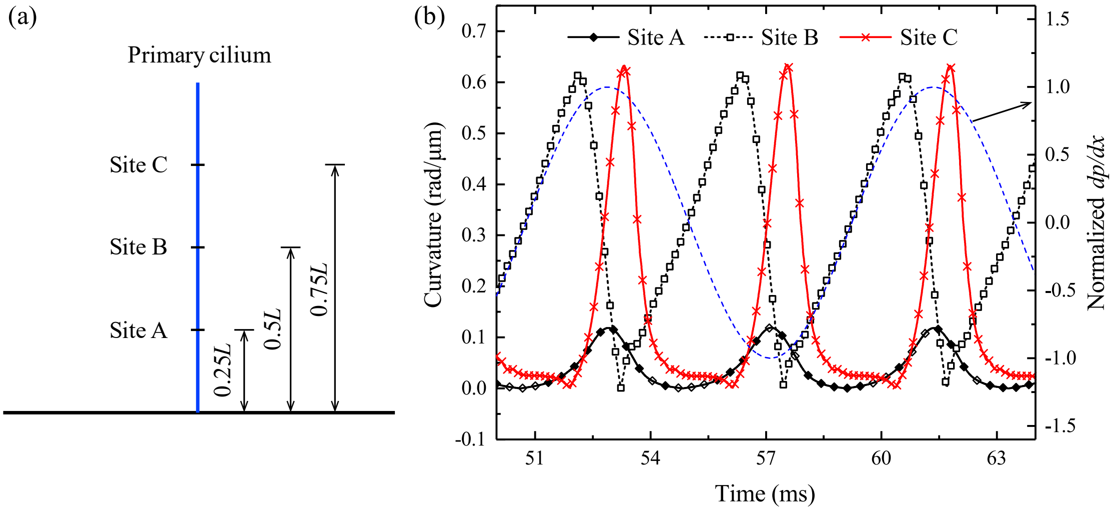

Fig. 4.6 Location of the three sites (a) and time evolutions of the curvature at the three sites (b)

The flow pattern in the deflection plane during a flapping cycle is given in Fig. 4.7, where the fluid motion is captured by streamlines. T1-T5 are some typical moments picked from a forward stroke while T6-T10 are chosen from the subsequent backward stroke. The flow features in T6-T10 are almost identical to those in T1-T5, only in the opposite direction. Due to the presence of primary cilium, the flow is disturbed especially in the near-wall region. However, unlike the moderate-Re cases that reported in [38], no interspersed recirculation regions are observable between the cilium spacing in our low-Re case. When the cilium approaches to its deflection limit, the disturbance becomes even stronger and a recirculation zone is formed around the cilium.

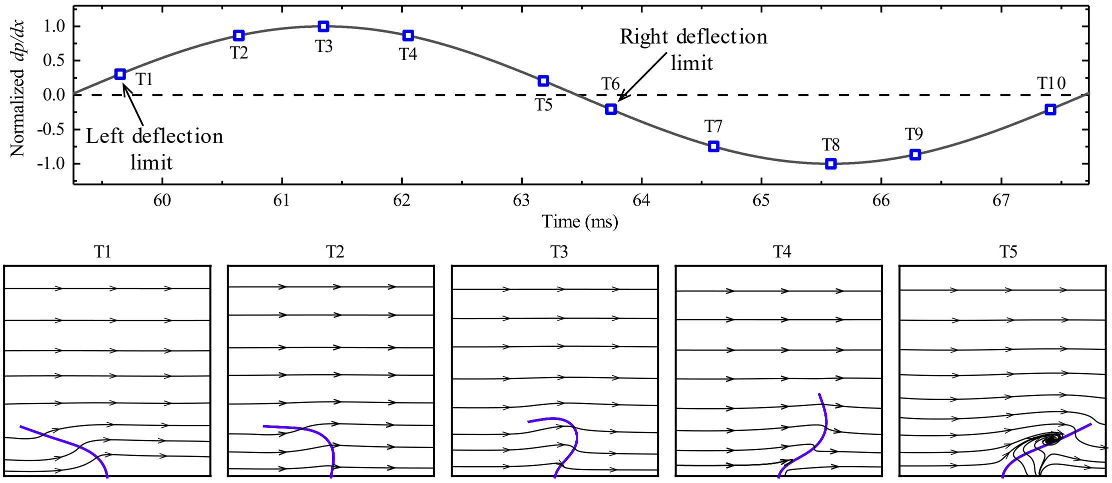

(a) Forward stroke

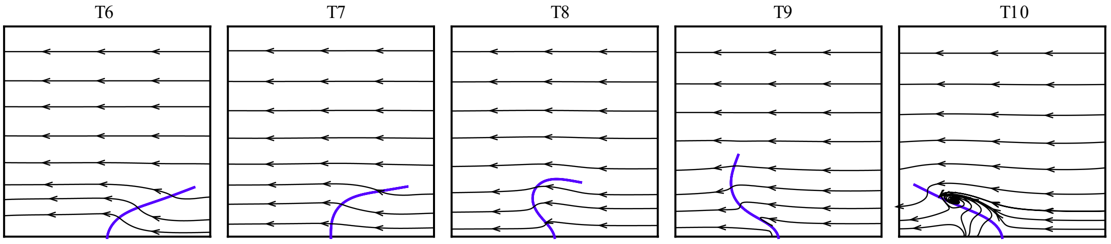

(b) Backward stroke

Fig. 4.7 The flow pattern in the deflection plane during a flapping cycle

Fig. 4.8a and b show the evolutions of the recirculation zone and the corresponding u-velocity contour during T5-T6. It is observed that, the recirculation zone initially forms around the lower section of the primary cilium with a very limited size. However, as time progresses, the zone gradually gets expanded and will eventually span the entire length of the cilium as the cilium deflects more to its deflection limit. During this process, the center of the recirculation zone is observed to move from the cilium's lower section to its tip section (see Fig. 4.8a). The presence of the primary cilium decelerates the fluid motion near the cilium surface due to the viscous effects (known as the no-slip condition). As a result, the adjacent fluid seems to stick to the cilium surface, as can be seen from Fig. 4.8b. During the deflection process, it is noticed that each node of the cilium does not reach its deflection limit (i.e., zero velocity moment) synchronously, and as mentioned earlier, the lower section synchronized better with the applied pressure signal. Therefore, the cilium's section closer to the basal end tends to reach its deflection limit more quickly. The lower section could already start its reversal motion when the tip section is about to reach its deflection limit. This brings opposite movements at different sections of the cilium. Due to the no-slip condition, two opposite fluid motions are generated, which further creates a recirculation zone (see Fig. 4.9a) at the lower section. The zone goes up as the reversal motion propagates towards the cilium tip. The 3D vortical structure (identified using the Q criterion [161]) at T5 is shown in Fig. 4.9b, where the tooth-like vortex is mainly found at the cilium tip section, but is not strong enough to shed from the cilium surface.

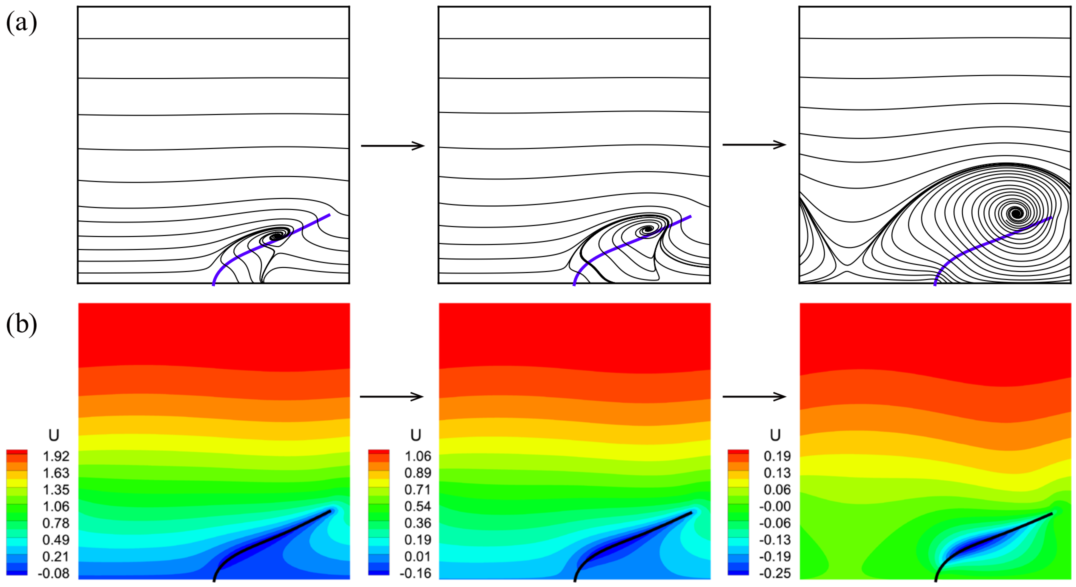

Fig. 4.8 The evolution of the recirculation zone (a) and the u-velocity field (b) during T5 to T6

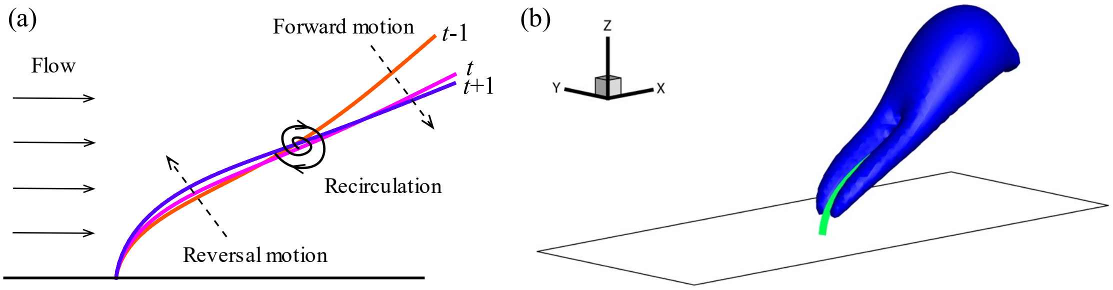

Fig. 4.9 A schematics of the formation of the recirculation zone (a) 3D vortical structure at T5 with the iso-surface of $Q = 4 \times 10^{-10}$ (b)

The flow-induced wall shear stress (WSS) is a kind of stimulus that endothelial cells forming the vessel wall are particularly sensitive to. Both low and oscillatory WSS have been implicated as potential causes for cardiovascular diseases such as atherosclerosis [162]. To examine the influence of primary cilia on the WSS distribution (hereafter the WSS in this study refers to the magnitude of the WSS vector unless otherwise stated), the WSS contour at the bottom plate is evaluated and shown in Fig. 4.10. As the variation of the WSS is also symmetric in a flapping cycle, only the WSS distribution in a forward stroke is presented. A uniform WSS distribution can be expected when the cilium is absent in the flow field. However, in the case when primary cilia are presented, the WSS distribution no longer remains uniform but varies in space. The region around the site where the primary cilium anchors tend to have a lower WSS. The presence of cilium also has a larger impact on the downstream WSS distribution compared with that in the upstream. When the flow becomes stronger (i.e., the velocity field increases in magnitude), the cilium's impact also gets strengthened as the affected area is extended along the flow direction. The time evolutions of the average WSS in cases with and without cilia are shown in Fig. 4.11. We can see that the presence of cilia reduces the average WSS.

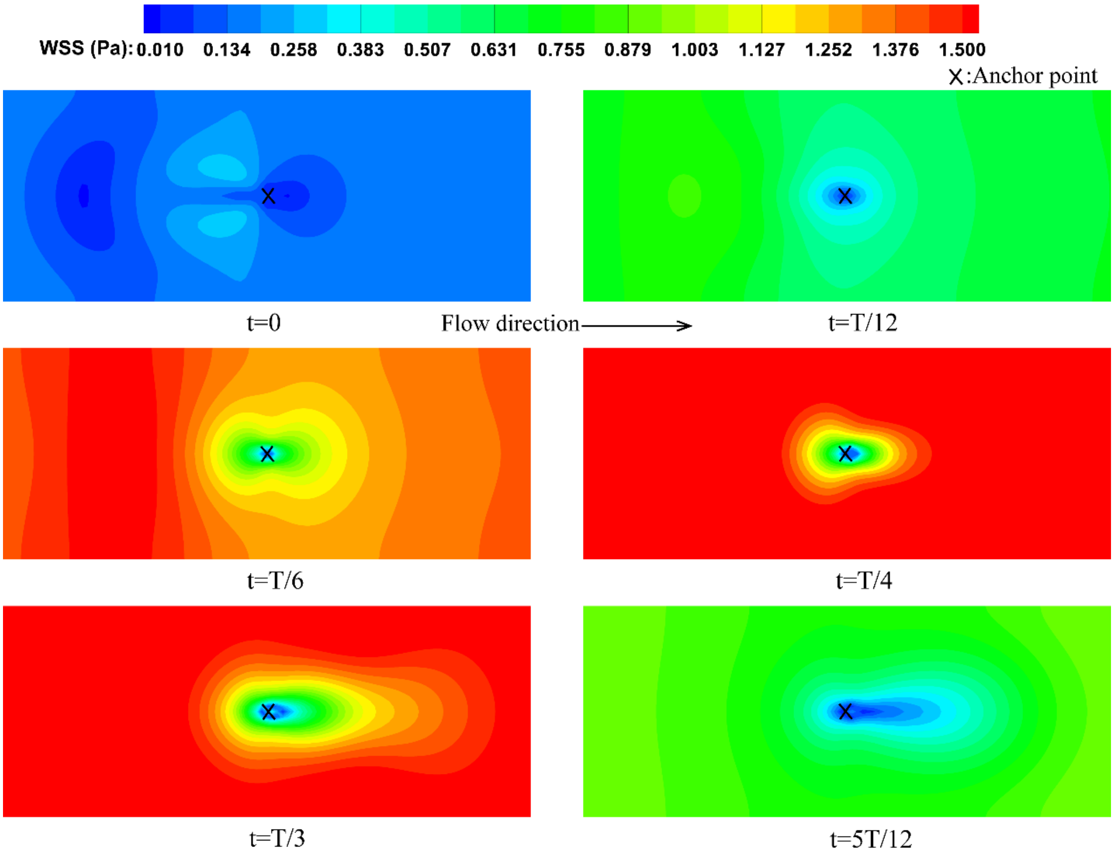

t=0 t=T/12

t=T/6 t=T/4

t=T/3 t=5T/12

Fig. 4.10 The snapshots of the WSS distribution in a forward stroke

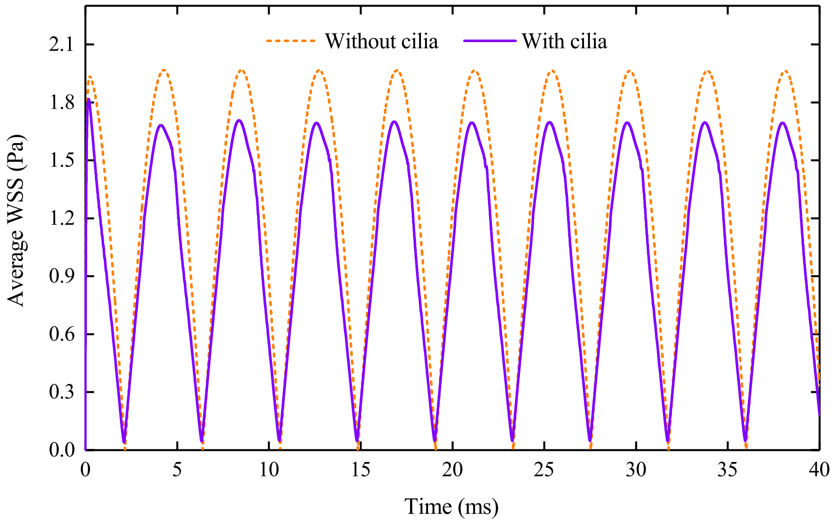

Fig. 4.11 Time evolutions of the average WSS in cases with and without cilia

To characterize the oscillatory features of the WSS field during oscillating cycles, we follow James et al. [163] to define an oscillatory shear index (OSI) which represents the disturbed flow patterns developed that result in the reverse flow velocity components occurring near the vessel walls. The OSI is calculated by

$$\mathrm{OSI} = \frac{1}{2}\left(1 - \frac{\left|\int_0^T \tau_x dt\right|}{\int_0^T |\tau_x| dt}\right) \tag{105}$$

where $T$ is the oscillating cycle, $\tau_x$ is the component of the WSS vector in the flow direction (i.e., the $x$-component). The value of OSI ranges from 0 to 0.5, with the value of 0 denoting a totally unidirectional WSS and the value of 0.5 denoting a purely unsteady and oscillatory flow with a net amount of zero WSS.

As the flow is driven by a sinusoidal pressure gradient waveform, the OSI at the bottom plate should be uniformly distributed with a value of 0.5 when there is no cilium presented. The OSI distribution in the presence of cilium is shown in Fig. 4.12. We can see that the OSI is not uniformly distributed, indicating that the presence of primary cilia affects the oscillation characteristic of the WSS. Though the primary cilium occupies only a very small portion of the wall area, its effect on the OSI distribution should not be underestimated: the affected region (i.e., the area has an OSI value less than 0.5) is taking up more than 50% of the wall area for the chosen case. Moreover, the regions in front of and behind the anchor points would be affected more considerably, while the regions above and below the anchor points turn out to be less affected. Each affected region in Fig. 4.12 resembles the shape of “8” and the cilium’s impact on the OSI value diminishes with distance.

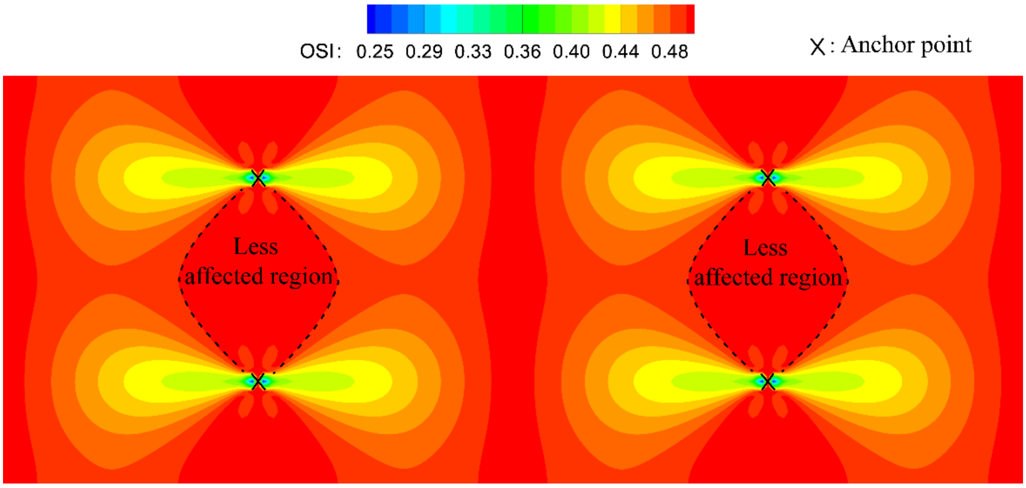

Fig. 4.12 OSI distribution due to the presence of primary cilia

## 4.3 Parametric study

### 4.3.1 Effect of the $Re_{peak}$

In this section, the dynamics of primary cilium at various $Re_{peak}$ is investigated. The $Re_{peak}$ is chosen at 0.05, 0.1, 0.15, 0.2, 0.3, and 0.4, respectively, while the $Wo$ is fixed at 0.6. The length ratio $L^*$ is set to 1/4 while the cilium spacing intervals in $x$- and $y$-directions are chosen as $L_d{}^* = 2.0$ and $W_d{}^* = 0.8$, respectively.

The simulated superpositions of the cilium profile at four different $Re_{peak}$ are shown in Fig. 4.13, where the trajectories of the tip positions are highlighted. When the $Re_{peak}$ increases, a larger flow drag will be applied to the primary cilium. As a result, the span of deflection increases, and the cilium behaves more complaint which further decreases the overall cilium length during the deflection process. At $Re_{peak}$=0.05, the tip trajectories between the forward and backward strokes nearly get overlapped. However, as the $Re_{peak}$ increases, the two trajectories start to make a difference, and when the $Re_{peak}$ exceeds 0.2, the tip trajectory resembles the shape of “8”.

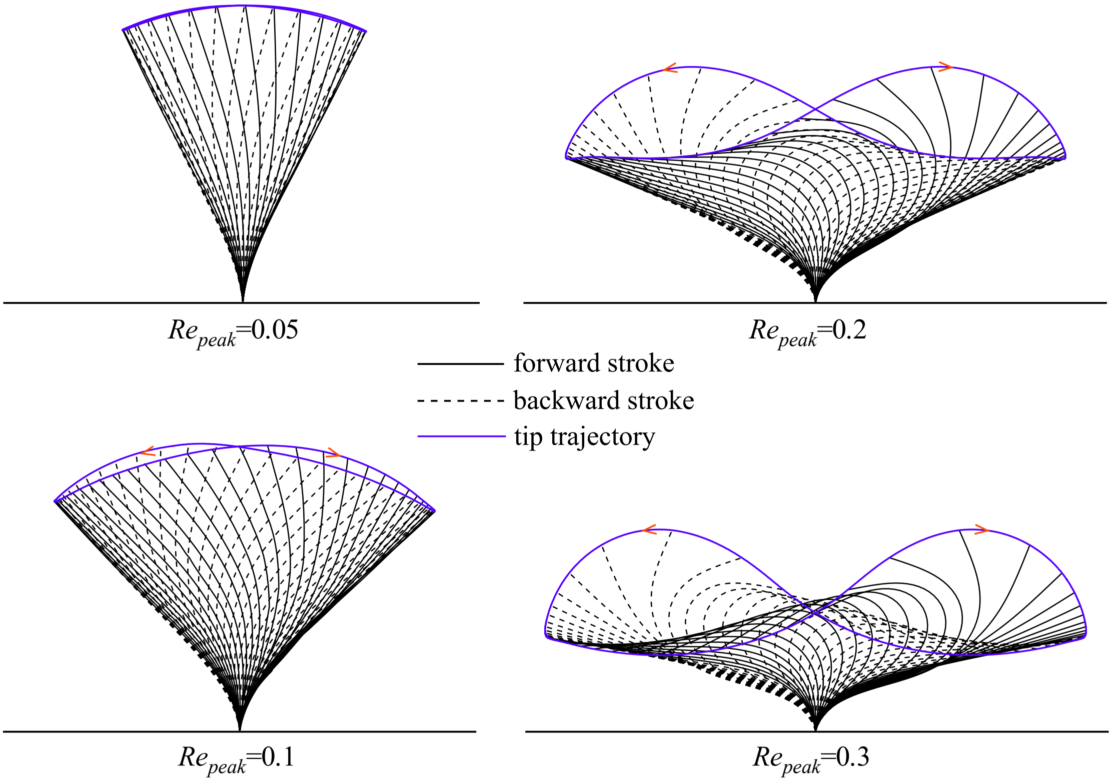

$Re_{peak}$=0.05 $Re_{peak}$=0.2

$Re_{peak}$=0.1 $Re_{peak}$=0.3

Fig. 4.13 Superpositions of the cilium profile at four different $Re_{peak}$

The time evolutions of the tip deflection at four different $Re_{peak}$ is shown in Fig. 4.14a. We can see that increasing the $Re_{peak}$ brings a larger tip deflection, which is an anticipated result and consistent with the result of Heys et al. [164]. It is also found that varying the $Re_{peak}$ will not change the phases of the tip deflection (i.e., the tip deflection varies synchronously at different $Re_{peak}$). Fig. 4.14b plots the maximal tip deflection as a function of $Re_{peak}$. The maximal tip deflection increases nonlinearly with the $Re_{peak}$, and we find the data can be well fitted by the following curve:

$$\delta_m^* = 0.93378 - 0.93256 * (9.1352\mathrm{e} - 6)^{\mathrm{Re_{peak}}} \tag{106}$$

where $\delta_m^* = \delta_m / L$ is the dimensionalized maximal tip deflection. The TAS at four different $Re_{peak}$ is plotted versus time in Fig. 4.15. An increase in the TAS can be observed when the flow $Re_{peak}$ increases, and when the $Re_{peak}$ is above 0.2, abrupt changes in the TAS can be observed when the cilium tip swings over its basal point due to the increased radical movement of the cilium tip.

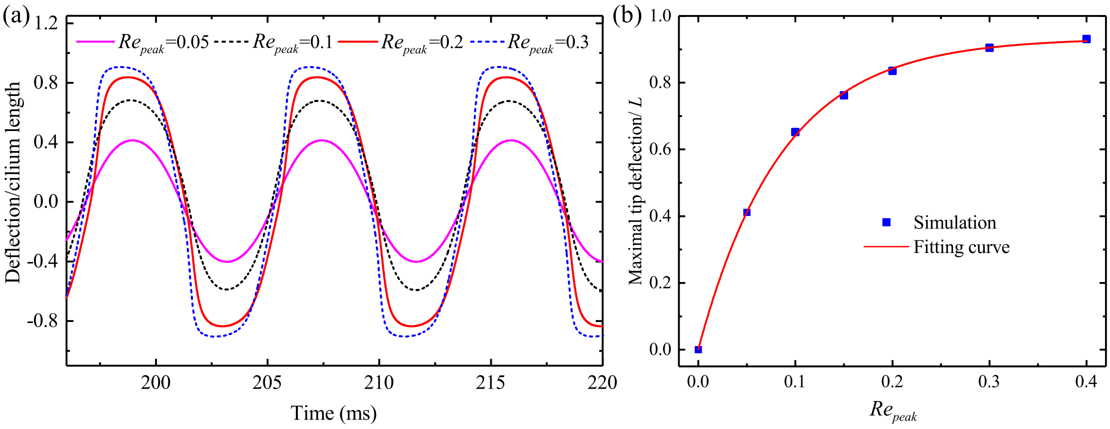

Fig. 4.14 Time evolutions of the tip deflection at four different $Re_{peak}$ (a) and the maximal tip deflection as a function of $Re_{peak}$ (b)

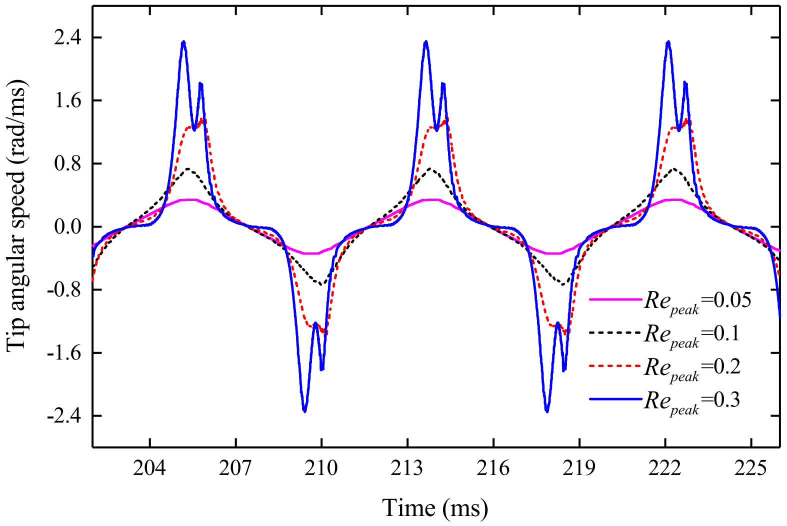

Fig. 4.15 Time evolutions of the TAS at four different $Re_{peak}$

The time evolutions of the maximal curvature and MTS location at four different $Re_{peak}$ are shown in Fig. 4.16a and b, respectively. When the $Re_{peak}$ is increased, a larger curvature can be obtained, and the evolution curve fluctuates more sharply. Propagation of the MTS location can be found in all chosen $Re_{peak}$ cases. The MTS location can only propagate for a maximal distance of $0.42L$ from the base at $Re_{peak}$=0.05. However, the distance increases to $0.62L$ when the $Re_{peak}$ is increased to 0.3. This suggests that the higher the $Re_{peak}$, the closer the MTS location can be propagated to the cilium tip. Apart from that, increasing the $Re_{peak}$ also promotes such propagation as the MTS location is observed to stay at the base region for a reduced time period when $Re_{peak}$ increases.

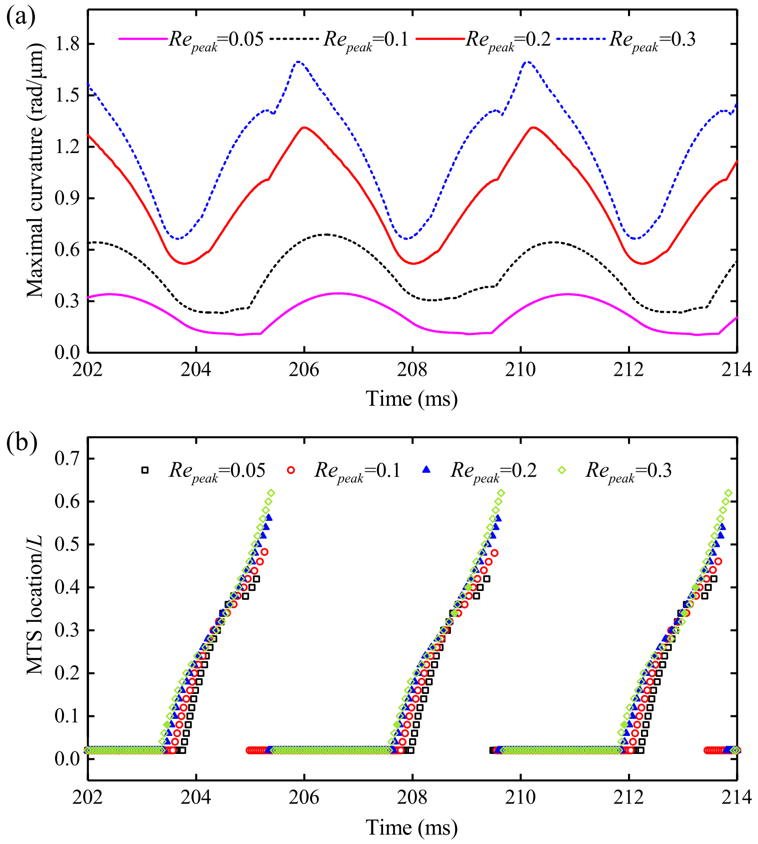

Fig. 4.16 Time evolutions of the maximal curvature (a) and MTS location (b) at four different $Re_{peak}$

The time evolutions of the average WSS for cases with and without cilia at three different $Re_{peak}$ are shown in Fig. 4.17a. The average WSS is found to increase monotonically with the $Re_{peak}$. Compared with the corresponding without-cilia case, a decrease (time-averaged) in the spatially-averaged WSS can be observed in all the simulated $Re_{peak}$ cases when primary cilia are presented. Fig. 4.17b plots the decrease in the average WSS caused by the presence of cilia at various $Re_{peak}$. The decrease is found to increase first and then decrease with the $Re_{peak}$. The turning point is found at $Re_{peak}$=0.2, where the decrease in the average WSS reaches its maximum, at a percentage of nearly 19%. The OSI distributions at four different $Re_{peak}$ are depicted in Fig. 4.18. A larger affected region with lower OSI values can be observed for a higher $Re_{peak}$.

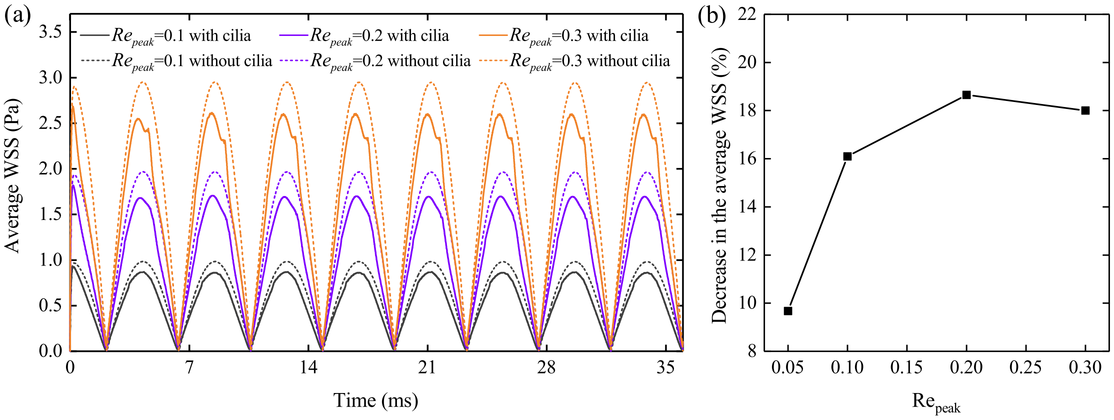

Fig. 4.17 Time evolutions of the average WSS in cases with and without cilia at different $Re_{peak}$ (a) decrease in the average WSS due to the presence of cilia at various

$Re_{peak}$ (b)

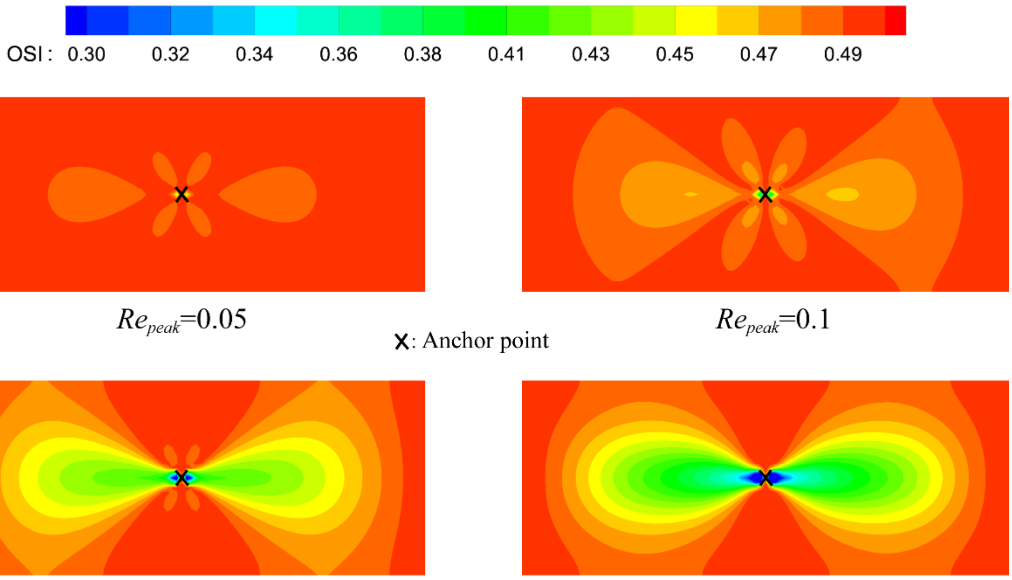

$Re_{peak}$=0.05

$Re_{peak}$=0.1

X: Anchor point

$Re_{peak}$=0.2

$Re_{peak}$=0.3

Fig. 4.18 OSI distributions at four different $Re_{peak}$

### 4.3.2 Effect of the *Wo*

The *Wo* is another important dimensionless number in cardiovascular system, which expresses the ratio of the oscillatory inertia force to the viscous/shear. In different types of human blood vessels, this number varies significantly due to the variations in vessel size across the vasculature system. Based on the vessel size we chose, simulations of the deflections of the primary cilium at a *Wo* range of 0.4-1.5 were performed at a fixed $Re_{peak}$ of 0.2. Varying of Wo here is achieved by altering the oscillating frequency $f$ in Equation (100) to save computational cost. The length ratio $L^*$ is set to 1/4 while the cilium spacing intervals in $x$- and $y$-directions are chosen as ${L_d}^* = 1.5$ and ${W_d}^* = 0.6$, respectively.

The simulated cilium profiles in one oscillating cycle at four different Wo are shown in Fig. 4.19. An increase in the $Wo$ will lead to a decrease in the span of deflection, and the primary cilium appears to be more flexible at low-$Wo$ cases as it deforms more significantly. The primary cilium deflects (its potential energy increases) because of the kinetic energy it harvested from the fluid flow. When the $Wo$ increases, the kinetic energy that a cilium can harvest will decrease in an oscillating cycle $T$ due to the rapid change of the pressure gradient ($T$ will decrease, thus the summation of the driven force over $T$ (i.e. applied energy) will also decrease). Fig. 4.20a plots the maximal tip deflection at various $Wo$ cases. It is found that the maximal tip deflection is inversely related to the $Wo$, and their relationship can be well fitted by the following polynomial:

$$\delta_m^* = 0.3525 + 3.5869Wo - 7.2810Wo^2 + 5.0141Wo^3 - 1.1905Wo^4 \qquad (107)$$

Compared with the applied pressure gradient, a phase lag in the tip deflection can be observed for all simulated $Wo$ cases (see Fig. 4.20b). The minimal phase lag is found at $Wo$=0.4 among the selected cases. For the cases with $Wo$>0.4, the phase lags between different cases are quite close, and the value is about 0.6π.

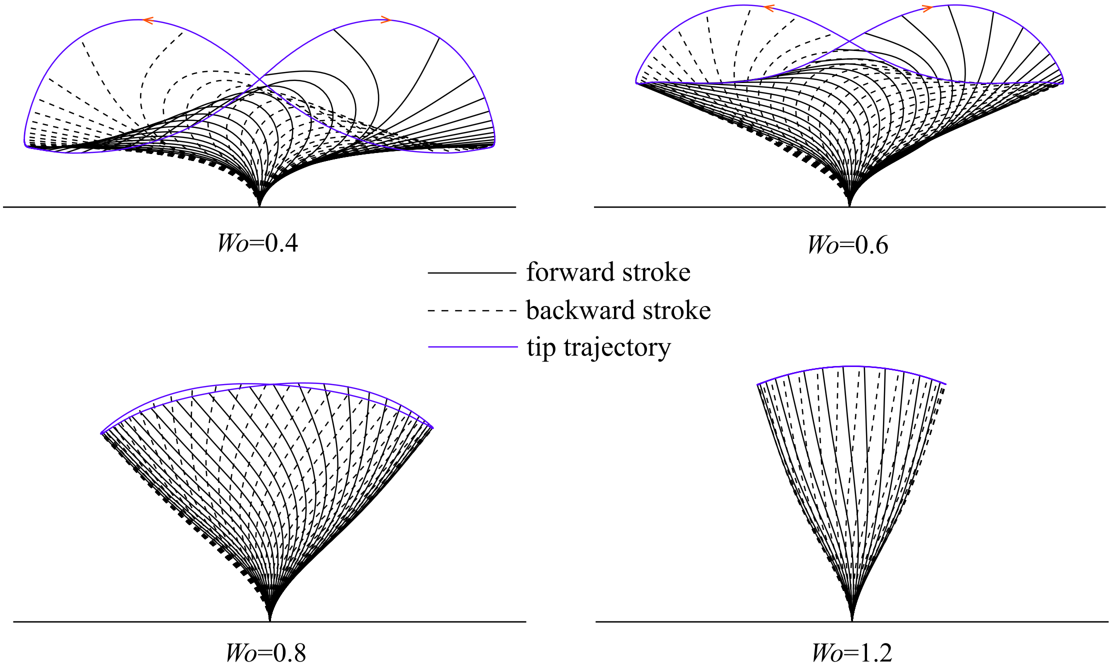

*Wo*=0.4 *Wo*=0.6 *Wo*=0.8 *Wo*=1.2

Fig. 4.19 Superpositions of the cilium profile at four different *Wo*

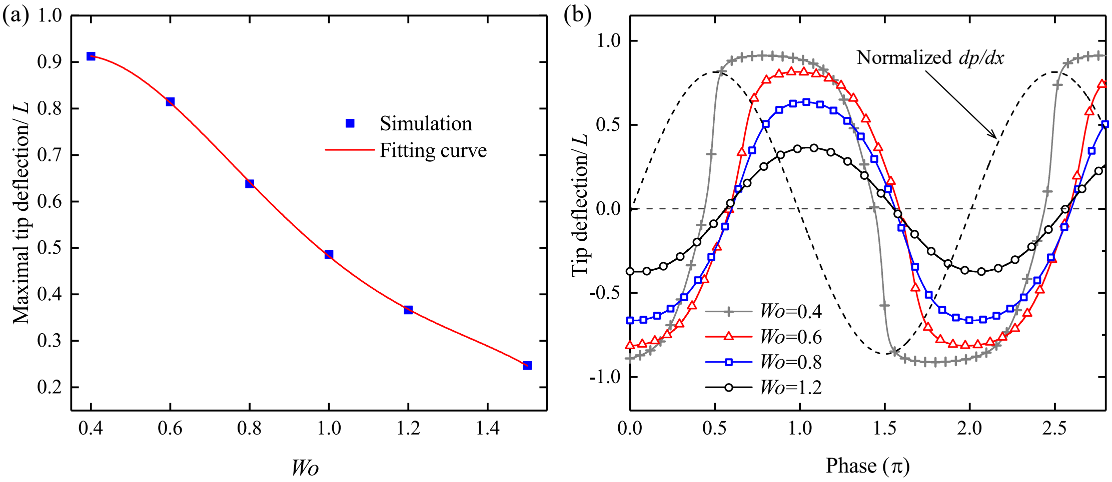

Fig. 4.20 The maximal tip deflection as a function of *Wo* (a) and phase lags in tip deflection for different *Wo* (b)

The phasic evolutions of the TAS and maximal curvature at four different *Wo* are displayed in Fig. 4.21a and b, respectively. A phase difference in both these two quantities is observable among different *Wo*. The amplitude of the TAS only varies slightly with the *Wo*. However, the profiles of the curve at different Wo can be very different. The curve is smooth for the cases with *Wo* larger than 0.8. For the other cases, the TAS varies more sharply and there are small fluctuations observable around those peaks and valleys. Increasing the *Wo* will also lead to a decrease in the maximal curvature (see Fig. 4.21b) and the maximal propagation distance of the MTS location (see Fig. 4.21c).

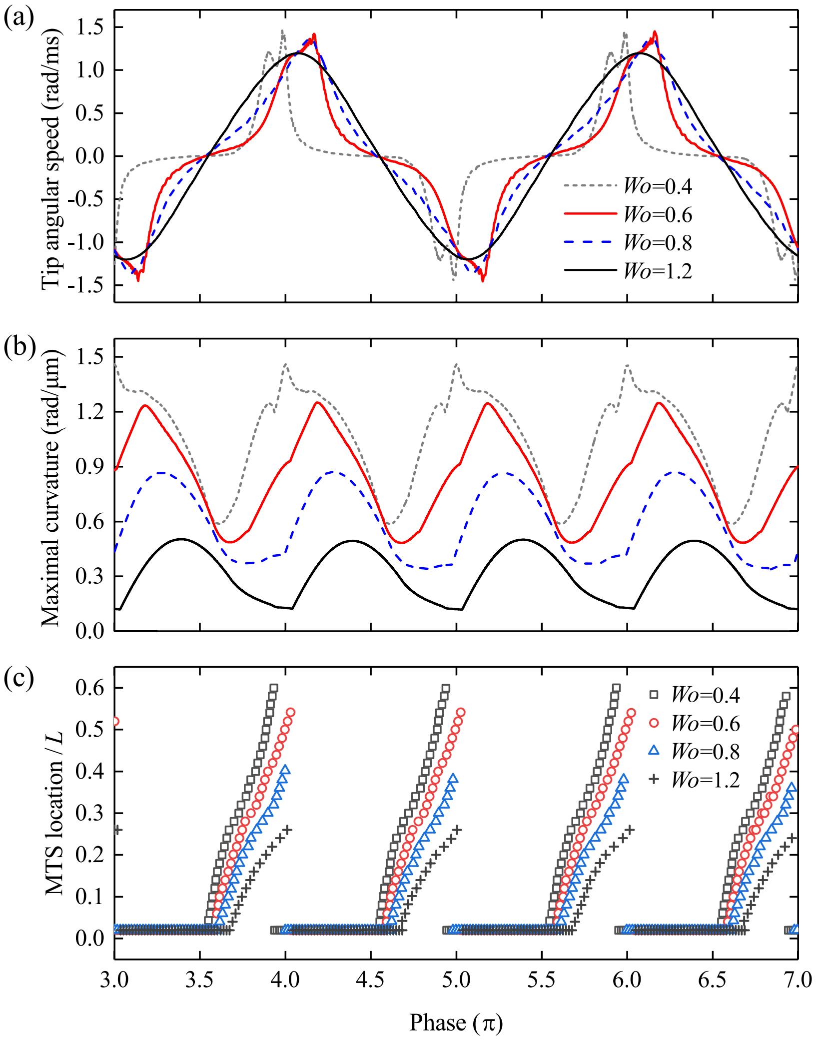

Fig. 4.21 Phasic evolutions of the TAS (a), maximal curvature (b), and scaled MTS location (c) at four different *Wo*

Fig. 4.22a shows the phasic evolutions of the average WSS in the cases with and without cilia for various *Wo*. When the primary cilia are absent, the phasic evolution of the average WSS does not vary with the *Wo*. Therefore, we do not show them repeatedly in the figure while only present one of them. For all the selected *Wo*, the average WSS tends to be lower when cilia are presented, and the smaller the *Wo*, the lower the average WSS. Fig. 4.22b plots the decrease in the average WSS due to the presence of cilia at various *Wo*. We can see that the decrease drops almost linearly with the *Wo*, which shows a similar trend with the maximal tip deflection shown in Fig. 4.20a. The effect of primary cilia on the OSI distribution at four different *Wo* is presented in Fig. 4.23. A larger affected region (the region with OSI value less than 0.5) with smaller OSI value can be observed in the case with a lower *Wo*.

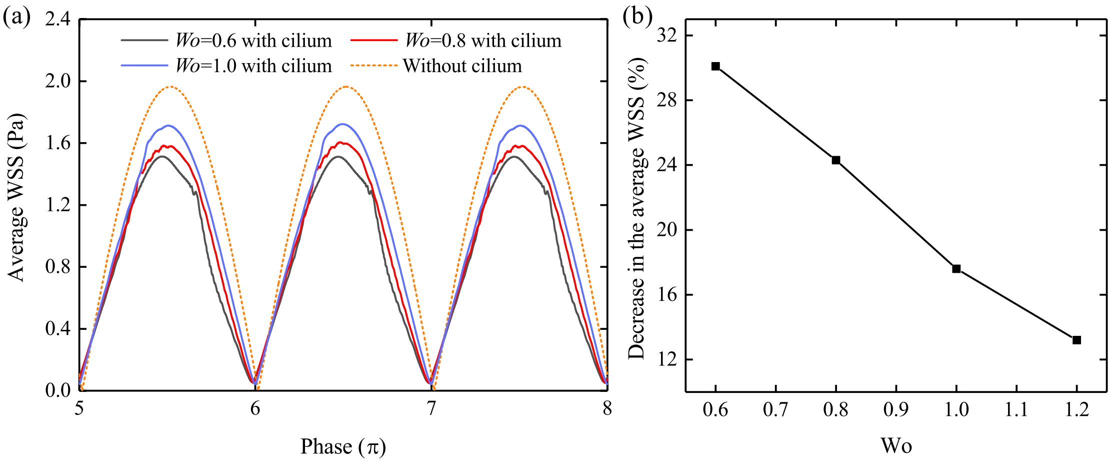

Fig. 4.22 Phasic evolutions of the average WSS in cases with and without cilia for various *Wo* (a) decrease in the average WSS due to the presence of cilia at various *Wo* (b)

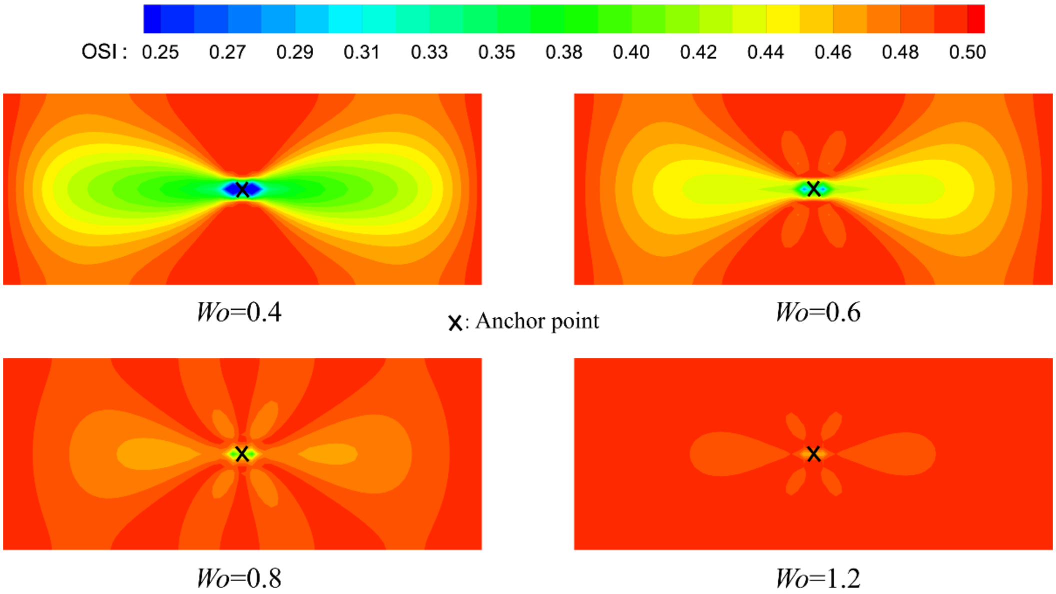

Fig. 4.23 OSI distributions at four different *Wo*

### 4.3.3 Effect of the cilium length

The primary cilium can dynamically alter its length to regulate its mechanosensitive response [159, 165, 166]. We therefore investigated the effect of the length ratio $L*$ (i.e. $L *= L/D$, which characterizes how much the cilium extends into the lumen) on the cilium dynamics. In our current study, three different cilium length are considered by setting the length ratios as $L*$=1/6 (short), 1/4 (medium), and 1/3 (long), respectively. The chosen $Re_{peak}$ and *Wo* is 0.2 and 0.6, respectively, and the spacing intervals are set as $L_d{}^*$=2.0 and $W_d{}^*$=0.8.

The simulated superpositions of the cilium profile in a flapping cycle at three different $L*$ are presented in Fig. 4.24. There is an obvious difference among these superpositions. Due to the fluid viscosity, the velocity at the near-wall region is much lower compared to that in the center region. A larger velocity will bring a larger flow drag. Therefore, a shorter cilium is observed to has a smaller deflection and a more rigid (straighter) profile (see Fig. 4.24). When $L*$ increases, the cilium extends more into the lumen, which allows the cilium to collect more flow information. In the meanwhile, it is exposed to a larger hydrodynamic load, which will deflect it more significantly (see Fig. 4.26a). Therefore, in the case of sensing a weak flow, a primary cilium can amplify the flow information by increasing its length extending into the lumen. Interestingly, for a long cilium that extends into 1/3 of the lumen, some of its profiles are found to vary twice in the curvature direction due to the increased inertial force obtained at its tip section. In that case, the base, middle and tip sections of the cilium will be under their own stress sates different from their neighbors'. This is the third stretch state observed in our simulation (see its schematic diagram in Fig. 4.25). Though a longer cilium will have a larger tip deflection under the same flow condition (see Fig. 4.26a), the scaled cilium deflections for different $L*$ turn out to be very close, as can be seen from Fig. 4.26b.

From Fig. 4.26a and c, we can see that a smaller phase lag in both the tip deflection and TAS is observed when the length ratio is reduced to $L*$=1/6, whereas no obvious phase differences in these two quantities are observable between the medium and long cilia. This implies that a primary cilium may be able to adjust its response speed via altering its length. Unlike the tip deflection, a decrease in the TAS is observable when the cilium becomes longer, as shown in Fig. 4.26c.

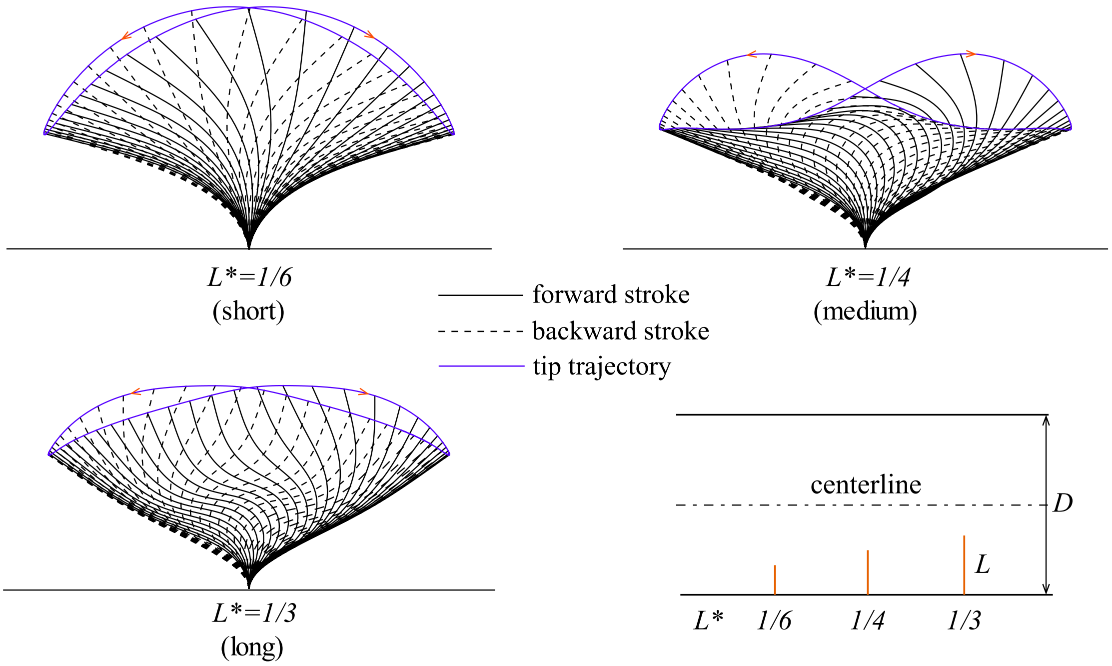

Fig. 4.24 Simulated superpositions of the cilium profile in a flapping cycle at three different $L^*$ (each profile is scaled by its own cilium length $L$)

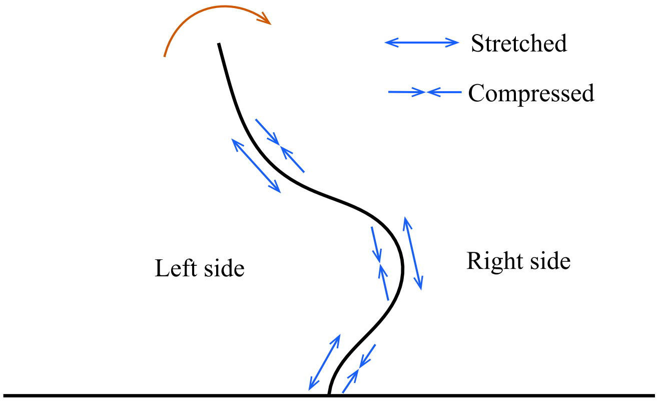

Fig. 4.25 Stretch state 3 observed for $L^*$=1/3

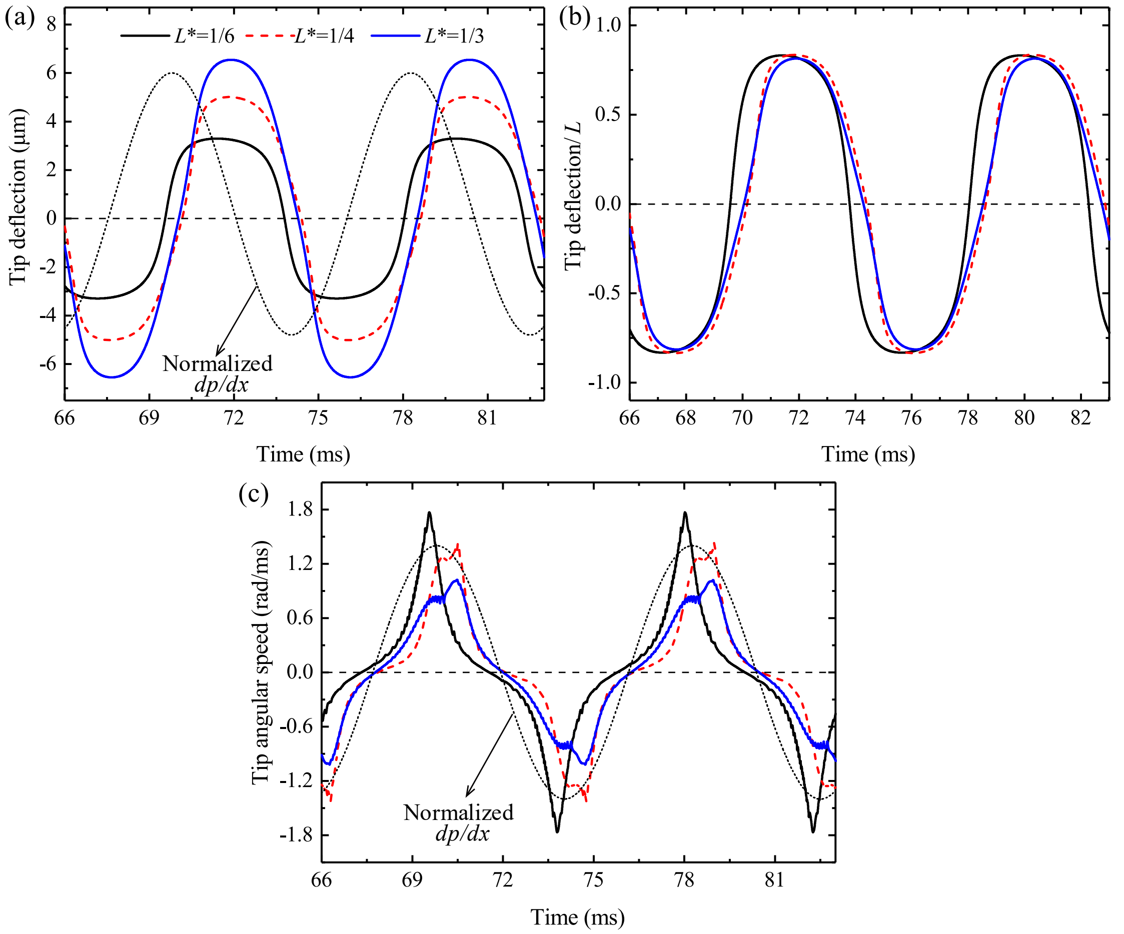

Fig. 4.26 Time evolutions of the unscaled (a) and scaled (b) tip deflection and TAS (c) at three different $L*$

Fig. 4.27 shows the time evolutions of the maximal curvature for three different $L*$. The maximal curvature increases nonlinearly with the length ratio $L*$. A dramatic increase in the maximal curvature is observed when the $L*$ is increased from 1/6 to 1/4. However, the further increase of $L*$ to 1/3 only leads to a very limited increment in the maximal curvature. Nonetheless, a longer cilium can still be viewed as a more sensitive mechanotransducer due to its increased membrane strain (i.e., the curvature in our study) at the same flow condition.

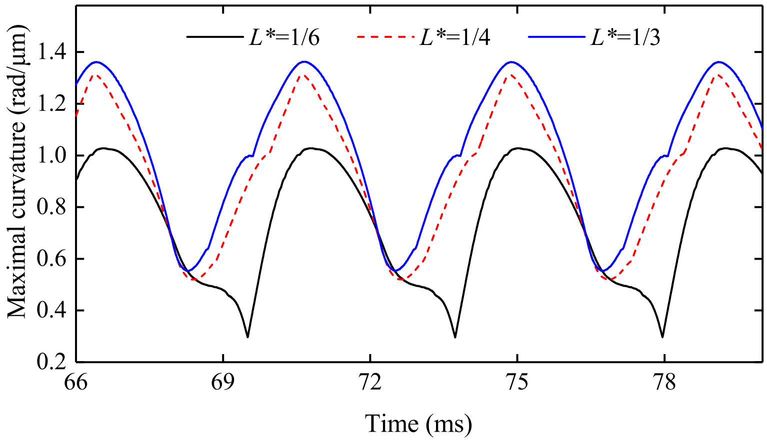

Fig. 4.27 Time evolutions of the maximal curvature for three different *L**

The time evolutions of the scaled MTS location for three different *L** are shown in Fig. 4.28a. Propagation of the MTS location is observable in all the three simulated cases. Fig. 4.28b plots the maximal propagation distances (scaled) as a function of *L**. An increase in the propagation distance is observed when the *L** is increased from 1/6 to 1/4. However, the distance starts to drop as the length ratio further increases to *L**=1/3. The drop is very likely due to a third curvature direction (see Fig. 4.25) occurs during the cilium deflection in the case of *L**=1/3.

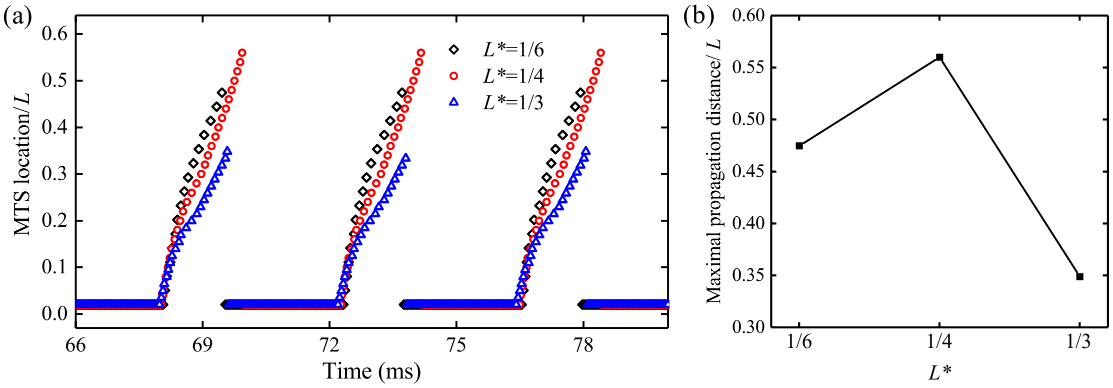

Fig. 4.28 Time evolutions of the scaled MTS location for three different *L** (a) and the scaled maximal propagation distances as a function of *L** (b)

The time evolutions of the average WSS in the cases with and without cilia for various $L^*$ are shown in Fig. 4.29a. Fig. 4.29b shows the decrease in the average WSS due to the presence of cilia at various $L^*$. The decrease increases monotonically with the $L^*$, indicating that a longer cilium will reduce the WSS more remarkably. The effect of $L^*$ on the OSI distribution is shown in Fig. 4.30, where the cilium with a medium length ratio has a larger impact on the OSI distribution compared to the short one.

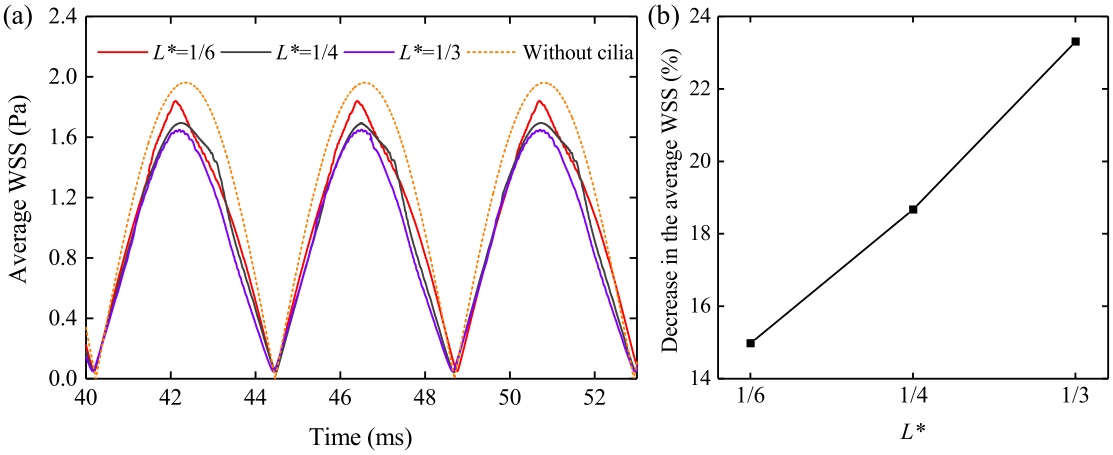

Fig. 4.29 Time evolutions of the average WSS in cases with and without cilia for various $L^*$ (a) decrease in the average WSS due to the presence of cilia at various $L^*$ (b)

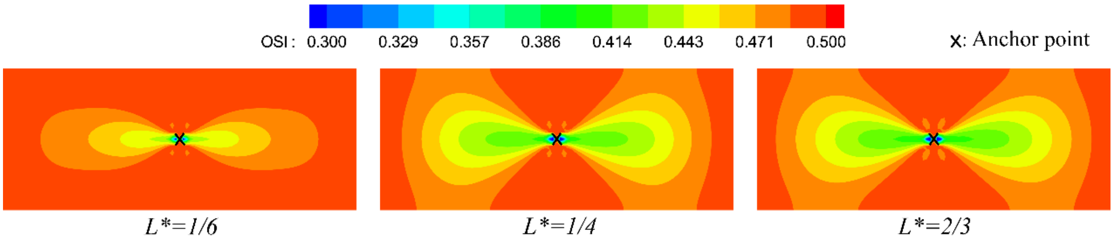

Fig. 4.30 OSI distributions at three different $L^*$

### 4.3.4 Effect of the spacing interval

The effect of cilium spacing interval on cilium dynamics was also investigated in this study. Since the spacing interval in the y-direction ($W_d$*) has a far less significant impact on cilium deflection, this study only covers the spacing interval in the flow direction (i.e. the x-direction, denoted by $L_d$*). Simulations were run at $Re_{peak}$=0.2, $Wo$=0.6, $L$*=1/4, and $W_d$*=0.8. The chosen $L_d$* is 0.5, 1.0, 2.0, and 3.0, respectively. A smaller value of $L_d$* represents a denser arrangement of the cilia array in the x-direction, while a larger value means a sparser arrangement.

Fig. 4.31 shows respectively the time evolutions of the scaled tip deflection and TAS at different $L_d$*. Fig. 4.32a shows the time evolution of the maximal curvature at four different $L_d$* and Fig. 4.32b plots the maximal propagation distance as a function of $L_d$*. For cilia arrays with spacing intervals $L_d^* \leq 2.0$, an increase in the tip deflection, maximal curvature, and maximal propagation distance can be observed when the arrangement becomes sparser. However, for those cilia arrays with spacing intervals $L_d^* \geq 2.0$, these quantities turn out to be nearly identical.

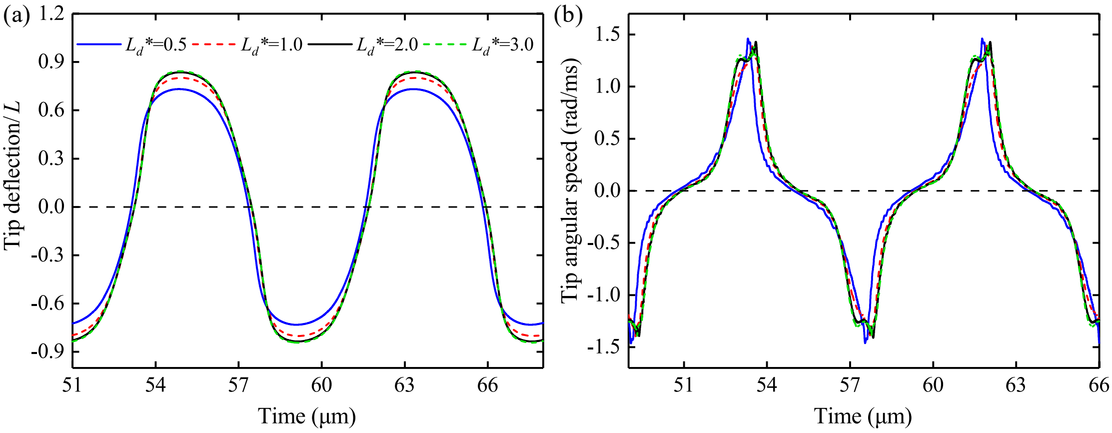

Fig. 4.31 Time evolutions of the scaled tip deflection (a) and TAS (b) at four different

$L_d$*

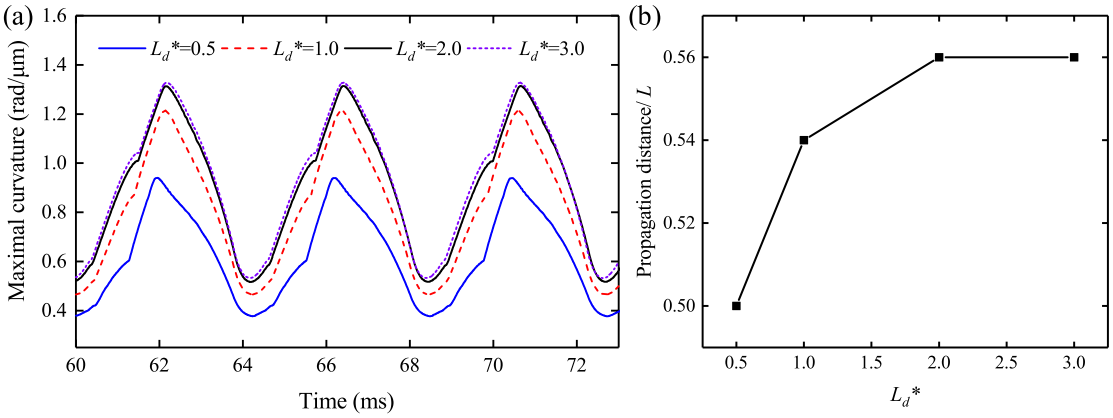

Fig. 4.32 Time evolution of the maximal curvature at four different $L_d$* (a) and the scaled maximal propagation distance as a function of $L_d$* (b)

The recirculation zones at three different spacing intervals are presented in Fig. 4.33. In synchronized cilia arrays, neighboring cilia interact with each other via surrounding fluid. For a denser cilia array, the two adjacent recirculation zones interact with each other. However, as the spacing interval grows, the interacting becomes weaker. Once the spacing interval exceeds twice the cilium length (i.e. $L_d$*≥ 2.0), the spacing interval is found to have a nearly negligible impact on the cilium dynamics. A sufficiently large spacing interval (i.e. $L_d$*≥ 2.0) thus can be beneficial to improve the sensing accuracy of primary cilia as it reduces the interference from the neighboring cilia. This could be the reason why there is only one primary cilium at most for each endothelial or epithelial cell whose diameter happens to be about 2-3 times the length of primary cilium, which falls into this range.

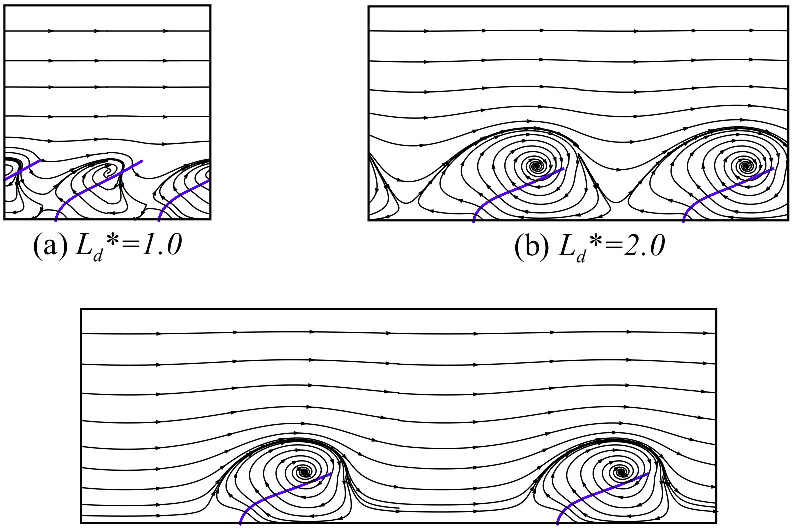

(a) $L_d^*=1.0$ (b) $L_d^*=2.0$

(c) $L_d^*=3.0$

Fig. 4.33 Recirculation zones at three different spacing intervals

The time evolutions of the average WSS in the cases with and without cilia for various $L_d^*$ are shown in Fig. 4.34a, where a lower average WSS is found for the case with a denser cilia array. The decrease in the average WSS due to the presence of cilia at various $L_d^*$ is plotted in Fig. 4.34b. The greatest decrease is found in the case of $L_d^*=0.5$ at a percentage more than 50%, meaning the average WSS is more than halved at such spacing interval compared to that of the without-cilia case. The decrease in the average WSS is also observed to be sharper for a denser cilia array.

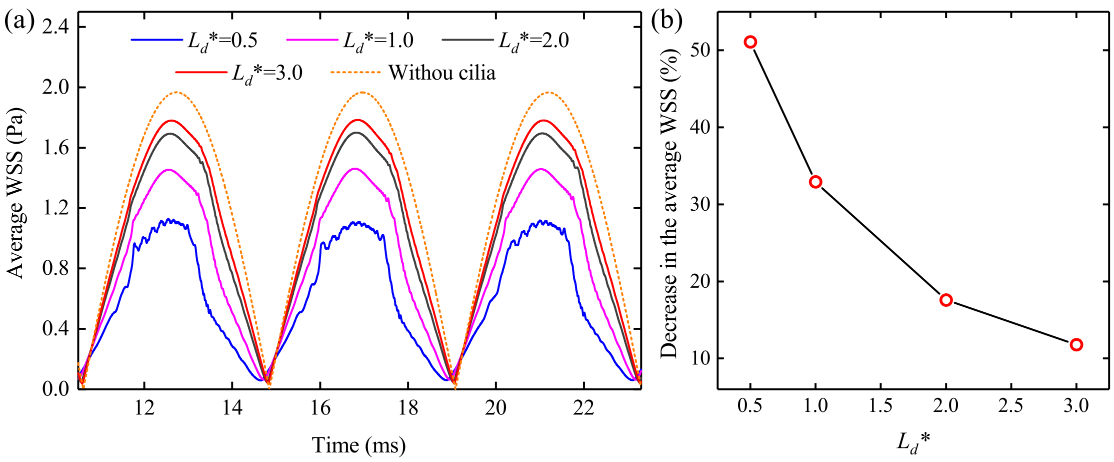

Fig. 4.34 Time evolutions of the average WSS in the cases with and without cilia for various $L_d$* (a) decrease in the average WSS due to the presence of cilia at various $L_d$* (b)

The OSI distributions at four different $L_d$* are shown in Fig. 4.35, where the affected region (i.e., region with OSI value less than 0.5) are divided into different subregions based on their locations. When $L_d$*≤ 2.0, the shapes of the affected region vary significantly with the spacing interval. When $L_d$*=0.5, there are only two subregions (i.e., subregion 2 and 3) visible, and the region in front of and behind the cilium (i.e., subregion 1) is too small to be noticed. For a spacing interval sparser than 0.5, we can observe three subregions, and as $L_d$* increases, subregion 1 will get expanded while subregion 2 and 3 will diminish. When $L_d$*≥ 2.0, subregion 1 dominates the affected region and the no significant variation on the OSI distribution can be observed when the $L_d$* further get increased, indicating that an enough separated cilium arrangement is obtained.

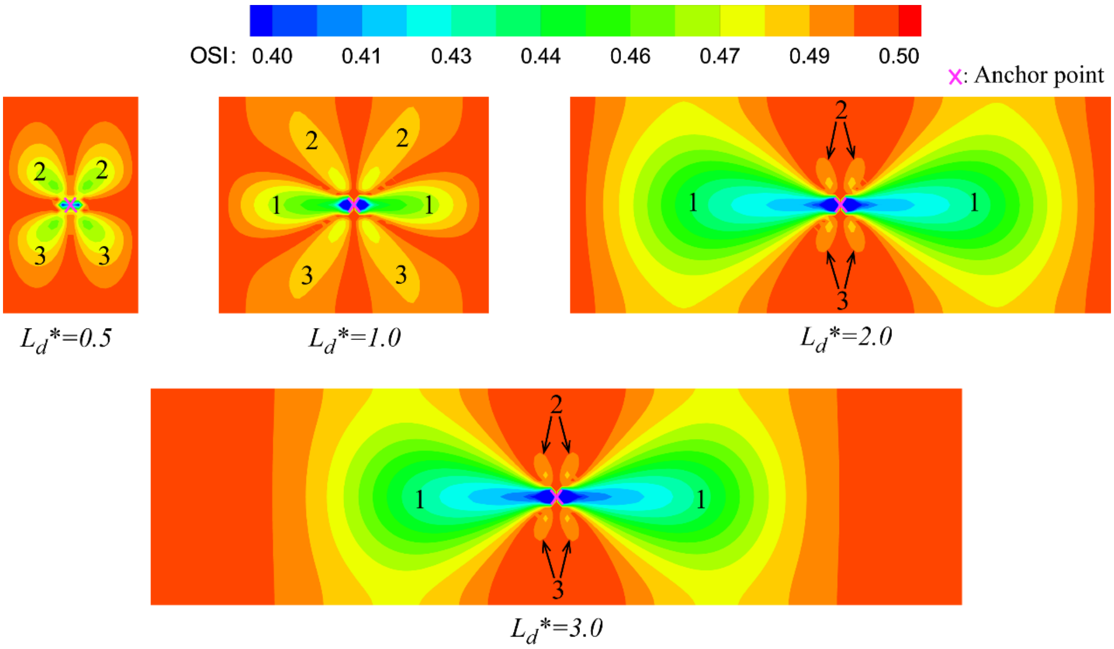

Fig. 4.35 OSI distributions at four different $L_d$*

## 4.4 Summary

The dynamics of primary cilia in an oscillating Newtonian flow is numerically studied in this chapter. The oscillating flow is driven by a sinusoidal pressure gradient waveform. The primary cilia are assumed to move synchronously, and present at the bottom and upper plates periodically and symmetrically. The deflection process and the impact of primary cilia on the flow field are analyzed and discussed first. After that, a parametric study which covers the $Re_{peak}$, the $Wo$, the cilium length, and the spacing interval, is performed to investigate how these parameters affect the flow-cilia interaction. Based on our simulation results, the following conclusions can be drawn.

(1). The primary cilia are observed to do an in-plane flapping motion which is symmetrical in term of the cilium profile. Among all the simulated cases, three typical stretch states are captured. In the first stretch state, the direction of the profile curvature does not vary along the cilium length, making one side of the ciliary membrane under stretch while the other under compression throughout the cilium length. In the second stretch state, the direction of the profile curvature is found to vary once along the cilium length. As a result, each side of the ciliary membrane will be partially under stretch and partially under compression. The third stretch state is observed for a long cilium that extends into 1/3 of the lumen. In this state, the cilium's profile is found to vary twice in the curvature direction. In that case, the base, middle and tip sections of the cilium will be under their own stress sates which may be different from each other.

(2). The MTS location may not always stay at the cilium's base region, instead it is found to periodically propagate from the cilium's base point to its tip by a certain distance. For primary cilia with short and medium length, an increase in the maximal tip deflection is accompanied with a greater propagation distance. While this may not necessarily apply to long primary cilia, as the possible occurrence of the third stretch state may greatly suppress the propagation of the MTS location.

(3). The flow-induced curvature at the lower part of the primary cilium is well synchronized with the applied pressure signal, while an obvious phase lag in the curvature is observed for the rest parts of the cilium. A smaller phase lag means a fast respond speed and less delay. Therefore, it would be reasonable to speculate that the lower part of primary cilia may be responsible for detecting the variations of the flow information.

(4). The presence of primary cilia slows down the velocity in the near-wall region and decreases the average WSS level. Under the same flow condition, the decrease is found to be more significant when a cilium undergoes a larger span of deflection and/or when the spacing interval is reduced. Compared with the spacing interval, the span of deflection plays a marginal role in decreasing WSS. The presence of primary cilia is also found to affect the oscillation characteristic of the WSS by making the WSS in some regions less oscillatory.

(5). For the ranges of parameters considered, an increase in the $Re_{peak}$ or cilium length is found to bring a larger span of cilium deflection and maximal curvature. An increase in the *Wo*, however, is found to decrease these two quantities. For a constant spacing interval, a larger span of deflection is found to correspond to a more uneven OSI distribution.

(6). In a cilia array, neighboring cilia interact with each other via surrounding fluid. The interacting becomes weaker as the spacing interval increases. A sparser cilia array therefore tends to have a larger span of cilium deflection, maximal curvature, and propagation distance of the MTS location. For a medium $Re_{peak}$ and *Wo*, our simulation suggests that a spacing interval greater than twice the cilium length could effectively reduce the interference from the neighboring cilia thus improves cilium's sensing accuracy. This could be the reason why there is only one primary cilium at most for each endothelial or epithelial cell whose diameter happens to be about 2-3 times the length of primary cilium.

# Chapter 5 Cilium dynamics in an oscillating non-Newtonian fluid flow

In the previous chapter, we have studied the dynamics of primary cilia embed in a Newtonian fluid. Actually, this is the case considered in most of the published papers that involve the simulation of the dynamics of primary cilium. However, what happens when the fluid becomes non-Newtonian? This situation should be expected when it comes to the blood flow. The blood is a concentrated suspension containing a variety of blood cells. Experimental studies have demonstrated that blood flow exhibits non-Newtonian behavior such as shear thinning, thixotropy, viscoelasticity, and yield stress [167]. Thus, it is more appropriate to consider blood as non-Newtonian fluid, especially in microvessels (vessels that have a diameter of 100μm or less) where its non-Newtonian nature becomes even more obvious. As the flow's non-Newtonian effect may play a role in governing cilium dynamics, in this chapter, the dynamics of primary cilium in non-Newtonian fluid will be numerically investigated.

## 5.1 Power-law model

The viscosity of the non-Newtonian fluid is characterized by a power-law model. As one of the most popular non-Newtonian viscosity models, the power-law model can model both pseudo-plastic and dilatant material behavior. In this model, the viscosity $\upsilon$ of the fluid is assumed shear-rate $\dot{\gamma}$ dependent, and their relationship can be expressed as:

$$\upsilon = m\dot{\gamma}^{n-1} \tag{108}$$

where $m$ is the consistency index, which has the units $\mathrm{m}^2\mathrm{s}^{n-2}$. $n$ is the power-law index, which determines the response of the fluid to the variation of shear rate. For $n < 1$, the fluid is shear thinning (pseudo-plastic), for $n = 1$ the fluid is Newtonian and for $n > 1$ the fluid is shear thickening (dilatant). The shear rate can be calculated by:

$$\dot{\gamma} = \sqrt{2D_{II}} \tag{109}$$

where $D_{II}$ is the second invariant of the strain rate tensor, and it is defined as,

$$D_{II} = \sum_{\alpha,\beta=1}^{3} S_{\alpha\beta}\, S_{\beta\alpha} \tag{110}$$

in three-dimensional, where $S_{\alpha\beta}$ is the strain rate tensor, which is defined as,

$$S_{\alpha\beta} = \frac{1}{2}\left(\nabla_\beta u_\alpha + \nabla_\alpha u_\beta\right) \tag{111}$$

In N-S solvers, it is necessary to calculate the derivations of the velocity gradient to obtain $S_{\alpha\beta}$, which complicates the non-Newtonian flow simulation and greatly increases the computational load. In the LBM with body force presents, the strain rate tensor can be calculated locally and efficiently at each grid point by

$$S_{\alpha\beta} = \frac{-3}{2\rho_0 c^2 \tau \Delta t} \sum_i c_{i\alpha} c_{i\beta}\left(f_i - f_i^{eq}\right) + S_{\alpha\beta}^{ext} \tag{112}$$

In Guo et al.'s split forcing scheme, $S_{\alpha\beta}^{ext}$ is computed by [168],

$$S_{\alpha\beta}^{ext} = \frac{(1 - \frac{1}{2\tau})}{c_s^2} \boldsymbol{F} \cdot \boldsymbol{F} \tag{113}$$

The Reynolds number for non-Newtonian fluid simulated with power-law model can be defined as,

$$Re_{PL} = \frac{u_0^{2-n} D^n}{m} \tag{114}$$

where $u_0$ is the maximal (central) velocity of the channel and $D$ the characteristic length (in our case the distance between the two parallel plates).

## 5.2 Validations of the power-law model

The LBM with power-law non-Newtonian viscosity model was validated by simulating a pressure gradient driven non-Newtonian fluid flow in a 3D box, which is bounded by two infinite parallel plates. The half-way BB scheme was implemented to enforce the no-slip boundary condition at the plates and for the rest boundaries, periodic boundary conditions are assumed. The pressure gradient is generated by applying a body force density on each lattice node. Simulations were run at $Re_{PL}$=0.3, and the power-law index is chosen as *n*=0.5, 1.0, and 1.5, respectively. Our simulated results were compared to the analytical solution, which is given by [169],

$$U(z) = \left(\frac{\Delta P}{mL}\right)^{\frac{1}{n}} \left(\frac{n}{n+1}\right) \left[ \left(\frac{D}{2}\right)^{\frac{n+1}{n}} - \left(\left|\frac{D}{2} - z\right|\right)^{\frac{n+1}{n}} \right] \tag{115}$$

where $\Delta P/L$ is the pressure gradient in the flow direction.

The comparison of the LB simulation result and the analytical solution at various *n* is shown in Fig. 5.1, where we can see that our simulated velocity profiles closely match the analytical ones. When *n*=1.0, *m*=*v*, the fluid is Newtonian, thus the velocity shows a parabolic profile. As *n* is decreased to 0.5, the fluid becomes shear-thinning, and its viscous effect becomes less significant in the high-shear region (near-wall region), thus its velocity profile is flatter. When *n*=1.5, the fluid behaves shear thickening, and the viscous effect is more obvious in the high-shear region. As a result, greater curvature is observed around the central peak velocity.

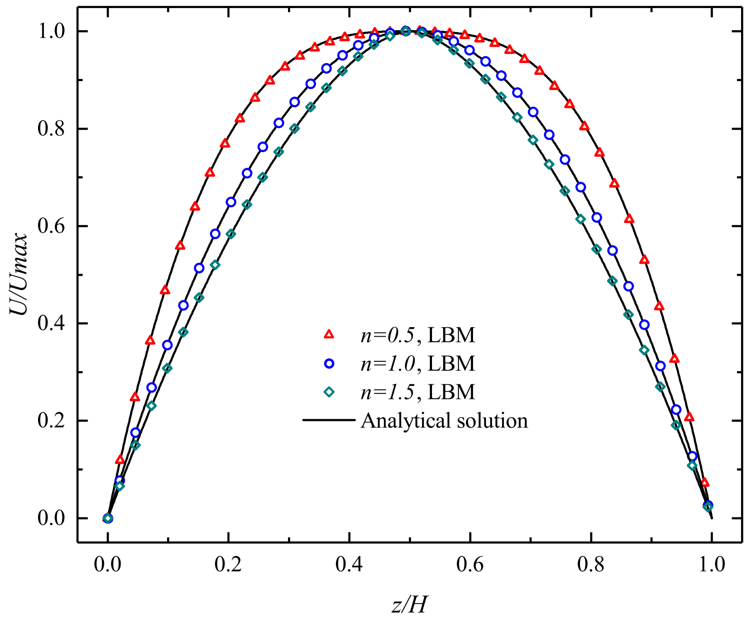

Fig. 5.1 The simulated velocity profiles (normalized) at different *n*

## 5.3 Simulation setup

With the power-law model been well validated, we now apply it to study the cilium dynamics in oscillating non-Newtonian fluid flow. The flow is still driven by a sinusoidal pressure gradient waveform, and the simulation domain is a cuboid box similar to the one used in Chapter 4, with a dimension of $1.5L(L_d) \times 0.5L(W_d) \times 2L(H_d)$. We keep the grid spacing, boundary conditions, and the other physical parameters the same as the studied Newtonian case in Chapter 4. The chosen peak $Re_{PL}$ is 0.3 and *Wo* 0.8. Five power-law indexes are considered in our simulations with the value of *n* being 0.5, 0.7, 1.0, 1.2, and 1.5, respectively, where *n*=1.0 corresponds to the Newtonian case.

## 5.4 Simulation results

The simulated superpositions of the cilium profile in a flapping cycle at five different $n$ are presented in Fig. 5.2. The symmetry in the superposition is perfectly maintained for $n$ below 1.2, as can be seen clearly from the tip trajectories highlighted in Fig. 5.2. However, this symmetry is found to be broken in the case of $n$=1.5, where the fluid shows an apparently shear-thickening characteristics. This could lead to a sensory failure, as the primary cilium does not successfully capture the symmetry of the input pressure signal through its passive deflection. In the asymmetric case, the cilium is observed has a lower profile during the forward stroke while its profile in the backward stroke tends to be higher.

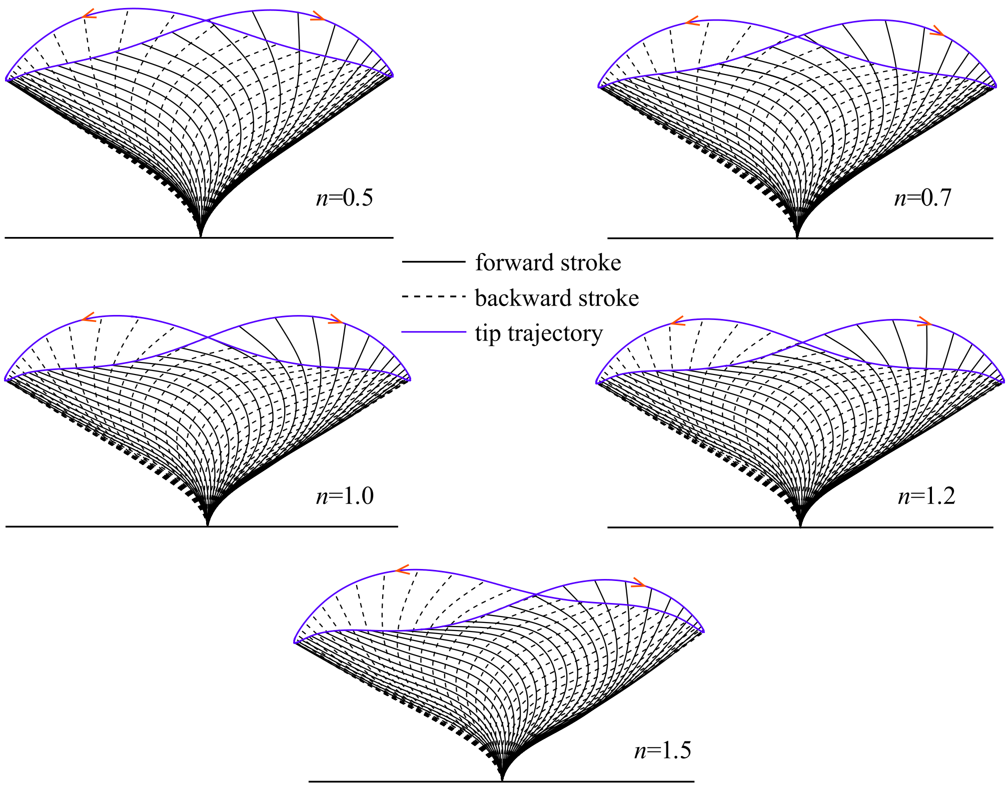

Fig. 5.2 Superpositions of the cilium profile for various $n$

Fig. 5.3a shows the time evolutions of the scaled tip deflection at three different *n* (for clarity purpose, we only show three typical cases though our simulations covered five cases), where only a very limited difference in the phase and amplitude can be observed among them. Fig. 5.3b shows the temporal fluctuations of the TAS. An increase in the *n* leads to a decrease in the maximal TAS. The time evolutions of the maximal curvature and MTS location (scaled) for various *n* are presented in Fig. 5.4a and b, respectively. The maximal curvature is found to increase as *n* increases. This increase is more significant when the fluid is shear thinning (i.e., $n<1$). Relocation of the MTS can be observed in all the simulated cases, while the maximal propagation distances for the three *n* have no significant difference. Due to the asymmetric flapping pattern occurs in the case of $n=1.5$, the MTS location varies differently between the forward and backward strokes.

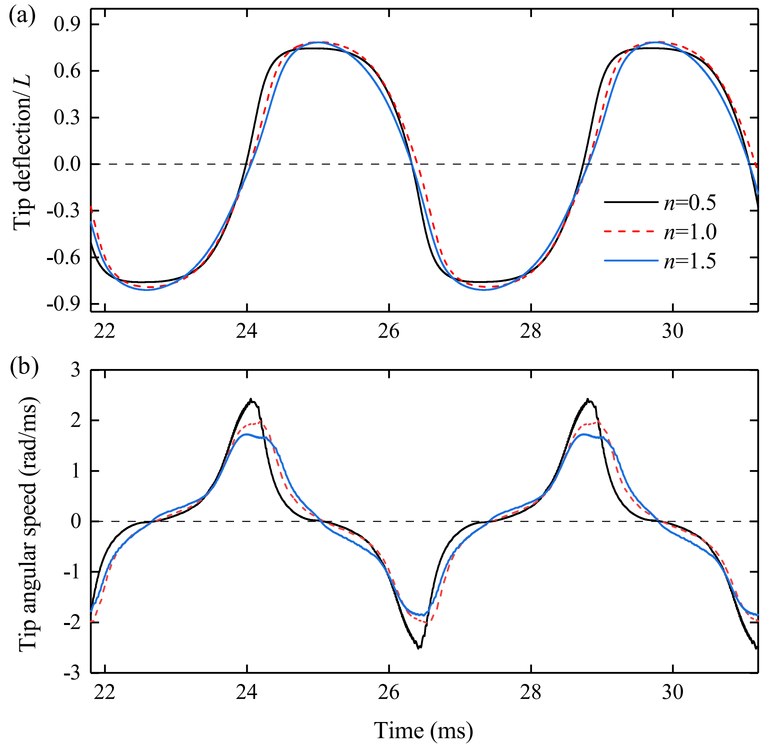

Fig. 5.3 Time evolutions of the scaled tip deflection (a) and TAS (b) for various *n*

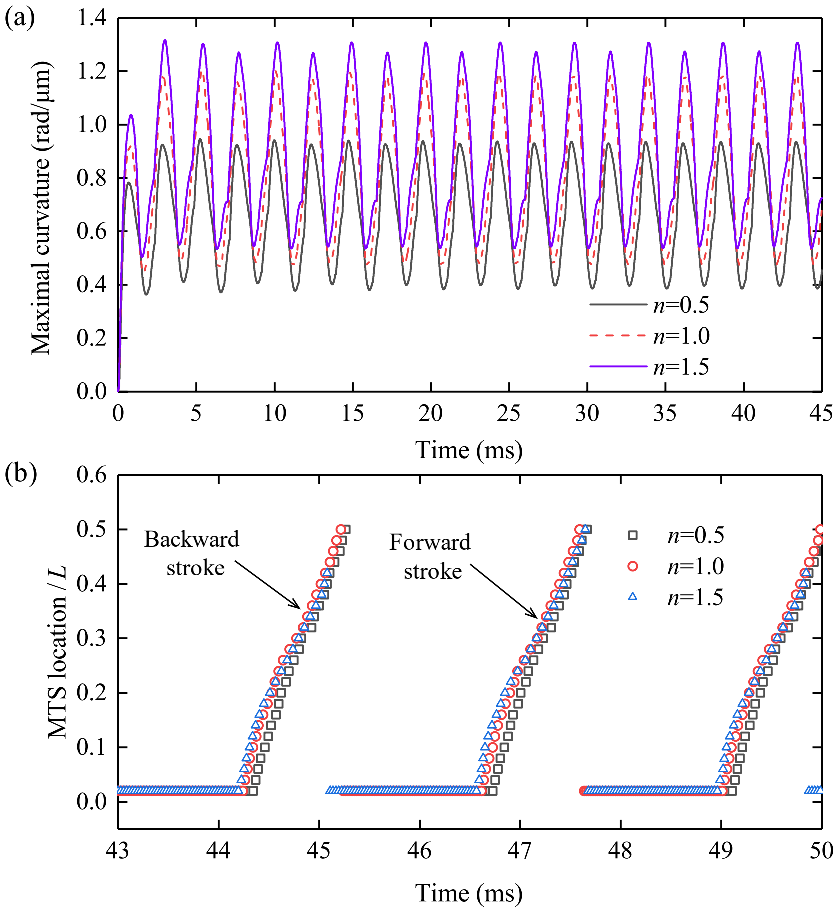

Fig. 5.4 Time evolutions of the maximal curvature (a) and scaled MTS location (b) for various *n*

The flow patterns captured in a forward stroke for various *n* are shown in Fig. 5.5. No significant difference in the flow structure is observable among the three cases. For all the three chosen *n* values, recirculation regions can be observed when the cilium is about to reach its deflection limit. Fig. 5.6 shows the snapshots of the u-velocity contour (scaled by the maximal u-velocity at the current timestep) for various *n*. As *n* increases, the shear effect between the fluid and the cilium becomes more significant, and as a result, a greater portion of fluid seems to attach to the cilium surface, causing a lower velocity region around the cilium. Apart from that, as cilium deflects, the mixing between adjacent fluid layers is also more remarkable in the case of $n$=0.5.

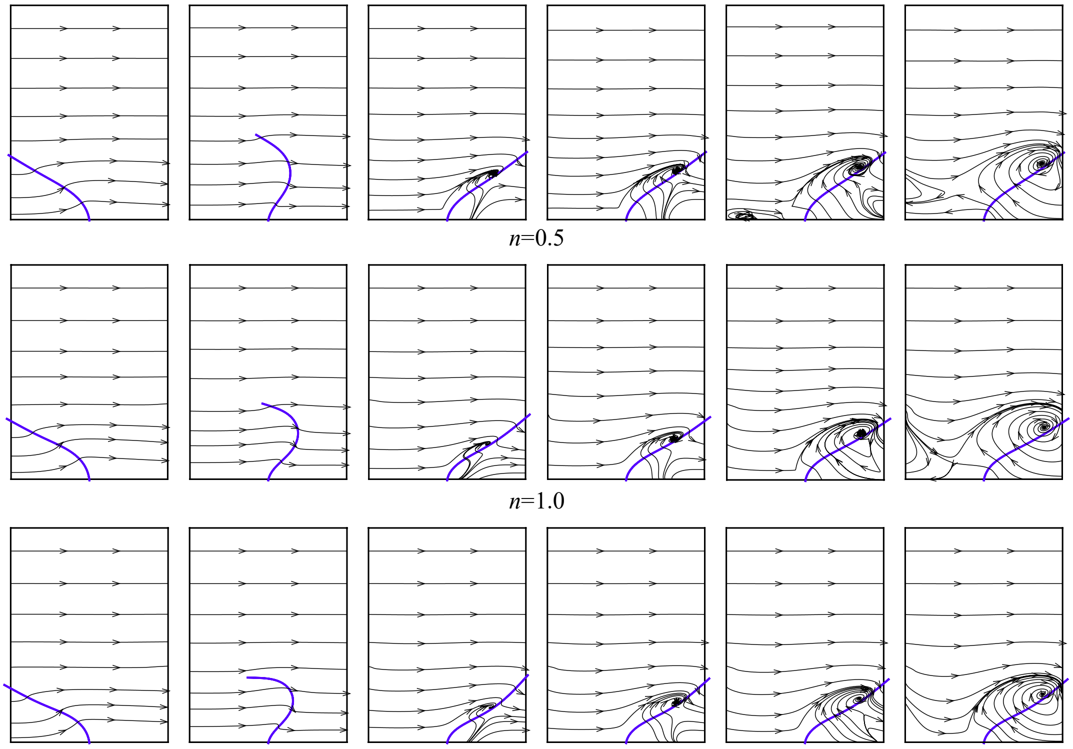

$n$=0.5

$n$=1.0

$n$=1.5

Fig. 5.5 Flow patterns captured in a forward stroke for various $n$

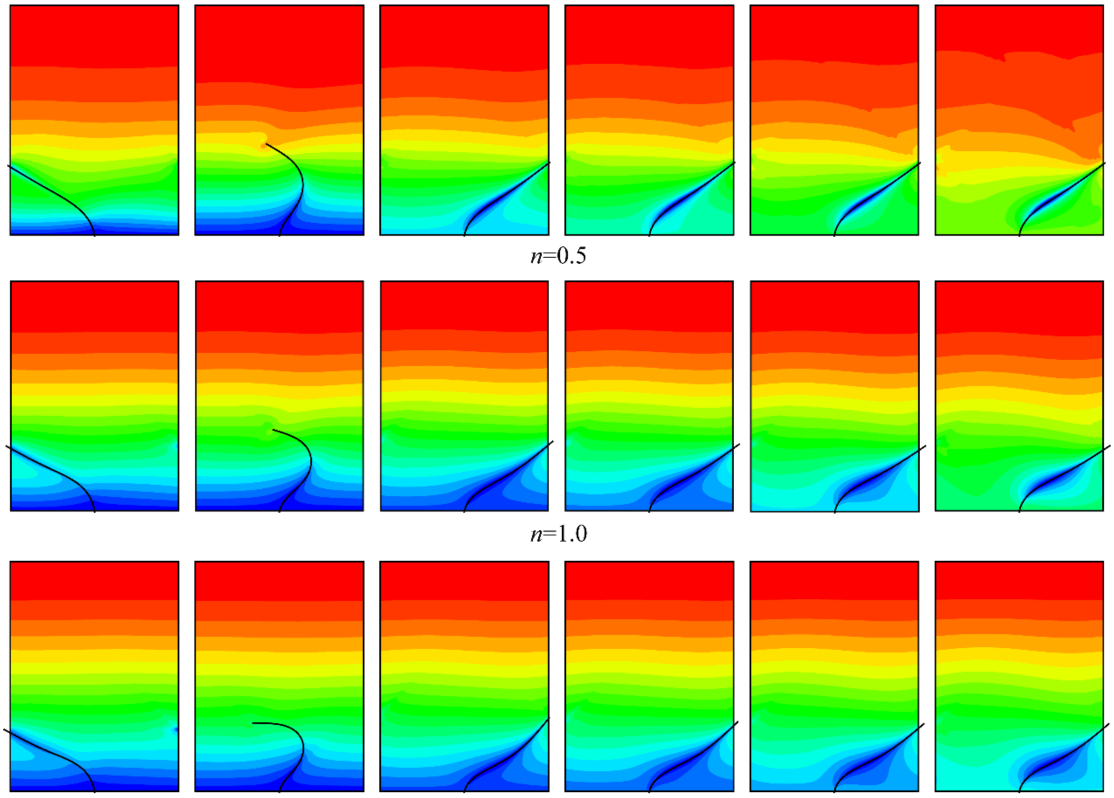

*n*=0.5

*n*=1.0

*n*=1.5

Fig. 5.6 Snapshots of the scaled u-velocity contour for various *n*

Fig. 5.7a presents the time evolutions of the average WSS in the cases with and without cilia for various *n*. Compared with the corresponding without-cilia cases, a decrease in the average WSS can be observed for all simulated *n* with cilia presented. Fig. 5.7b plots the time-averaged decrease in the average WSS due to the presence of cilia. Compared with the Newtonian fluid case (i.e., $n$=1.0), the decrease is more dramatic for a shear-thinning fluid (i.e., $n$<1) while less obvious for shear-thickening fluid. As a kind of non-Newtonian fluid, the blood flow exhibits shear-thinning characteristics. Simply modelling the blood flow as a Newtonian fluid thus underestimates cilium's impact on the WSS. From the figure, it is found that the maximal decrease is obtained in the case of $n$=0.7, at a percentage of 24.3%. When

$n>0.7$, the percentage is found to drop almost linearly with $n$. Fig. 5.8 presents the OSI distributions for three different $n$. Increasing the $n$ brings a larger affected area (the area with OSI value less than 0.5) with smaller OSI value. Due to the cilium's asymmetric flapping in the case $n=1.5$, its corresponding OSI distributions is also found to be asymmetric.

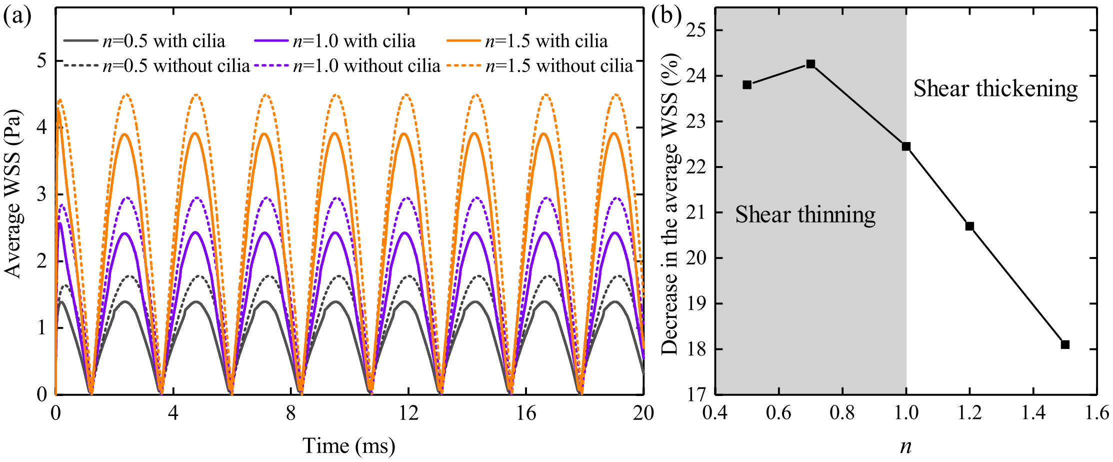

Fig. 5.7 Time evolutions of the average WSS in cases with and without cilia for various $n$ (a) decrease in the average WSS due to the presence of cilia for various $n$ (b)

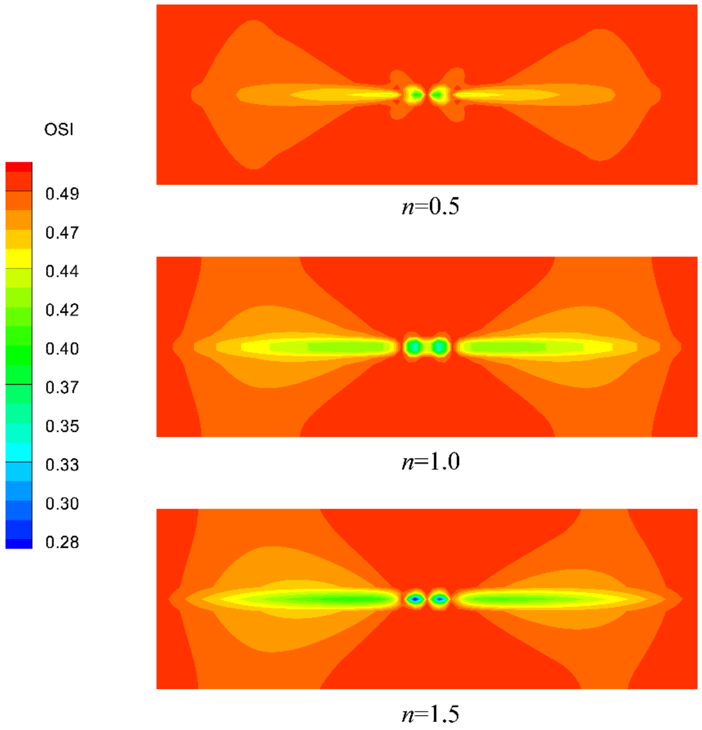

Fig. 5.8 OSI distributions for three different *n*

## 5.5 Summary

In this chapter, we implemented the power-law model into our IB-LBM algorithm to study cilium dynamics in oscillating no-Newtonian fluid. By varying the power-law index *n* from 0.5 to 1.5, we studied and compared the cilium dynamics in shear-thinning, Newtonian, and shear-thickening fluid. Our numerical simulations suggest that:

(1). The symmetry in flapping is found to be broken when *n*=1.5. In that case, a sensory failure may occur as the primary cilium fails to capture the symmetry of the input pressure signal via its passive deflection.

(2). No significant difference in the flow structure is observable for different *n* values. However, as *n* increases, a greater portion of fluid seems to attach to the cilium surface due to the increased shear effect and a larger affected area with smaller OSI value can be observed in the OSI distribution.

(3). The decrease in average WSS is most significant for shear-thinning fluid, then followed by Newtonian fluid. The shear-thickening fluid causes the least decrease in the average WSS. Modelling a shear-thinning fluid as Newtonian thus underestimates cilium's impact on the WSS while modelling a shear-thickening fluid as Newtonian will overestimate such impact.

# Chapter 6 The adhesion of a circulating tumor cell in a curved microvessel

## 6.1 Physical model and simulation setup

The geometry of the curved vessel is shown in Fig. 6.1, which is the three-dimensional version of the one used by Yan et al. [73]. Another improvement of our model over the one in Yan et al. [73] is that the elasticity of the cell membrane is considered. Both the blood plasma and cytoplasm are modeled as DPD fluid of the same property. The curved part of the microvessel is consisted of three bends and the vessel geometry is bilaterally symmetric, as shown in Fig. 6.1. The origin of the coordinate system locates at point O. A spherical CTC of diameter $d_{\mathrm{c}}$ is released at a vertical position $H_0$ in the straight section of the vessel. A constant azimuthal body force density $\boldsymbol{f}_{\mathrm{d}}$ is applied to all DPD particles to produce a pressure gradient to drive the fluid. The flow is assumed periodic in the y-direction, and the vessel wall is rigid, impermeable and imposed with a no-slip condition. The basic parameters used in our simulations are tabulated in Table 6.1, where a length scaling factor $C_{\mathrm{l}} = 1 \times 10^{-6}\mathrm{m}$, a viscosity scaling factor $C_{\mu} = 5.1 \times 10^{-5}\mathrm{Pa} \cdot \mathrm{s}$, and an energy scaling factor $C_{\mathrm{e}} = 4.28 \times 10^{-21}\mathrm{J}$ are used for unit conversion. The simulation is based on our in-house code which has been well validated in our previous research [170-172].

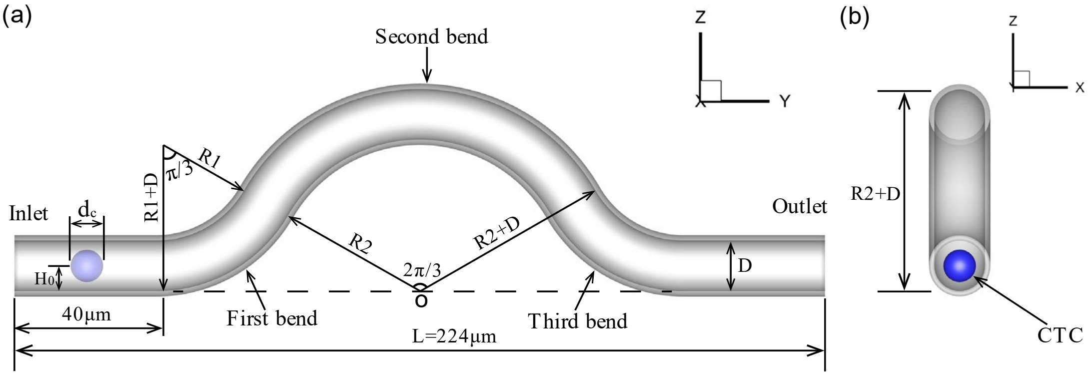

Fig. 6.1Geometry of the curved microvessel (a) front view (b) side view

Table 6.1 Basic parameters used in our simulations

| Parameters | Physical value | Simulation input |
|---|---|---|
| CTC diameter ($d_c$) | 9μm | 9 |
| Vessel diameter ($D$) | 14μm | 14 |
| $R1$ | 28μm | 28 |
| $R2$ | 42μm | 42 |
| Initial vertical position ($H_0$) | 7μm | 7 |
| Blood plasma viscosity ($\mu$) | $1.2 \times 10^{-3}\mathrm{Pa \cdot s}$ [173] | 1.43 |
| $k_BT$ ($T = 310\mathrm{K}$) | $4.28 \times 10^{-21}\mathrm{J}$ | 1 |
| Driven force density ($f$) | $1.284 \times 10^{5}\mathrm{N/m^3}$ | 30 |
| Membrane bending modulus ($K_b$) | $3.6 \times 10^{-18}\mathrm{J}$ [151] | 841.12 |
| Global area constraint constant ($K_{area}^{tot}$) | $3.35 \times 10^{-3}\mathrm{N/m}$ [68] | $7.83 \times 10^{5}$ |
| Local area constraint constant ($K_{\mathrm{area}}$) | $5.2 \times 10^{-6}\mathrm{N/m}$ [68] | $1.21 \times 10^{3}$ |
| Volume constraint constant ($K_{volume}$) | $3.35 \times 10^{-3}\mathrm{N/m}$ [68] | $7.83 \times 10^{5}$ |
| Unstressed on rate ($k_{\mathrm{on}}^0$) | $1 \times 10^{4}\mathrm{s}^{-1}$ [174] | 1960 |
| Unstressed off rate ($k_{\mathrm{off}}^0$) | $20s^{-1}$ [175] | 3.92 |

| | | |
|---|---|---|
| Effective on strength ($\sigma_{\mathrm{on}}$) | $5 \times 10^{-7}\mathrm{N/m}$ [176] | 116.82 |
| Effective off strength ($\sigma_{\mathrm{off}}$) | $5 \times 10^{-8}\mathrm{N/m}$ [176] | 11.68 |
| Association distance ($d_{\mathrm{on}}$) | 0.1μm | 0.1 |
| Disassociation distance ($d_{\mathrm{off}}$) | 0.1μm | 0.1 |
| Spring constant ($K_s$) | $2 \times 10^{-3}\mathrm{N/m}$ [177] | $4.67 \times 10^5$ |
| Equilibrium spring length ($l_b^0$) | 0.025μm [176] | 0.025 |
| Receptor density ($n_r$) | $4.63/\mu\mathrm{m}^2$ | 4.63 |
| Ligand density ($n_l$) | $1.73/\mu\mathrm{m}^2$ | 1.73 |
| Timestep (Δt) | $4.9 \times 10^{-5}\mathrm{s}$ | $2.5 \times 10^{-4}$ |
| Cut off radius ($r_{\mathrm{c}}$) | 1.0μm | 1.0 |

## 6.2 CTC adhesion in straight and curved vessels

A comparative study is first performed by simulating the adhesion of a CTC respectively in a curved and a straight vessel. Despite the curvatures, all the other parameters are kept identical between these two vessels (i.e., the CTC needs to travel the same distance to reach the vessel outlet). The evolutions of the CTC in the two vessels are presented in Fig. 6.2a and b, respectively, where the cell-wall contact areas are highlighted. A deformation in the CTC can be observed in both two vessels as the CTC migrates to the downstream of the vessels. In the curved-vessel case, the CTC is found to contact the wall for several times during its migration. However, the contact happens for only once in the straight-vessel case. The increased contacts in the curved vessel case may be caused by the centrifugal effect as the CTC is found to move outwards, away from the center of curvature. Fig. 6.2c demonstrates a typical unsuccessful adhesion in the curved vessel. The cell membrane is flattened once it has a direct contact with the vessel inner wall. This then leads to in an increase in the contact surface area, which further promotes bond formation as more receptors will fall into the reactive distance $d_{\mathrm{on}}$ of the ligands which localize to the endothelium. The adhesive spring force from those bonds will drag the CTC and stop it from escaping that site (i.e., cell arrest). The anti-adhesive force (e.g., the hydrodynamic force and the reaction force from the wall), on the contrary, suppresses the cell from getting arrest. A successful cell arrest this depends on the competition between the anti-adhesive and adhesive forces. Once the anti-adhesive force wins (just like the simulated case here), the adhesion fails and the CTC can migrate forward. When the cell is trying to escape from the wall's arrest, a spike is formed due to the adhesive drag force. The anti-adhesive force will eventually rupture all the formed bonds and the CTC will recover to a more spherical shape.

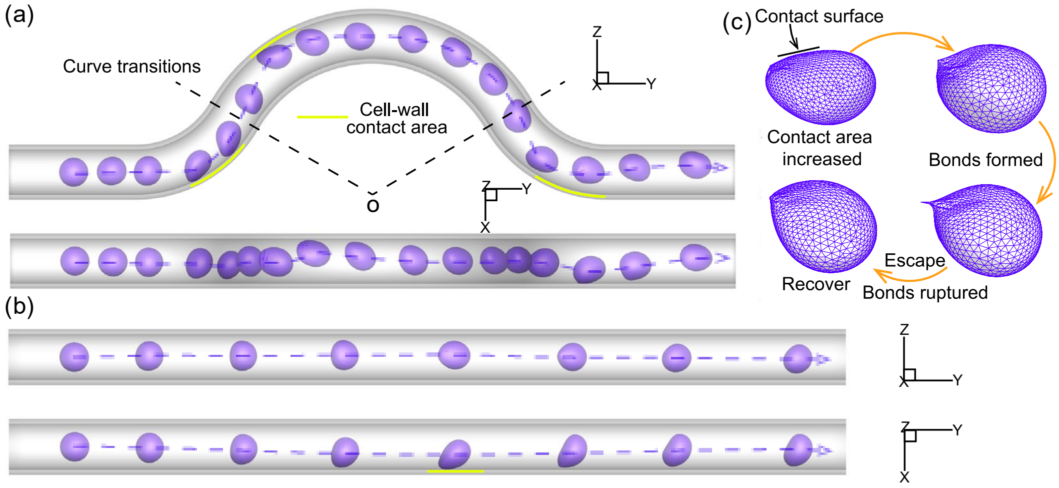

Fig. 6.2 The evolution of the CTC in a curved vessel (a) and in a straight vessel (b). A typical unsuccessful adhesion process captured in the curved-vessel case (c).

The trajectories of the CTC (represented by the cell center) in the curved and straight vessels are plotted in Fig. 6.3a and b, respectively. The CTC's trajectory is found to be three-dimensional and it deviates from the vessel axis. Compared with the straight-vessel case, a greater deviation in the CTC trajectory is observed for the curved-vessel case possibly due to the centrifugal effect. The deviation increases bond formations, as it makes more receptors fall into the effective range of the ligands. Once a bond is formed, the adhesive force will further pull the CTC toward the vessel wall and makes a possible cell-wall contacts. This explains why cell-wall contacts happens in our low-*Re* flow case, where the viscous effect dominates the fluid motion.

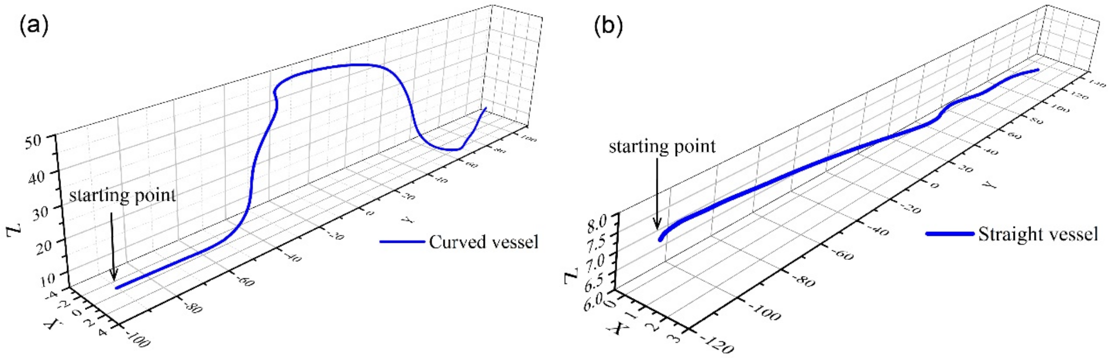

Fig. 6.3 Trajectories of the center of CTC in the curved (a) and straight (b) vessels

Fig. 6.4a shows the how the velocity magnitude of the CTC varies with time, where the CTC's vertical position (dash-dot-dash line) in the curved vessel is also appended to indicate its transient location. We can see that the CTC migrates faster in the straight vessel as the time needed to migrate over the entire length of the vessel nearly gets halved compared to that in the curved vessel. The velocity magnitude shows an increasing trend at the beginning for both cases. However, in the curved-vessel case, the velocity magnitude starts to fluctuate after the CTC enters the first vessel bend. On the contrary, the CTC in the straight vessel is found to accelerate throughout the journey, though a short fluctuation is still observable in the middle of the migration possibly due to the cell-wall contact. Fig. 6.4c-d show the time evolutions of the bond number in the two vessels. In the curved-vessel case, intensive bond formations are observed at three different sites with a maximum bond number of 7. However, no bonds are formed during the migration of CTC in the straight vessel, suggesting that the curvature of the vessel greatly affects the CTC adhesion. Interestingly, bond formations occur more frequently around those curve transition regions (the regions where vessel curvature is varying), where cell-wall contacts are also more prevalent (see Fig. 6.2a). Fig. 6.4b plots the probability to form bonds at a specified number during the migration. The probability of bond formation seems to be low (<10%) even for the curved-vessel case, it is a significant improvement over the straight-vessel case, in which we have observed no bond formations at all. Since the probability of the bond formation also depends on the receptor and ligand densities, for the densities chosen in the current study, it is at the low end, which may reflect the real situation that the arrest and adhesion of the CTCs do not happen frequently.

The time evolutions of CTC's volume and surface area are shown in Fig. 6.5a and b, respectively. A shrinkage in the volume while a slight expansion in the surface area (less than 6%, for we use a large $K_{area}^{tot}$ in our simulations) are observed when the CTC contacts the wall. That explains those sudden changes observed in Fig. 6.5a and b. The shrinkage in the cell volume tends to decrease the flow resistance, while the expansion in the surface area leads to a more complete contact. Both changes are favorable to a successful cell adhesion.

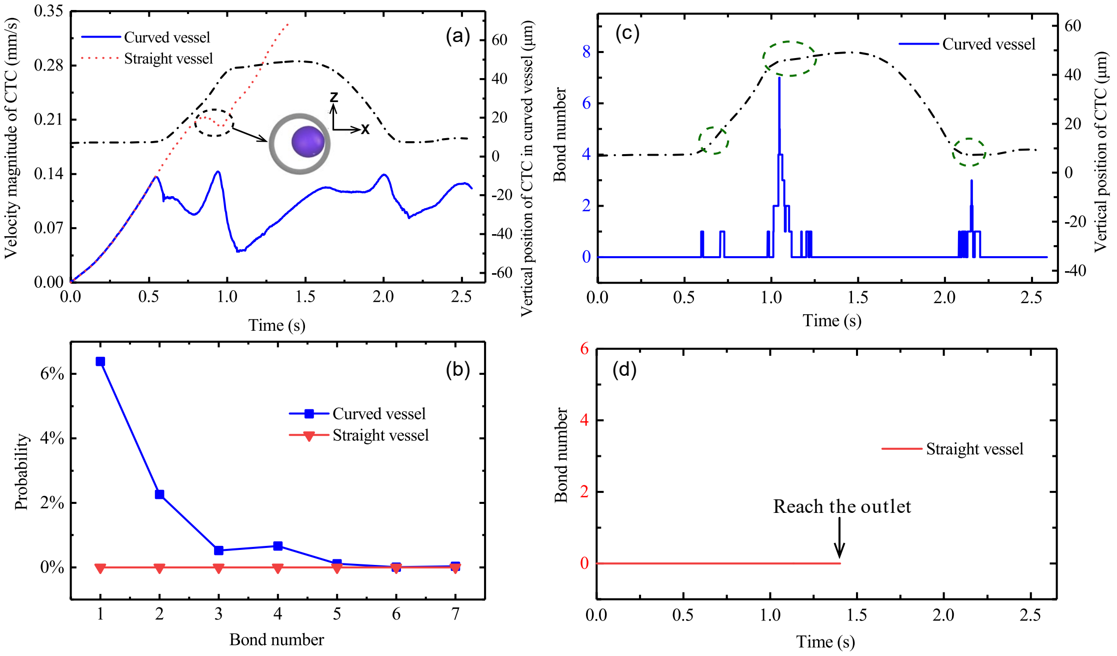

Fig. 6.4 The time evolutions of the velocity magnitude of a CTC (a), the probability to form bonds at a specified number (b), and the number of bonds formed in the curved (c) and straight (d) vessels. The dash-dot-dash line in (a) and (c) represents the vertical position of the CTC with the scale shown at the right axis.

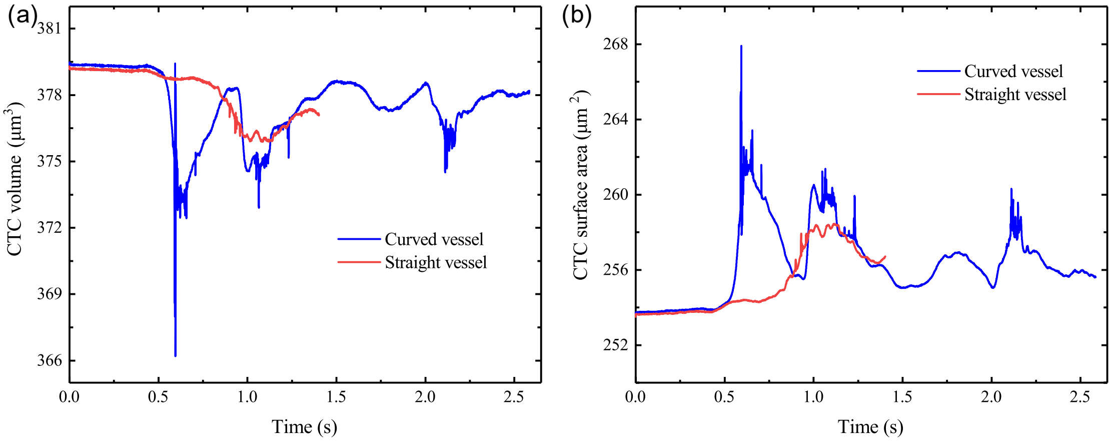

Fig. 6.5 The time evolution of the volume (a) and surface area (b) of CTC in the curved and straight vessels

## 6.3 Effect of the driven force density

The effect of the flow *Re* on the cell dynamics and adhesion is investigated by varying the applied driven force density *f*. Three different *f* values are chosen (e.g., *f*=15, 30, and 45, respectively). Fig. 6.6a-c show how the bond number varies with the time in the three cases. The probability to form bonds at a specified number is presented in Fig. 6.6d. An increase in the average bond number and bond formation probability is observable as the *Re* increases. In the case of *f*=15, bond formation can be found in two sites of the vessel and the maximum and average bond number are 3 and 0.0658, respectively. As *f* increases to 30, bond formation can be found in three sites and the average and maximum bond number become 0.159 and 7, respectively. The average bond number reaches to 0.191, as the applied *f* further increases to a value of 45. Apart from that, the cell is found to form bonds in four different sites, even in the downstream straight section of the vessel. This is an anticipated result. When a larger value of *f* is applied, the velocity magnitude of the CTC will get increased (see Fig. 6.6e), which brings a larger centrifugal force. As a result, the trajectory of the CTC will deviate more from the vessel axis, which tends to increase cell-wall contacts. However, it should be noted that an increase in the bond number may not necessarily enhance the cell adhesion possibility, as the increase of *f* also brings a larger hydrodynamic force (part of the anti-adhesive force) that prevents the adhesion of the CTC. From Fig. 7a-c, one can also observe a shift of the hotspot for bond formation. In the case of *f*=15, the most active site (hotspot) for bond formation locates at the first bend of the vessel. However, as the value of *f* increase to 30, the hotspot is found at the left half of the second bend of the vessel, even at the third bend.

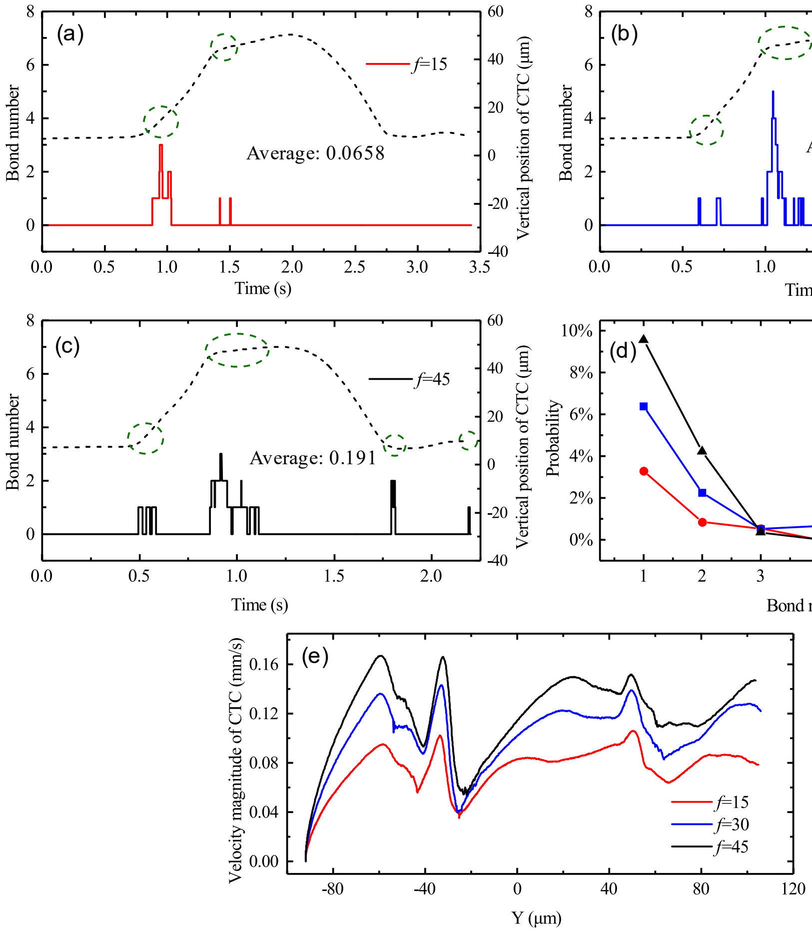

Fig. 6.6 The time evolutions of the bond number at f=15 (a), f=30 (b) and f=45 (c), the probability to form bonds at a specified number (d) and the velocity magnitude of a CTC as a function of the y-coordinate of the cell center (e). The short-dashed line in (a-c) represents the vertical position of the CTC with the scale shown at the right axis.

## 6.4 Effect of the membrane bending modulus

The migration of a softer CTC ($K_b = 500$) is simulated at *f*=15 in this section. The results will be compared with that of the prior case ($K_b = 841.12$) to explore the effect of the membrane bending modulus $K_b$ on CTC adhesion. Fig. 6.7a shows the time evolutions of the cell's velocity magnitude, where two curves are found to get nearly overlapped. Thus, the $K_b$ will not greatly affect the velocity magnitude of CTC. However, the $K_b$ of the CTC is found to closely related to the cell adhesion, as can be seen from Fig. 6.7c-d. When the $K_b$ of CTC reduced from 841.12 to 500, the average bond number increases nearly by 104%, from 0.0658 to 0.134. Fig. 6.8a shows the probability to form bonds at a specified number in the two cases. The probability is found to increase significantly when the value of $K_b$ decreases from 841.12 to 500, indicating that a softer CTC tends to be more adhesive during its migration in a curved microvessel. Fig. 6.7b shows the time evolution of the CTC surface area. A cell-wall contact will induce a leap in the surface area of CTC, which is severer for a softer CTC. The leap in the surface area makes the cell contact the wall more comprehensively (see Fig. 6.8b). Apart from that, that bonds form intensively at four sites of the vessel in the softer-CTC case while only two sites are found in the stiffer-CTC case (see Fig. 6.7c-d). Furthermore, the hotspot for bond formation is found to shift to the left half of the second bend of the vessel.

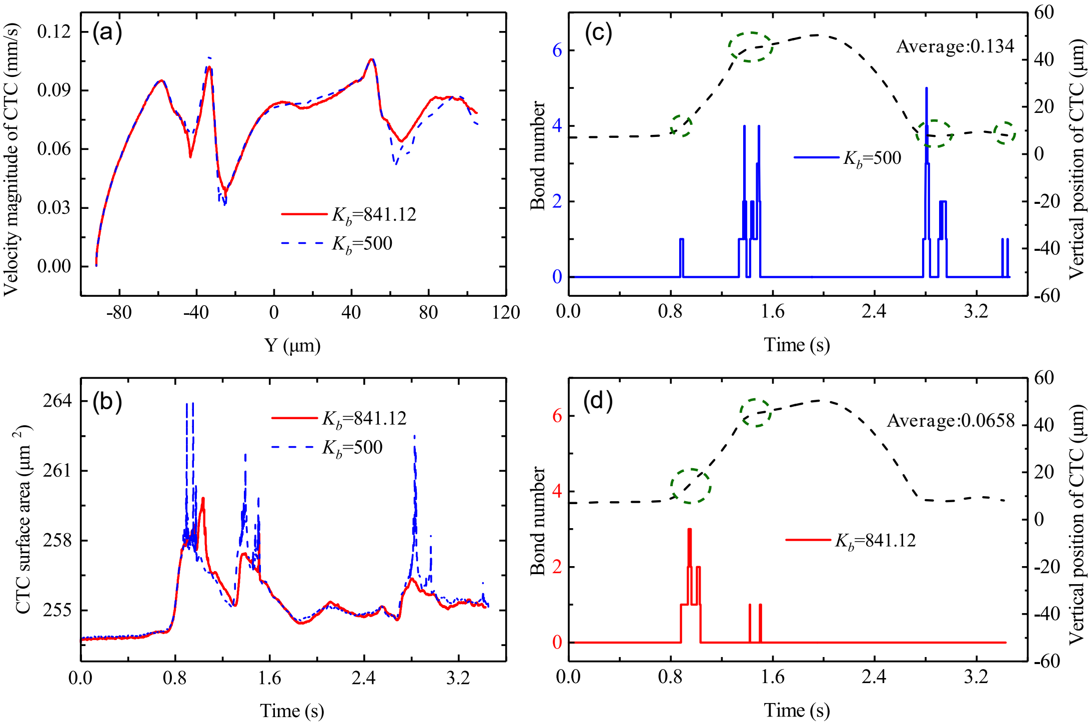

Fig. 6.7 The velocity magnitude of CTC as a function of the y-coordinate of the cell center (a), and the time evolution of the CTC surface area (b), and the number of bonds formed when $K_b = 500$ (c) and $K_b = 841.12$ (d). The dashed line in (c-d) represents the vertical position of the CTC with the scale shown at the right axis.

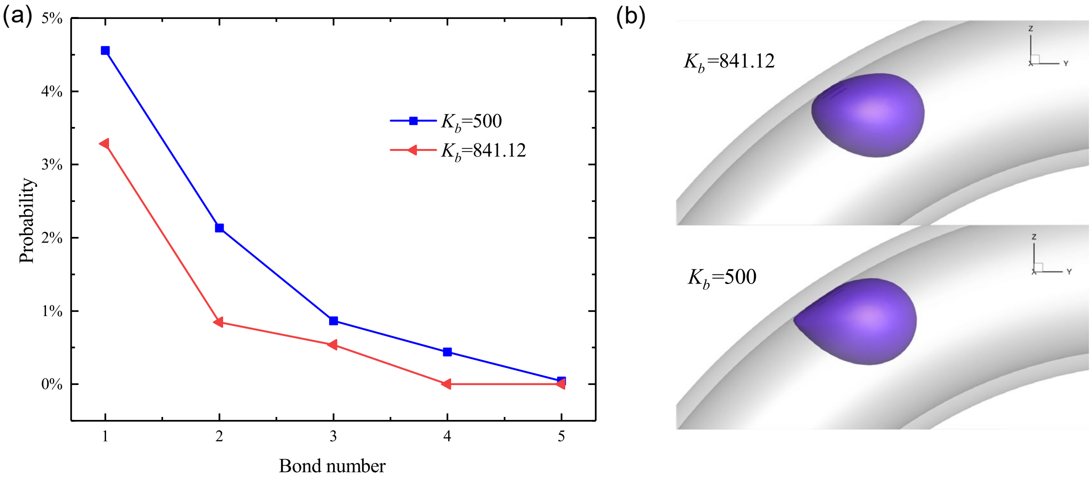

Fig. 6.8 The probability to form bonds at a specified number (a) and a comparison of the cell-wall contact at the second bend of the vessel with each snapshot taken when a

full-contact happens (b)

## 6.5 Summary

In this chapter, the adhesion of a CTC in a curved microvessel is numerical investigated. The DPD is used to solve the flow dynamics, the membrane of the CTC is modelled with the spring-based network, and the adhesion behavior is solved by the probabilistic adhesion model. A comparative study is performed to characterize the differences between the adhesion of CTC in straight and curved vessels. After that, a parametric study is performed to investigate the effect of the $Re$ and membrane bending modulus $K_b$ on CTC adhesion. Our simulation results suggests that:

(1). It's easier for a CTC to get adhered in a curved vessel as the centrifugal effect cause a deviation of the cell trajectory and increases bond formations. Compared to that in the straight vessel, the velocity magnitude of the CTC tends to be lower and more fluctuant in the curved vessel due to the increased cell-wall contact.

(2). In the curved-vessel case, an increase in the $Re$ or a decrease in the $K_b$ could promote the formation of bond and outspread the bond formation sites. The former brings a larger centrifugal force while the latter increases the contact surface area in a cell-wall contact. In addition, the most active site for bond formations in the curved vessel is found to vary with the $Re$ and the $K_b$. For the curved vessel considered, the most active site for bond formation locates at the first bend of the vessel when the $Re$ is relatively low. However, as $Re$ increases or $K_b$ decreases, the site is found to shift to the left half of the second bend of the vessel.

# Chapter 7 Conclusions and future works

## 7.1 Conclusions

This thesis explores the FSI arising in the flow sensing and cell adhesion problems. The thesis is mainly presented in two parts. The first part concerns the modelling of the dynamics of primary cilia in an oscillating flow. The two-way FSI is solved by the IB-LBM, and the primary cilium is modelled as a slender filament whose basal end is attached to a nonlinear rotational spring. In this way, the basal rotation of primary cilium can be well considered. After being well validated, the developed algorithm is used to study the dynamics of a 3D cilia array in an oscillating Newtonian flow. A parametric study covering the $Re_{peak}$, the $Wo$, the cilium length, and the spacing interval, is also performed to investigate how these parameters affect the flow-cilia interaction. Based on our simulation results, the following conclusions can be drawn.

(1). The primary cilia are observed to do an in-plane flapping motion which is symmetrical in term of the cilium profile. Among all the simulated cases, three typical stretch states are captured. In the first stretch state, the direction of the profile curvature does not vary along the cilium length, making one side of the ciliary membrane under stretch while the other under compression throughout the cilium length. In the second stretch state, the direction of the profile curvature is found to vary once along the cilium length. As a result, each side of the ciliary membrane will be partially under stretch and partially under compression. The third stretch state is observed for a long cilium that extends into 1/3 of the lumen. In this state, the cilium's profile is found to vary twice in the curvature direction. In that case, the base, middle and tip sections of the cilium will be under stress sates different from their neighbors'.

(2). The MTS location may not always stay at the cilium's base region, instead it is found to periodically propagate from the cilium's base point to its tip by a certain distance. For primary cilia with short and medium length, an increase in the maximal tip deflection is accompanied with a greater propagation distance. While this may not necessarily apply to long primary cilia, as the possible occurrence of the third stretch state may greatly suppress the propagation of the MTS location.

(3). The flow-induced curvature at the lower part of the primary cilium is well synchronized with the applied pressure signal, while an obvious phase lag in the curvature is observed for the rest parts of the cilium. A smaller phase lag means a fast respond speed and less delay. Therefore, it would be reasonable to speculate that the lower part of primary cilia may be most responsible for detecting the variations of the flow information.

(4). The presence of primary cilia slows down the velocity in the near-wall region and decreases the average WSS level. Under the same flow condition, the decrease is found to be more significant when a cilium undergoes a larger span of deflection and/or when the spacing interval is reduced. Compared with the spacing interval, the span of deflection plays a marginal role in decreasing WSS. The presence of primary cilia is also found to affect the oscillation characteristic of the WSS by making the WSS in some regions less oscillatory.

(5). For the ranges of parameters considered, an increase in the $Re_{peak}$ or cilium length is found to bring a larger span of cilium deflection and maximal curvature. An increase in the *Wo*, however, is found to decrease these two quantities. For a constant spacing interval, a larger span of deflection is found to correspond to a more uneven OSI distribution.

(6). In a cilia array, neighboring cilia interact with each other via surrounding fluid. The interacting becomes weaker as the spacing interval increases. A sparser cilia arrangement therefore tends to have a larger span of cilium deflection, maximal curvature, and propagation distance of the MTS location. For a medium $Re_{peak}$ and *Wo*, our simulation suggests that a spacing interval greater than twice the cilium length could effectively reduce the interference from the neighboring cilia thus improves the sensing accuracy of primary cilia. This could be the reason why there is only one primary cilium at most for each endothelial or epithelial cell whose diameter happens to be about 2-3 times the length of primary cilium.

The developed model is further extended to study cilium dynamics in oscillating no-Newtonian fluids with the power-law model. The simulation result suggests that:

(1). The symmetry in flapping is found to be broken when $n$=1.5. In that case, a sensory failure may occur as the primary cilium fails to capture the symmetry of the input pressure signal via its passive deflection.

(2). No significant difference in the flow structure is observable for different $n$ values. However, as $n$ increases, a greater portion of fluid seems to attach to the cilium surface due to the increased shear effect and a larger affected area with smaller OSI value can be observed in the OSI distribution.

(3). The decrease in average WSS is most significant for shear-thinning fluid, then followed by Newtonian fluid. The shear-thickening fluid causes the least decrease in the average WSS. Modelling a shear-thinning fluid as Newtonian thus underestimates cilium's impact on the WSS while modelling a shear-thickening fluid as Newtonian will overestimate such impact.

The second part of the thesis focus on the simulation of CTC adhesion in a curved microvessel. The flow dynamics is solved by the DPD, the membrane of the CTC is modelled with the spring-based network, and the adhesion behavior is solved by the probabilistic adhesion model. A comparative study is performed to characterize the differences between the adhesion of CTC in straight and curved vessels. After that, a parametric study is performed to investigate the effect of the $Re$ and membrane bending modulus $K_b$ on CTC adhesion. Our simulation resultson this problem suggests that:

(1). It's easier for a CTC to get adhered in a curved vessel as the centrifugal effect cause a deviation of the cell trajectory and increases bond formations. Compared to that in the straight vessel, the velocity magnitude of the CTC tends to be lower and more fluctuant in the curved vessel due to the increased cell-wall contact.

(2). In the curved-vessel case, an increase in the $Re$ or a decrease in the $K_b$ could promote the formation of bond and outspread the bond formation sites. The former brings a larger centrifugal force while the latter increases the contact surface area in a cell-wall contact. In addition, the most active site for bond formations in the curved vessel is found to vary with the $Re$ and the $K_b$. For the curved vessel considered, the most active site for bond formation locates at the first bend of the vessel when the $Re$

is relatively low. However, as $Re$ increases or $K_b$ decreases, the site is found to shift to the left half of the second bend of the vessel.

## 7.2 Future work

### 7.2.1 For the flow sensing of primary cilia

We are aware that our current simulations are rather simplified compared to the in vivo cilium deflection cases. The endothelial primary cilium in vivo may also be subjected to other hemodynamic forces (e.g., the force due to cell-cilium collisions), and physical constraints imposed by the glycocalyx layer and organic constraints when in blood vessels.

(1). Therefore, a possible future improvement over our current model is to include the effect of the glycocalyx layer (a layer made of proteoglycans and glycoproteins serving as a mechano-sensor for WSS [178]) on the cilium deflection. This requires us to treat the fluid as two immiscible layers and use a proper multiphase and multicomponent model, such as the popular Shan-Chen model [75] and free-energy model [179] for LB modelling.

(2). Our current model can also be improved by considering the interaction between the cells (red blood cells (RBCs) and leukocytes) and the primary cilia. Such interaction is expected in micro-vessels where the blood flow should be treated as a suspension of RBCs (in large size vessels, such as arteries, the cell-cilium collisions are less unlikely duo to that the RBCs tend to flow to the center of the vessels, forming a cell free layer near the vessel wall [180]).

(3). The primary cilia are found to be prevalent in the arterial bifurcations and the inner curvature of arched arteries, where the flow is low and disturbed [181]. The future studies thus can focus on the cilium dynamics in these sites. This means we should use more realistic vessel geometries, such as cylindrical, curved and even bifurcated vessel shapes. In a curved vessel, the centrifugal effect may give rise to a secondary flow (known as Dean vortices), which may induce out-of-plane cilium motions. In the vessel bifurcation regions, the vortical flow structures could make the flow more distributed and complicated. It would be interesting to find out the cilium dynamics in these sites and its impact on the WSS distribution there.

(4). We currently use a MPI and OpenMP parallel computation strategy to speed up our simulations. They work well for our current small-scale simulations, however, may be not efficient for large-scale simulations that involve several tens even hundreds of primary cilia. Future studies thus can integrate in and takes the advantage of the GPU parallel computing, which can significantly improve the computational efficiency.

### 7.2.2 For cell adhesion problem

The present study is an initial step towards the investigation on CTC adhesion in real microvasculature with complicated geometric patterns. We list here some possible future studies that will follow the research described in the current study.

(1). One is to explore the influence of the circulating blood cells on the CTC adhesion. As blood is a concentrated suspension of a variety of cells, the blood cells (e.g., RBCs, leukocytes, and platelets) certainly should play an important role in the migration and adhesion of CTCs.

(2). A few studies have observed clusters of the CTCs in the circulation [182, 183]. How will the CTC clusters respond in a curved vessel? Will the CTC clusters promote or inhibit CTC adhesion compared to the single-cell case? Further studies are required to answer these questions.

(3). Most tumor cells have their specific metastatic organs, for instance, colon cancer preferentially metastasizes to the liver [184], and the receptors-ligands bond can be activated by both mechanical (e.g., blood flow) and chemical (e.g., cytokines) stimuli [71, 185, 186]. Therefore, it is necessary to develop a model with spatial-temporal distributions of the receptors and ligands, and varied bond formation kinetics, to reflect the local mechanochemical factors in the specific organ on the CTC adhesion and transmigration.

(4). The impact of some other relevant factors on CTC adhesion is also worth investigating, e.g., other vessel geometry types (e.g., bifurcated vessels) and the initial position of the CTC.

# References

[1] Hagiwara, H, Ohwada, N, Aoki, T, Suzuki, T, Takata, K. The primary cilia of secretory cells in the human oviduct mucosa, Medical Molecular Morphology. 41 (2008) 193-8.

[2] Nguyen, AM, Jacobs, CR. Emerging role of primary cilia as mechanosensors in osteocytes, Bone. 54 (2013) 196-204.

[3] Davenport, JR, Yoder, BK. An incredible decade for the primary cilium: a look at a once-forgotten organelle, Am J Physiol Renal Physiol. 289 (2005) F1159.

[4] Singla, V, Reiter, JF. The Primary Cilium as the Cell's Antenna: Signaling at a Sensory Organelle, Science. 313 (2006) 629-33.

[5] Resnick, A. Mechanical properties of a primary cilium as measured by resonant oscillation, Biophysical Journal. 109 (2015) 18-25.

[6] Nauli, SM, Alenghat, FJ, Luo, Y, Williams, E, Vassilev, P, Lil, XG, et al. Polycystins 1 and 2 mediate mechanosensation in the primary cilium of kidney cells, Nature Genetics. 33 (2003) 129-37.

[7] Praetorius, HA, Frokiaer, J, Nielsen, S, Spring, KR. Bending the primary cilium opens Ca2+-sensitive intermediate-conductance K+ channels in MDCK cells, Journal of Membrane Biology. 191 (2003) 193-200.

[8] Praetorius, HA, Spring, KR. Bending the mdck cell primary cilium increases intracellular calcium, The Journal of Membrane Biology. 184 (2001) 71-9.

[9] Praetorius, HA, Spring, KR. Removal of the MDCK Cell Primary Cilium Abolishes Flow Sensing, The Journal of Membrane Biology. 191 (2003) 69-76.

[10] Boo, YC, Jo, H. Flow-dependent regulation of endothelial nitric oxide synthase: role of protein kinases, American Journal of Physiology-Cell Physiology. 285 (2003) C499-C508.

[11] Yoder, BK. Role of primary cilia in the pathogenesis of polycystic kidney disease, Journal of the American Society of Nephrology. 18 (2007) 1381-8.

[12] Yoder, BK, Hou, XY, Guay-Woodford, LM. The polycystic kidney disease proteins, polycystin-1, polycystin-2, polaris, and cystin, are co-localized in renal cilia, Journal of

the American Society of Nephrology. 13 (2002) 2508-16.

[13] Masyuk, AI, Masyuk, TV, LaRusso, NF. Cholangiocyte primary cilia in liver health and disease, Developmental Dynamics. 237 (2008) 2007-12.

[14] McGlashan, SR, Cluett, EC, Jensen, CG, Poole, CA. Primary cilia in osteoarthritic chondrocytes: From chondrons to clusters, Developmental Dynamics. 237 (2008) 2013-20.

[15] Sen Gupta, P, Prodromou, NV, Chapple, JP. Can faulty antennae increase adiposity? The link between cilia proteins and obesity, Journal of Endocrinology. 203 (2009) 327-36.

[16] Hassounah, NB, Bunch, TA, McDermott, KM. Molecular pathways: The role of primary cilia in cancer progression and therapeutics with a focus on hedgehog signaling, Clinical Cancer Research. 18 (2012) 2429-35.

[17] Menzl, I, Lebeau, L, Pandey, R, Hassounah, NB, Li, FW, Nagle, R, et al. Loss of primary cilia occurs early in breast cancer development, Cilia. 3 (2014) 7.

[18] Khayyeri, H, Barreto, S, Lacroix, D. Primary cilia mechanics affects cell mechanosensation: A computational study, Journal of Theoretical Biology. 379 (2015) 38-46.

[19] Resnick, A. HIF stabilization weakens primary cilia, Plos One. 11 (2016) 15.

[20] Hanasoge, S, Hesketh, PJ, Alexeev, A. Metachronal motion of artificial magnetic cilia, Soft Matter. 14 (2018) 3689-93.

[21] Lim, YC, McGlashan, SR, Cooling, MT, Long, DS. Culture and detection of primary cilia in endothelial cell models, Cilia. 4 (2015) 11.

[22] Shimozawa, T, Kanou, M. The aerodynamics and sensory physiology of range fractionation in the cereal filiform sensilla of the cricketGryllus bimaculatus, Journal of Comparative Physiology A-neuroethology Sensory Neural and Behavioral Physiology. 155 (1984) 495-505.

[23] Shimozawa, T, Kanou, M. Varieties of filiform hairs: range fractionation by sensory afferents and cereal interneurons of a cricket, Journal of Comparative Physiology A. 155 (1984) 485-93.

[24] Barth, FG, Wastl, U, Humphrey, JAC, Devarakonda, R. Dynamics of arthropod

filiform hairs. II. Mechanical properties of spider trichobothria (cupiennius salei keys.), Philosophical Transactions of the Royal Society of London Series B: Biological Sciences. 340 (1993) 445-61.

[25] Humphrey, J, Devarakonda, R, Iglesias, I, Barth, F. Dynamics of Arthropod Filiform Hairs. I. Mathematical Modelling of the Hair and Air Motions, Philosophical Transactions of The Royal Society B: Biological Sciences. 340 (1993) 423-44.

[26] Cummins, B, Gedeon, T, Klapper, I, Cortez, R. Interaction between arthropod filiform hairs in a fluid enviroment, Journal of theoretical biology. 247 (2007) 266-80.

[27] Schwartz, EA, Leonard, ML, Bizios, R, Bowser, SS. Analysis and modeling of the primary cilium bending response to fluid shear, American Journal of Physiology-Renal Physiology. 272 (1997) F132-F8.

[28] Downs, ME, Nguyen, AM, Herzog, FA, Hoey, DA, Jacobs, CR. An experimental and computational analysis of primary cilia deflection under fluid flow, Computer Methods in Biomechanics and Biomedical Engineering. 17 (2014) 2-10.

[29] Herzog, F. A mechanical approach to study the bending of the primary cilium in response to fluid flow. in: D Pioletti, (Ed.).2010.

[30] Liu, W, Murcia, NS, Duan, Y, Weinbaum, S, Yoder, BK, Schwiebert, E, et al. Mechanoregulation of intracellular Ca2+ concentration is attenuated in collecting duct of monocilium-impaired orpk mice, American journal of physiology Renal physiology. 289 (2005) F978.

[31] Nguyen, AM, Young, YN, Jacobs, CR. The primary cilium is a self-adaptable, integrating nexus for mechanical stimuli and cellular signaling, Biology Open. 4 (2015) 1733-8.

[32] Li, L, Manikantan, H, Saintillan, D, Spagnolie, Saverio E. The sedimentation of flexible filaments, Journal of Fluid Mechanics. 735 (2013) 705-36.

[33] Tornberg, A-K, Gustavsson, K. A numerical method for simulations of rigid fiber suspensions, Journal of Computational Physics. 215 (2006) 172-96.

[34] Tornberg, A-K, Shelley, MJ. Simulating the dynamics and interactions of flexible fibers in Stokes flows, Journal of Computational Physics. 196 (2004) 8-40.

[35] Young, YN, Downs, M, Jacobs, CR. Dynamics of the Primary Cilium in Shear

Flow, Biophysical Journal. 103 (2012) 629-39.

[36] Battle, C, Ott, CM, Burnette, DT, Lippincott-Schwartz, J, Schmidt, CF. Intracellular and extracellular forces drive primary cilia movement, Proceedings of the National Academy of Sciences. 112 (2015) 1410-5.

[37] Rydholm, S, Zwartz, G, Kowalewski, JM, Kamali-Zare, P, Frisk, T, Brismar, H. Mechanical properties of primary cilia regulate the response to fluid flow, Am J Physiol-Renal Physiol. 298 (2010) F1096-F102.

[38] O"Connor, J, Revell, A, Mandal, P, Day, P. Application of a Lattice Boltzmann-Immersed Boundary Method for Fluid-Filament Dynamics and Flow Sensing, Journal of Biomechanics. 49 (2015) 2143-51.

[39] Connell, BSH, Yue, DKP. Flapping dynamics of a flag in a uniform stream, J Fluid Mech. 581 (2007) 33-68.

[40] Zhu, LD, Peskin, CS. Interaction of two flapping filaments in a flowing soap film, Physics of Fluids. 15 (2003) 1954-60.

[41] Peskin, CS. Numerical analysis of blood flow in the heart, Journal of Computational Physics. 25 (1977) 220-52.

[42] Peskin, CS. The Fluid Dynamics of Heart Valves: Experimental, Theoretical, and Computational Methods, Annual Review of Fluid Mechanics. 14 (1982) 235-59.

[43] Peskin , C. Peskin, C.S.: The immersed boundary method. Acta Numerica 11, 479-517, Acta Numerica. 11 (2002) 479-517.

[44] Goza, A, Colonius, T. A strongly-coupled immersed-boundary formulation for thin elastic structures, Journal of Computational Physics. 336 (2017) 401-11.

[45] Huang, W-X, Shin, SJ, Sung, HJ. Simulation of flexible filaments in a uniform flow by the immersed boundary method, Journal of Computational Physics. 226 (2007) 2206-28.

[46] Tian, F-B, Luo, H, Zhu, L, Liao, JC, Lu, X-Y. An efficient immersed boundary-lattice Boltzmann method for the hydrodynamic interaction of elastic filaments, Journal of Computational Physics. 230 (2011) 7266-83.

[47] Yuan, H-Z, Niu, X-D, Shu, S, Li, M, Yamaguchi, H. A momentum exchange-based immersed boundary-lattice Boltzmann method for simulating a flexible filament in an

incompressible flow, Computers & Mathematics with Applications. 67 (2014) 1039-56.

[48] Zhu, L, Peskin, CS. Simulation of a Flapping Flexible Filament in a Flowing Soap Film by the Immersed Boundary Method, Journal of Computational Physics. 179 (2002) 452-68.

[49] Heys, J, Gedeon, T, Knott, BC, Kim, Y. Modeling arthropod filiform hair motion using the penalty immersed boundary method, Journal of biomechanics. 41 (2008) 977-84.

[50] Zhu, P-F, Li, X, Li, A, Liu, Y, Chen, D-D, Xu, Y-q. Simulation Study on the Mass Transport Based on the Ciliated Dynamic System of the Respiratory Tract, Computational and Mathematical Methods in Medicine. 2019 (2019) 1-9.

[51] Cui, J, Liu, Y, Fu, B. Numerical study on the dynamics of primary cilium in pulsatile flows by the immersed boundary-lattice Boltzmann method, Biomechanics and Modeling in Mechanobiology. 19 (2019).

[52] O'Connor, J, Revell, A, Mandal, P, Day, P. Application of a Lattice Boltzmann-Immersed Boundary Method for Fluid-Filament Dynamics and Flow Sensing, Journal of Biomechanics. 49 (2016) 2143-51.

[53] Egorova, AD, van der Heiden, K, Poelmann, RE, Hierck, BP. Primary cilia as biomechanical sensors in regulating endothelial function, Differentiation. 83 (2012) S56-S61.

[54] Poudineh, M, Labib, M, Ahmed, S, Nguyen, M, Kermanshah, L, Mohamadi, R, et al. Profiling Functional and Biochemical Phenotypes of Circulating Tumor Cells Using a Two-Dimensional Sorting Device, Angewandte Chemie International Edition. (2016).

[55] Weiss, L. Invivo Selection of Human Renal-Carcinoma Cells with High Metastatic Potential in Nude-Mice - Comments, Clin Exp Metastas. 8 (1990) 103-6.

[56] Cai, B, Fan, J, Zeng, M, Zhang, L, Fu, BM. Adhesion of malignant mammary tumor cells MDA-MB-231 to microvessel wall increases microvascular permeability via degradation of endothelial surface glycocalyx, Journal of Applied Physiology. 113 (2012) 1141.

[57] Guo, P, Cai, B, Lei, M, Liu, Y, Fu, BM. Differential arrest and adhesion of tumor

cells and microbeads in the microvasculature, Biomechanics and Modeling in Mechanobiology. 13 (2014) 537-50.

[58] Haier, J, Nicolson, G. Haier J, Nicolson GL.. Tumor cell adhesion under hydrodynamic conditions of fluid flow. APMIS 109: 241-262, APMIS : acta pathologica, microbiologica, et immunologica Scandinavica. 109 (2001) 241-62.

[59] Janiszewska, M, Primi, M, Izard, T. Cell adhesion in cancer: Beyond the migration of single cells, Journal of Biological Chemistry. 295 (2020) jbc.REV119.007759.

[60] Zhu, C, Bao, G, Wang, N. Cell mechanics: Mechanical response, cell adhesion, and molecular deformation, Annu Rev Biomed Eng. 2 (2000) 189-226.

[61] Weiss, L. Biomechanical Interactions of Cancer-Cells with the Microvasculature during Hematogenous Metastasis, Cancer and Metastasis Reviews. 11 (1992) 227-35.

[62] Wirtz, D, Konstantopoulos, K, Searson, PC. The physics of cancer: the role of physical interactions and mechanical forces in metastasis, Nature reviews Cancer. 11 (2011) 512-22.

[63] Hoshino, A, Costa-Silva, B, Shen, T-L, Rodrigues, G, Hashimoto, A, Mark, M, et al. Tumour exosome integrins determine organotropic metastasis, Nature. 527 (2015).

[64] Dong, C, Slattery, M, Liang, S. Micromechanics of tumor cell adhesion and migration under dynamic flow conditions, Frontiers in bioscience : a journal and virtual library. 10 (2005) 379-84.

[65] Marshall, B, Sarangapani, K, Lou, J, McEver, R, Zhu, C. Force History Dependence of Receptor-Ligand Dissociation, Biophysical journal. 88 (2005) 1458-66.

[66] Mao, S, Zhang, Q, Li, H, Zhang, W, Huang, Q, Khan, M, et al. Adhesion analysis of single circulating tumor cells on a base layer of endothelial cells using open microfluidics, Chem Sci. 9 (2018) 7694-9.

[67] Rejniak, KA. Investigating dynamical deformations of tumor cells in circulation: predictions from a theoretical model, Frontiers in oncology. 2 (2012) 111.

[68] Xiao, L, Liu, Y, Chen, S, Fu, B. Effects of flowing RBCs on adhesion of a circulating tumor cell in microvessels, Biomechanics and Modeling in Mechanobiology. 16 (2016).

[69] Liu, Q, Mirc, D, Fu, BM. Mechanical mechanisms of thrombosis in intact bent

microvessels of rat mesentery, Journal of Biomechanics. 41 (2008) 2726-34.

[70] Zhang, L, Zeng, M, Fu, B. Inhibition of endothelial nitric oxide synthase decreases breast cancer cell MDA-MB-231 adhesion to intact microvessels under physiological flows, American journal of physiology Heart and circulatory physiology. 310 (2016) ajpheart.00109.2016.

[71] Zhang, L, Zeng, M, Fu, BM. Inhibition of endothelial nitric oxide synthase decreases breast cancer cell MDA-MB-231 adhesion to intact microvessels under physiological flows, Am J Physiol Heart Circ Physiol. 310 (2016) H1735-47.

[72] Yan, W, Cai, B, Liu, Y, Fu, B. Effects of wall shear stress and its gradient on tumor cell adhesion in curved microvessels, Biomechanics and modeling in mechanobiology. 11 (2011) 641-53.

[73] Yan, W, Liu, Y, Fu, B. Effects of curvature and cell-cell interaction on cell adhesion in microvessels, Biomechanics and modeling in mechanobiology. 9 (2010) 629-40.

[74] Sbragaglia, M, Chen, H, Shan, X, Succi, S. Continuum Free-Energy formulation for a class of Lattice Boltzmann multiphase models, EPL (Europhysics Letters). 86 (2009).

[75] Shan, X, Chen, H. Lattice Boltzmann Model for Simulating Flows with Multiple Phases and Components, Physical review E, Statistical physics, plasmas, fluids, and related interdisciplinary topics. 47 (1993) 1815-9.

[76] Chen, H, Kandasamy, S, Orszag, S, Shock, R, Succi, S, Yakhot, V. Extended Boltzmann Kinetic Equation for Turbulent Flows, Science (New York, NY). 301 (2003) 633-6.

[77] Dong, Y-H, Sagaut, P. A study of time correlations in lattice Boltzmann-based large-eddy simulation of isotropic turbulence, Physics of Fluids. 20 (2008).

[78] Ladd, A. Numerical Simulations of Particulate Suspensions via a Discretized Boltzmann Equation Part II. Numerical Results, Journal of Fluid Mechanics. 271 (1993).

[79] Ladd, AJC. Numerical simulations of particulate suspensions via a discretized Boltzmann equation. Part 1. Theoretical foundation, Journal of Fluid Mechanics. 271 (1994) 285-309.

[80] Boyd, J, Buick, J, Cosgrove, J, Stansell, P. Application of the lattice Boltzmann model to simulated stenosis growth in a two-dimensional carotid artery, Physics in medicine and biology. 50 (2005) 4783-96.

[81] Boyd, J, Buick, J, Green, S. Analysis of the Casson and Carreau-Yasuda non-Newtonian blood models in steady and oscillatory flow using the lattice Boltzmann method, Physics of Fluids. 19 (2007).

[82] Kang, Q, Zhang, D, Chen, S, He, X. Lattice Boltzmann simulation of chemical dissolution in porous media, Physical review E, Statistical, nonlinear, and soft matter physics. 65 (2002) 036318.

[83] Aidun, C, Clausen, J. Lattice-Boltzmann Method for Complex Flows, Annual Review of Fluid Mechanics. 42 (2009) 439-72.

[84] Bernaschi, M, Melchionna, S, Succi, S. Mesoscopic simulations at the physics-chemistry-biology interface2019.

[85] Hardy, J, Pomeau, Y, Pazzis, O. Time Evolution of a Two-Dimensional Classical Lattice System, Physical Review Letters. 31 (1973) 276-9.

[86] Frisch, U, Hasslacher, B, Pomeau, Y. Lattice-Gas Automata for the Navier-Stokes Equation, Physical review letters. 56 (1986) 1505-8.

[87] McNamara, GR, Zanetti, G. Use of the Boltzmann Equation to Simulate Lattice-Gas Automata, Physical review letters. 61 (1988) 2332-5.

[88] Chen, H, Chen, S, Matthaeus, W. Recovery of the Navier-Stokes Equations Using a Lattice-Gas Boltzmann Method, Physical Review A. 45 (1992).

[89] Qian, YH, Dhumieres, D, Lallemand, P. Lattice BGK model for Navier-Stokes equation, Physical Review E. 61 (1992) 401-14.

[90] Guo, Z, Zheng, C, Shi, B. Discrete lattice effects on the forcing term in the lattice Boltzmann method, Physical review E, Statistical, nonlinear, and soft matter physics. 65 (2002) 046308.

[91] Ginzburg, I, Dhumieres, D, Kuzmin, A. Optimal Stability of Advection-Diffusion Lattice Boltzmann Models with Two Relaxation Times for Positive/Negative Equilibrium, Journal of Statistical Physics. 139 (2010) 1090-143.

[92] Kuzmin, A, Ginzburg, I, Mohamad, AA. The role of the kinetic parameter in the

stability of two-relaxation-time advection–diffusion lattice Boltzmann schemes, Computers & Mathematics with Applications. 61 (2011) 3417-42.

[93] Krüger, T, Kusumaatmaja, H, Kuzmin, A, Shardt, O, Silva, G, Viggen, EM. The Lattice Boltzmann Method - Principles and Practice2016.

[94] Luo, L-S, Liao, W, Chen, X, Peng, Y, Zhang, W. Numerics of the lattice Boltzmann method: effects of collision models on the lattice Boltzmann simulations, Physical review E, Statistical, nonlinear, and soft matter physics. 83 (2011) 056710-.

[95] Premnath, K, Abraham, J. Three-Dimensional Multi-Relaxation Time (MRT) Lattice-Boltzmann Models for Multiphase Flow, Journal of Computational Physics. 224 (2007) 539-59.

[96] D'Humières, D, Ginzburg, I, Krafczyk, M, Lallemand, P, Luo, LS. Multiple-Relaxation-Time Lattice Boltzmann Models in Three Dimensions, Philosophical Transactions of The Royal Society A Mathematical Physical and Engineering ences. 360 (2002) 437-51.

[97] Lallemand, P, Luo, L-S. Theory of the Lattice Boltzmann Method: Dispersion, Dissipation, Isotropy, Galilean Invariance, and Stability, Physical review E, Statistical physics, plasmas, fluids, and related interdisciplinary topics. 61 (2000) 6546-62.

[98] McCracken, M, Abraham, J. Multiple-relaxation-time lattice-Boltzmann model for multiphase flow, Physical review E, Statistical, nonlinear, and soft matter physics. 71 (2005) 036701.

[99] Premnath, K, Abraham, J. Lattice Boltzmann Model for Axisymmetric Multiphase Flows, Physical review E, Statistical, nonlinear, and soft matter physics. 71 (2005) 056706.

[100] Premnath, K, Pattison, M, Banerjee, S. Generalized Lattice-Boltzmann Equation with Forcing Term for Computation of Wall-Bounded Turbulent Flows, Physical review E, Statistical, nonlinear, and soft matter physics. 79 (2009) 026703.

[101] Premnath, KN, Abraham, J. Lattice boltzmann simulations of drop–drop interactions in two-phase flows, International Journal of Modern Physics C. 16 (2005) 25-44.

[102] Xiaoyi, He, Xiaowen, Shan, Gary, D., et al. Discrete Boltzmann equation model

for nonideal gases, Physical Review E. 57 (1998) R13–R6.

[103] Cornubert, R, Dhumieres, D, Levermore, D. A Knudsen layer theory for lattice gases, Physica D: Nonlinear Phenomena. 47 (1991).

[104] Ginzburg, I, Adler, P. Boundary flow condition analysis for the three-dimensional lattice Bolzmann model, Journal de Physique II. 4 (1994) 191.

[105] Verschaeve, JCG. Analysis of the lattice Boltzmann Bhatnagar-Gross-Krook no-slip boundary condition: Ways to improve accuracy and stability, Physical Review E. 80 (2009) 036703.

[106] Ziegler, D. Boundary conditions for Lattice Boltzmann simulations, Journal of Statistical Physics. 71 (1993) 1171-7.

[107] Filippova, O, Hänel, D. Grid Refinement for Lattice-BGK Models, Journal of Computational Physics. 147 (1998) 219-28.

[108] Ginzburg, I, d'Humières, D. Multireflection boundary conditions for lattice Boltzmann models, Physical Review E. 68 (2003) 066614.

[109] Guo, Z, Chu-Guang, Z, Shi, B. Non-equilibrium extrapolation method for velocity and boundary conditions in the lattice Boltzmann method, Chinese Physics. 11 (2002) 366.

[110] Guo, Z, Zheng, C, Shi, B. An extrapolation method for boundary conditions in lattice Boltzmann method, Physics of Fluids. 14 (2002).

[111] Mei, R, Luo, L-S, Shyy, W. An Accurate Curved Boundary Treatment in the Lattice Boltzmann Method, Journal of Computational Physics. 155 (1999) 307-30.

[112] Zou, Q, He, X. On pressure and velocity boundary conditions for the Lattice Boltzmann BGK model, Physics of Fluids. 9 (1996).

[113] Hecht, M, Harting, J. Implementation of on-site velocity boundary conditions for D3Q19 lattice Boltzmann simulations (vol 2010, P01018, 2010), Journal of Statistical Mechanics Theory and Experiment. 2013 (2008).

[114] Orlanski, I. A simple boundary condition for unbounded hyperbolic flows, Journal of Computational Physics. 21 (1976) 251-69.

[115] Kang, X. Assessment of the pulsatile wall shear stress in the stenosed and recanalized carotid bifurcations by the lattice Boltzmann method, Computers & Fluids.

97 (2014) 156–63.

[116] Mei, R, Yu, D, Shyy, W, Luo, L-S. Force Evaluation in the Lattice Boltzmann Method Involving Curved Geometry, Physical review E, Statistical, nonlinear, and soft matter physics. 65 (2002) 041203.

[117] Stahl, B, Chopard, B, Latt, J. Measurements of wall shear stress with the lattice Boltzmann method and staircase approximation of boundaries, Computers & Fluids. 39 (2010) 1625-33.

[118] Kang, X, Dun, Z. Accuracy and grid convergence of wall shear stress measured by lattice Boltzmann method, International Journal of Modern Physics C. 25 (2014) 1450057.

[119] Eggleton, CD, Popel, AS. Large deformation of red blood cell ghosts in a simple shear flow, Physics of Fluids. 10 (1998) 1834-45.

[120] Fauci, LJ, McDonald, A. Sperm motility in the presence of boundaries, Bulletin of Mathematical Biology. 57 (1995) 679-99.

[121] Fauci, LJ, Peskin, CS. A computational model of aquatic animal locomotion, Journal of Computational Physics. 77 (1988) 85-108.

[122] Miller, L, Peskin, C. When vortices stick: An aerodynamic transition in tiny insect flight, The Journal of experimental biology. 207 (2004) 3073-88.

[123] Stockie, JM, Wetton, BR. Analysis of Stiffness in the Immersed Boundary Method and Implications for Time-Stepping Schemes, Journal of Computational Physics. 154 (1999) 41-64.

[124] Stockie, JM, Wetton, BTR. Stability Analysis for the Immersed Fiber Problem, SIAM Journal on Applied Mathematics. 55 (1995) 1577-91.

[125] Mayo, A, Peskin, C. An implicit numerical method for fluid dynamics problems with immersed elastic boundaries, Contemp Math. 141 (1993).

[126] Mori, Y, Peskin, CS. Implicit second-order immersed boundary methods with boundary mass, Computer Methods in Applied Mechanics and Engineering. 197 (2008) 2049-67.

[127] Ceniceros, H, Fisher, J, Roma, A. Efficient solutions to robust, semi-implicit discretizations of the immersed boundary method, Journal of Computational Physics.

228 (2009) 7137-58.

[128] Ceniceros, HD, Fisher, JE, Roma, AM. Efficient solutions to robust, semi-implicit discretizations of the immersed boundary method, Journal of Computational Physics. 228 (2009) 7137-58.

[129] Hou, T, Shi, Z. An efficient semi-implicit immersed boundary method for the Navier–Stokes equations, Journal of Computational Physics. 227 (2008) 8968-91.

[130] Sotiropoulos, F, Yang, X. Immersed boundary methods for simulating fluid–structure interaction, Progress in Aerospace Sciences. 65 (2013).

[131] Wu, J, Shu, C. Implicit velocity correction-based immersed boundary-lattice Boltzmann method and its applications, Journal of Computational Physics. 228 (2009) 1963-79.

[132] Kang, S, Hassan, Y. An immersed boundary-lattice Boltzmann method for large particle sedimentation2008.

[133] Le, DV, Khoo, BC, Lim, KM. An implicit-forcing immersed boundary method for simulating viscous flows in irregular domains, Computer Methods in Applied Mechanics and Engineering. 197 (2008) 2119-30.

[134] Wang, Z, Fan, J, Luo, K. Combined multi-direct forcing and immersed boundary method for simulating flows with moving particles, International Journal of Multiphase Flow. 34 (2008) 283-302.

[135] Tao, S, He, Q, Chen, J, Chen, B, Yang, G, Wu, Z. A non-iterative immersed boundary-lattice Boltzmann method with boundary condition enforced for fluid-solid flows, Applied Mathematical Modelling. 76 (2019).

[136] Niu, XD, Shu, C, Chew, YT, Peng, Y. A momentum exchange-based immersed boundary-lattice Boltzmann method for simulating incompressible viscous flows, Physics Letters A. 354 (2006) 173-82.

[137] Yuan, HZ, Niu, XD, Shu, S, Li, MJ, Yamaguchi, H. A momentum exchange-based immersed boundary-lattice Boltzmann method for simulating a flexible filament in an incompressible flow, Computers & Mathematics with Applications. 67 (2014) 1039-56.

[138] Hu, Y, Yuan, H-Z, Shu, S, Li, M. An improved momentum exchanged-based immersed boundary–lattice Boltzmann method by using an iterative technique,

Computers & Mathematics with Applications. 68 (2014).

[139] Goldstein, D, Handler, R, Sirovich, L. Modeling a No-Slip Flow Boundary with an External Force Field, Journal of Computational Physics. 105 (1993) 354-66.

[140] Mittal, R, Dong, H, Bozkurttas, M, Najjar, F, Vargas, A, Loebbecke, A. A versatile sharp interface immersed boundary method for incompressible flows with complex boundaries, Journal of computational physics. 227 (2008) 4825-52.

[141] Seo, JH, Mittal, R. A sharp-interface immersed boundary method with improved mass conservation and reduced spurious pressure oscillations, Journal of Computational Physics. 230 (2011) 7347-63.

[142] Kim, J, Kim, D, Choi, H. An Immersed-Boundary Finite-Volume Method for Simulations of Flow in Complex Geometries, Journal of Computational Physics. 171 (2001) 132-50.

[143] Lee, J, Kim, J, Choi, H, Yang, K-S. Sources of spurious force oscillations from an immersed boundary method for moving-body problems, J Comput Physics. 230 (2011) 2677-95.

[144] Yang, X, Zhang, X, Li, Z, He, G-W. A smoothing technique for discrete delta functions with application to immersed boundary method in moving boundary simulations, Journal of Computational Physics. 228 (2009) 7821-36.

[145] Wiens, J, Stockie, J. Simulating flexible fiber suspensions using a scalable immersed boundary algorithm, Computer Methods in Applied Mechanics and Engineering. 290 (2015) 1-18.

[146] Fan, X, Phan-Thien, N, Chen, S, Wu, X, Yong Ng, T. Simulating flow of DNA suspension using dissipative particle dynamics, Physics of Fluids. 18 (2006) 063102.

[147] Soares, J, Gao, C, Alemu, Y, Slepian, M, Bluestein, D. Simulation of Platelets Suspension Flowing Through a Stenosis Model Using a Dissipative Particle Dynamics Approach, Annals of biomedical engineering. 41 (2013).

[148] Hoogerbrugge, PJ, Koelman, JMVA. Simulating Microscopic Hydrodynamic Phenomena with Dissipative Particle Dynamics, Europhysics Letters (EPL). 19 (1992) 155-60.

[149] Espanol, Pep. Hydrodynamics from dissipative particle dynamics, Phys Rev E

Stat Phys Plasmas Fluids Relat Interdiscip Topics. 52 (1995) 1734-42.

[150] Groot, RD, Warren, PB. Dissipative particle dynamics: Bridging the gap between atomistic and mesoscopic simulation, The Journal of Chemical Physics. 107 (1997) 4423-35.

[151] Fedosov, DA, Caswell, B, Karniadakis, GE. Systematic coarse-graining of spectrin-level red blood cell models, Computer Methods in Applied Mechanics and Engineering. 199 (2010) 1937-48.

[152] Hammer, DA, Apte, SM. Simulation of cell rolling and adhesion on surfaces in shear flow: general results and analysis of selectin-mediated neutrophil adhesion, Biophysical Journal. 63 (1992) 35-57.

[153] Krüger, T, Holmes, D, Coveney, P. Deformability-based red blood cell separation in deterministic lateral displacement devices-A simulation study, Biomicrofluidics. 8 (2014).

[154] Mei , R. Flow due to an oscillating sphere and an expression for unsteady drag on the sphere at finite Reynolds number, Journal of Fluid Mechanics. 270 (1994) 133-74.

[155] Tian, F-B, Dai, H, Luo, H, Doyle, JF, Rousseau, B. Fluid–structure interaction involving large deformations: 3D simulations and applications to biological systems, Journal of Computational Physics. 258 (2014) 451-69.

[156] Saff, E, Kuijlaars, A. Distributing Many Points on a Sphere, Math Intell. 19 (1997) 5-11.

[157] Suzuki, K, Inamuro, T. Effect of internal mass in the simulation of a moving body by the immersed boundary method, Computers & Fluids. 49 (2011) 173–87.

[158] Doddi, SK, Bagchi, P. Three-dimensional computational modeling of multiple deformable cells flowing in microvessels, Physical Review E. 79 (2009) 046318.

[159] Resnick, A, Hopfer, U. Force-response considerations in ciliary mechanosensation, Biophysical Journal. 93 (2007) 1380-90.

[160] O'Connor, AK, Malarkey, EB, Berbari, NF, Croyle, MJ, Haycraft, CJ, Bell, PD, et al. An inducible Cilia$^{GFP}$ mouse model for in vivo visualization and analysis of cilia in live tissue, Cilia. 2 (2013) 8.

[161] Kevlahan, NK-R, Hunt, JCR, Vassilicos, JC. A comparison of different analytical techniques for identifying structures in turbulence, Applied Scientific Research. 53 (1994) 339-55.

[162] Davies, PF. Hemodynamic shear stress and the endothelium in cardiovascular pathophysiology, Nature clinical practice Cardiovascular medicine. 6 (2009) 16-26.

[163] Moore, JE, Xu, C, Glagov, S, Zarins, CK, Ku, DN. Fluid wall shear stress measurements in a model of the human abdominal aorta: oscillatory behavior and relationship to atherosclerosis, Atherosclerosis. 110 (1994) 225-40.

[164] Heys, JJ, Gedeon, T, Knott, BC, Kim, Y. Modeling arthropod filiform hair motion using the penalty immersed boundary method, Journal of Biomechanics. 41 (2008) 977-84.

[165] Besschetnova, TY, Kolpakova-Hart, E, Guan, YH, Zhou, J, Olsen, BR, Shah, JV. Identification of Signaling Pathways Regulating Primary Cilium Length and Flow-Mediated Adaptation, Current Biology. 20 (2010) 182-7.

[166] Gardner, K, Arnoczky, SP, Lavagnino, M. Effect of in vitro stress-deprivation and cyclic loading on the length of tendon cell cilia in situ, Journal of orthopaedic research : official publication of the Orthopaedic Research Society. 29 (2011) 582-7.

[167] Baskurt, O, Meiselman, H. Blood Rheology and Hemodynamics, Seminars in thrombosis and hemostasis. 29 (2003) 435-50.

[168] Farnoush, S, Manzari, M. An investigation on the body force modeling in a lattice Boltzmann BGK simulation of generalized Newtonian fluids, Physica A: Statistical Mechanics and its Applications. 415 (2014) 315–32.

[169] Gabbanelli, S, Drazer, G, Koplik, J. Lattice Boltzmann Method for non-Newtonian (Power-Law) Fluids, Physical review E, Statistical, nonlinear, and soft matter physics. 72 (2005) 046312.

[170] Xiao, L, Chen, S, Lin, C, Liu, Y. Simulation of a Single Red Blood Cell Flowing Through a Microvessel Stenosis Using Dissipative Particle Dynamics, Molecular & cellular biomechanics : MCB. 11 (2014) 67-85.

[171] Xiao, L, Liu, Y, Chen, S, Fu, B. Numerical simulation of a single cell passing through a narrow slit, Biomechanics and Modeling in Mechanobiology. 15 (2016).

[172] Xiao, L, Liu, Y, Chen, S, Fu, B. Simulation of Deformation and Aggregation of Two Red Blood Cells in a Stenosed Microvessel by Dissipative Particle Dynamics, Cell Biochemistry and Biophysics. 74 (2016).

[173] Skalak, R, Chien, S. Handbook of bioengineering. New York, McGraw-Hill; 1987.

[174] Schwarz, U, Alon, R. From The Cover: L-selectin-mediated leukocyte tethering in shear flow is controlled by multiple contacts and cytoskeletal anchorage facilitating fast rebinding events, Proceedings of the National Academy of Sciences of the United States of America. 101 (2004) 6940-5.

[175] Alon, R. The Kinetics of L-selectin Tethers and the Mechanics of Selectin-mediated Rolling, Journal of Cell Biology. 138 (1997) 1169-80.

[176] Dembo, M, Torney, D, Saxman, K, Da, H. The Reaction-Limited Kinetics of Membrane-to-Surface Adhesion and Detachment, Proceedings of the Royal Society of London Series B, Containing papers of a Biological character Royal Society (Great Britain). 234 (1988) 55-83.

[177] Chang, K-C, Hammer, D. Influence of Direction and Type of Applied Force on the Detachment of Macromolecularly-Bound Particles from Surfaces, Langmuir. 12 (1996).

[178] Yao, Y, Rabodzey, A, Dewey, C. Glycocalyx modulates the motility and proliferative response of vascular endothelium to fluid shear stress, American journal of physiology Heart and circulatory physiology. 293 (2007) H1023-30.

[179] Swift, M, Osborn, W, Yeomans, J. Lattice Boltzmann Simulation of Non-Ideal Fluids, Physical Review Letters. 75 (1995).

[180] Bendas, G, Borsig, L. Cancer cell adhesion and metastasis: selectins, integrins, and the inhibitory potential of heparins, International journal of cell biology. 2012 (2012) 676731.

[181] Van der Heiden, K, Hierck, BP, Krams, R, de Crom, R, Cheng, C, Baiker, M, et al. Endothelial primary cilia in areas of disturbed flow are at the base of atherosclerosis, Atherosclerosis. 196 (2008) 542-50.

[182] King, M, Phillips, K, Mitrugno, A, Lee, T-R, Am, d, Chandrasekaran, S, et al. A physical sciences network characterization of circulating tumor cell aggregate transport,

AJP Cell Physiology. 308 (2015).

[183] Phillips, KG, Lee, AM, Tormoen, GW, Rigg, RA, Kolatkar, A, Luttgen, M, et al. The thrombotic potential of circulating tumor microemboli: computational modeling of circulating tumor cell-induced coagulation, American Journal of Physiology-Cell Physiology. 308 (2015) C229-C36.

[184] Mook, ORF, Marle, JV, Vreeling-Sindelárová, H, Jonges, R, Frederiks, WM, Noorden, CJFV. Visualization of early events in tumor formation of eGFP-transfected rat colon cancer cells in liver, Hepatology. 38 (2003) 295-304.

[185] Huang, Q, Hu, X, He, W, Zhao, Y, Shi, M. Fluid shear stress and tumor metastasis, American Journal of Cancer Research. 8 (2018) 763.

[186] Wirtz, D, Konstantopoulos, K, Searson, P. The Physics of Cancer: The Role of Physical Interactions and Mechanical Forces in Metastasis, Nature reviews Cancer. 11 (2011) 512-22.